OPERATIONS, ACCELERATOR PHYSICS,

AND INSTRUMENTATION

K1200 OPERATING EXPERIENCE

D.R. Poe, H.A. Thulin and P. Miller

Table I shows operating time statistics for the K1200 cyclotron in 1992, and Table II shows the various beams which it ran. There were 81 beams with 135 different beam changes in 6625.5 hours of operation and 4993.5 hours of research. This means that there was a beam change every 49 hours of operation and every 37 hours of research time.

There were 4993.5 hours of research time in 1992 against 3553.5 hours in 1991. The "operation" category (research + development + overhead), which represents the time that the cyclotron was running, went from 5587.25 to 6625.50 hours in 1992. The efficiency, which is the time the cyclotron ran divided by the time that we tried to run it, increased from 81.2 % to 88.8 %. The total number of hours in 1992 was 8784, it being a leap year. Research was therefore carried on 56.8 % of the time, and operation was 75.5 %

As was mentioned last year, we are now running with silicone rubber O-rings in five of the six dee stem cavities, sealing the dee stem insulators. We have so far repaired three dee stems due to leaks at these joints in the two years since they were installed, but there have been no cases of the O-rings failing, only of the insulators failing. The sixth stem uses Delta seals, which use aluminum as a sealing surface. This has not failed, but a recent attempt to replace a pair of O-rings with delta seals on another stem was a failure due to an inability to make it leak tight. This problem is now being investigated, as we would like to use metal instead of the rubber seals, since the silicon rubber outgasses and is permeable to helium.

The RF group completed the project of building the Power Converter Cabinet, which houses the step-start circuitry, rectifier stacks, and filter choke in a cabinet inside the building. In terms of maintenance, this is an improvement over the original factory assembly, which had these elements submerged in oil in a tank outdoors. The RF group is now trying to replace the hydraulic servos of the input couplers and dee fine tuners with bang-bang servos, in hopes of improving reliabilty and maintenance problems.

There is a project moving forward at this time to replace the electromechanical switches in the trim coil power supplies for the bumps with all electronic switches of NSCL design. These switches are prone to failure due to their frequent usage, so the all electronic variety should improve reliability as well as making cyclotron tuning easier.

The deflectors are now able to run up to 100 kV/cm operationally. Both E1 and E2 are now running with anodized aluminum shoes, and spares of this type are being made. The anodized layer is believed to help control electron emission from the negative surface. E1 has a water cooled housing on the segment into which the beam enters (it is made in three segments so that the curvature can be changed to approximately match the shape of the beam). Instrumentation has been added to measure the temperature of the housing near the beam entrance, and a small beam probe is attached to the entrance of E1 at the radius of the last turn, as an aid to tuning. We have changed to a new model of insulator, which is made of Macor with titanium end caps, has a larger diameter than the old version (for strength), and has flutes cut into the side to inhibit electron travel along the length of the insulator. Tests at Chalk River showed this design to be superior to the older version, and operational experience seems to confirm this.

TABLE I: K1200 Time Distribution 1992

Operation	Hours	Percentage
Research	4993.50	64.06
Development	572.75	7.35
Overhead	1059.25	13.59
(R + D + O)	6625.50	85.00
Maintenance	337.50	4.33
Breakdown	831.50	10.67
TOTAL	7794.50	100.00%
OFF	975.00	

EFFICIENCY = E = (R + D + O) / (TOTAL - MAINTENANCE)
E = 6625.50 / (7794.5 - 337.5) = 0.888 = 88.8 %

K1200 BEAMS Jan. - Dec. 1992

Ion	E/A (MeV/u)	Hours	% Time
1 H2 1+	140.0	18.5	0.4
4 He 2+	170.0	9.0	0.2
4 He 2+	145.0	75.3	1.5
4 He 1+	60.0	6.5	0.1
4 He 1+	50.0	13.3	0.3
4 He 1+	40.0	196.0	3.9
5 (H-He) 1+	40.0	3.8	0.1
5 (H-He) 1+	34.9	128.0	2.5
5 (H-He) 1+	33.9	16.0	0.3
6 (D-He) 1+	22.0	31.8	0.6
7 Li 2+	50.0	434.3	8.6
7 Li 1+	19.0	92.8	1.8
11 B 2+	32.0	150.8	3.0
11 B 2+	25.0	4.0	0.1
12 C 5+	95.0	17.0	0.3
12 C 4+	70.0	9.0	0.2
12 C 3+	40.0	151.5	3.0
12 C 2+	22.0	34.0	0.7
14 N 6+	100.0	34.3	0.7
14 N 4+	70.0	98.5	2.0
14 N 3+	35.0	48.0	1.0
14 N 2+	19.0	11.8	0.2
15 N 6+	89.0	2.0	0.0
15 N 6+	88.0	1.0	0.0
15 N 6+	87.0	1.0	0.0
15 N 6+	86.0	1.3	0.0
15 N 6+	85.0	1.0	0.0
15 N 6+	84.0	1.0	0.0
15 N 6+	83.0	1.0	0.0
15 N 3+	30.0	1.0	0.0
16 O 5+	70.0	83.3	1.7
16 O 5+	60.0	59.0	1.2
16 O 4+	50.0	31.8	0.6
16 O 4+	40.0	25.5	0.5
16 O 3+	25.0	63.5	1.3
17 O 3+	25.0	145.3	2.9
18 O 6+	100.0	50.0	1.0
18 O 7+	100.0	96.8	1.9
18 O 6+	80.0	689.3	13.7
18 O 4+	35.0	14.3	0.3
20 Ne 10+	170.0	12.3	0.2
20 Ne 10+	140.0	23.0	0.5
20 Ne 8+	110.0	63.5	1.3
20 Ne 7+	80.0	123.3	2.4
20 Ne 6+	60.0	33.3	0.7
20 Ne 4+	30.0	51.0	1.0
22 Ne 4+	25.0	4.0	0.1
24 Mg 7+	60.0	74.0	1.5
28 Si 9+	80.0	227.8	4.5
36 Ar 16+	120.0	216.0	4.3
36 Ar 12+	80.0	101.0	2.0
38 Ar 15+	100.0	62.0	1.2
40 Ar 16+	115.0	14.5	0.3
40 Ar 13+	80.0	136.5	2.7
40 Ar 12+	80.0	102.8	2.0
40 Ar 11+	55.0	46.5	0.9
40 Ca 11+	55.0	72.3	1.4
40 Ar 10+	40.0	136.3	2.7
40 Ar 7+	25.0	44.3	0.9
52 Cr 14+	65.0	2.5	0.0
58 Ni 15+	70.0	11.5	0.2
58 Ni 16+	70.0	12.5	0.2
58 Ni 15+	70.0	68.0	1.3
58 Ni 15+	65.0	11.5	0.2
58 Ni 15+	60.0	17.0	0.3
84 Kr 23+	70.0	60.3	1.2
84 Kr 20+	55.0	38.0	0.8
84 Kr 17+	35.0	42.8	0.8
84 Kr 15+	30.0	134.0	2.7
86 Kr 24+	80.0	7.5	0.1
86 Kr 22+	70.0	77.3	1.5
129 Xe 30+	60.0	107.0	2.1
129 Xe 28+	50.0	30.3	0.6
129 Xe 26+	40.0	155.5	3.1
129 Xe 23+	30.0	49.0	1.0
129 Xe 19+	20.0	5.3	0.1
136 Xe 24+	30.0	91.5	1.8
197 Au 35+	30.0	2.3	0.0
197 Au 29+	20.0	120.5	2.4
238 U 35+	20.0	54.0	1.1
	5043.0	100.0	

K1200 INJECTION LINE SECTOR FARADAY CUPS

K. Harrison and T. A. Antaya

Introduction

In order to maximize the transmission of the low energy ($E \leq 15$ keV Q) positive ion beam from the ion sources to the cyclotron, it is important to be able to image the ion beam. With a good imaging system of the ion beam one can know:

1.) if the beam is well centered in the beam pipe

2.) the symmetry, or asymmetry of the beam

3.) if the steering and focusing magnets are having an effect on beam shape and intensity

Some imaging systems that have been attempted on the NSCL Injection Lines and the problems associated with them :

1.) Single plate faraday cups - no structure information

2.) Wire Scanners - doesn't show incoherent effects

3.) Phosphors - low sensitivity and/or low survival time

4.) Temperature Sensitive Liquid crystals - slow response and coarse

5.) Kapton Film - no real time display

We have replaced the existing single plate faraday cup with a sixteen sectored faraday cup that has greatly increased our beam tuning capabilities.

The 16 Channel Sectored Faraday Cup

The faraday cup is a two layer pc board with the sector pattern etched onto it via standard pc board fabrication techniques. The surface material is copper and the substrate is G-10. The board is shown in Figure 1. The beamside pattern consists of four concentric circles divided into quadrants, for a total of sixteen sectors. The sectors have a radial width of 5/16" and are separated by a 1/16" gap. A current path from the front to the back of the faraday cup is made through a solder filled hole in the center of each sector. Wires, to carry the current signal out of the vacuum system via a electrical vacuum feedthrough, are connected to either the solder filled hole or an etched edge connector circuit pattern on the back of the board.

Signal Processing

Each sector's ion beam signal goes through a vacuum feedthrough, across a 1M ohm resistor, to ground. The voltage across each of resistor is read by a 16 channel analog input multiplexer board. The boards for all of the faraday cups are daisy chained together and located in the K1200 injection line tunnel near the faraday cups to minimize signal cable lengths. The output of the multiplexer boards is sent to a 16 channel high speed Analog/Digital converter located in a 386/16SX PC, located next to the multiplexer boards in the tunnel. Using a compiled QuickBasic code, the currents, their totals, and ratios are computed and displayed on a Color Graphics monitor

located in the ECR control room. The intensity of the beam is shown graphically by assigning different colors shades to current ranges - bright green being the most intense, down to blue for negative currents. Using Windows, we are able to take snapshots of the display for later analysis. In order to keep computation time down, integer arithmetic is used in the code. The output is a full screen update with a refresh rate of ~ 10 Hz. The display is directly connected to the pc, which is ~ 100 feet away, without serial or network connections. Figure 2 shows a schematic of the signal processing system.

Cost of the system

Faraday cup boards	$200
386/16 SX PC	1000
Remote PC Display	400
Multiplexer board	400 (x4)
A/D Converter	400
Total	$3600

Conclusion

Using the sectored faraday cup system we have observed :

1.) The update speed is comparable to the Fermi Consoles display of single parameters.

2.) Total signal vs ratio tuning works well.

3.) Up/down and left/right asymmetries are observed.

4.) An improved transmission efficiency using the sectored faraday cups versus the old faraday cups.

When placed in the beam line, the sectored faraday cup board does exhibit some initial outgassing (mostly water), but with no long term effect on the base pressure of the system. The sectored faraday cup has been exposed to beam intensities of 300 euA of He^+ with an energy of 10 keV with no observable damage to it.

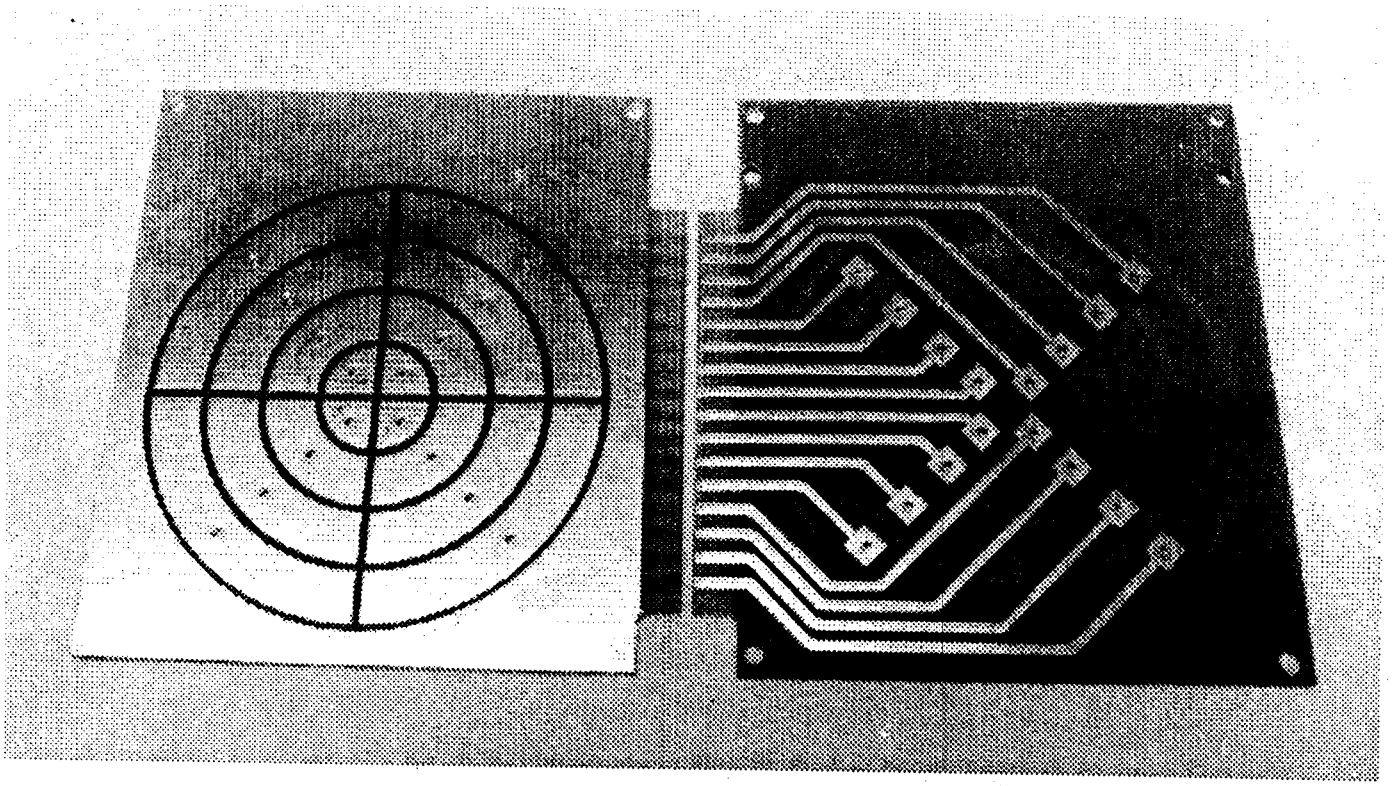

Figure 1. Front and Back of the Sectored Faraday Cup

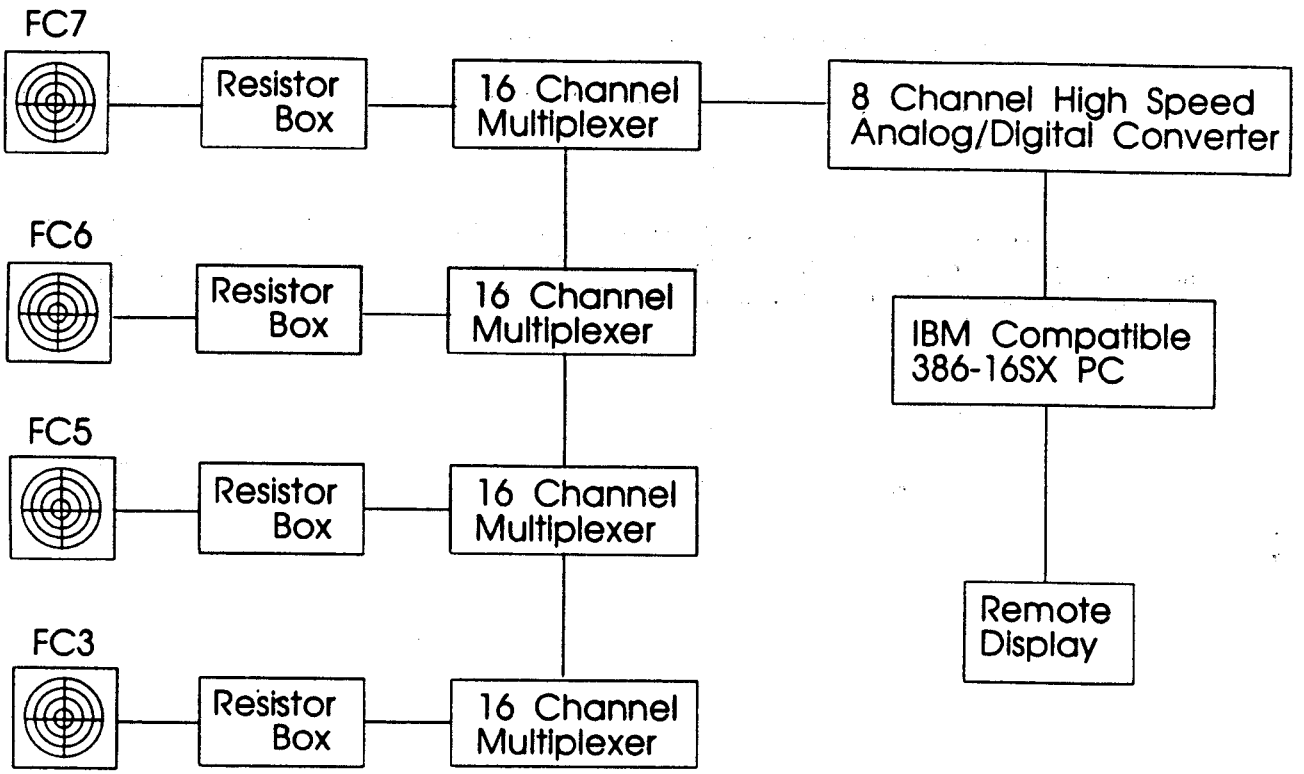

Figure 2. Schematic of the injection line showing FC locations, pc location and indicating remote display

K1200 CYCLOTRON DEFLECTOR DEVELOPMENT

T.A. Antaya, G. Horner, D. Poe and P. Miller

We would like to describe briefly our plans to further increase the performance of electrostatic deflectors in the K1200 cyclotron, in order to achieve both higher energy and intensity beams.

Operating Requirements

We have recently produced Q/M=1/2 extracted beams at 170 MeV/n, and internal beams to full radius at 200 MeV/n. The voltage limits of the electrostatic deflectors appear to be the only constraint on the production of a 200 MeV/n extracted beam from the K1200 cyclotron. The present pair of electrostatic deflectors operates reliably at levels of 60 kV over a 6mm gap, sufficient for 170 MeV/n, but must rise to about 70 kV to extract a 200 MeV/n beam.

Running intermediate energy beams, e.g., $^{18}O^{6+}$ at 80 MeV/n at high intensity, we have observed beam induced degradation of deflector voltage holding limits. The present intensity limit is around 200-400 enA of extracted beam, when the extraction efficiency is about 30%. To some extent this effect is exacerbated by the small deflector gap, but mainly the effect is thought to be thermal, given that the observed increase in leakage current is a slow process. Neither deflector cathodes nor deflector housings, with the exception of the EIA housing, have direct water cooling.

Deflector Development Issues

The technical areas to address in pushing the deflector performance include:

1.) Preparation: alignment, cleaning and conditioning

2.) Operating Environment: vacuum constituents, magnetic field, rf fields

3.) Insulator Breakdown

4.) Vacuum Breakdown

5.) Accelerated Beam Effects

Deflector preparation to run at high voltage is always an issue, and a number of techniques have been developed at NSCL to prepare and condition deflectors. At present, we have no plans to alter any of those techniques.

The operating environment is also critical, so we plan to use the K500 cyclotron for proof testing new hardware designs. The K500 cyclotron will be operated primarily as a high field test stand, i.e., magnet on and under vacuum, but no rf field and beam. Beams are available from the ECR sources, however; so deflector testing with beam is possible where important, if it is determined to be feasible to operate the full K500 system.

Cathode insulator development is one area in which it is possible to move rapidly off line, because insulators are easily tested in a small test stand, and also because it is difficult to isolate insulator limits from metal

sparking limits in the full deflector assemblies. We have recently switched to a fluted macor insulator design, after comparison testing, and this has helped to establish the present deflector operating limits [see the separate Annual Report contribution: "K1200 Deflector Insulator Tests"]. Generally, our plan is to test new insulator concepts in the TASCC deflector materials test stand at Chalk River Nuclear Laboratories. We are presently developing a 'greened' alumina insulator, as a potential improvement over the fluted macor insulators.

The proper selection of cathode and anode materials is a complex problem. At present we have anodized aluminum cathode shoes and stainless steel sparking plates. Chalk River reports better success with an all electropolished stainless steel system[1], while Texas A&M is working on an all-anodized titanium design[2]. Electropolishing presumably reduces field emission by the elimination of micro-projections. Anodizing perhaps achieves the same result by the 'insulation' of the metallic emission surface. Stainless steel is a good vacuum material but has thermal dissipation and weight problems (for large shoes). Surface wear and secondary electron enhancement issues may limit the effectiveness of the anodized cathode shoes.

K500 5mm Gap Deflector Test

The K250 proton therapy cyclotron presently under construction at NSCL requires 100 kV/cm extractions fields. Since it is expected that the proton beam size in that cyclotron will be small, using a 5mm gap should be possible. In order to test this concept, the two K500 cyclotron deflectors were modified to reduce the gap between the shoe and septum to 5mm, and then tested to determine voltage holding characteristics. The E1 deflector gap was reduced by spacing its original macor insulators toward the septum with washers. The gap in E2 was reduced by using the fluted macor insulator design now used in the K1200 cyclotron. Both deflectors were installed and the cyclotron was pumped down to $1x10^{-6}$ Torr. The deflectors were first conditioned without magnetic field to 50 kV and then conditioned with a magnetic field of about 3.5 Tesla, up to the voltage holding limit.

Table 1 summarizes the B=0 and B=3.5 Tesla kG conditioning of E1 and E2. Generally, E2, with the fluted macor insulators, had lower leakage current at a given voltage. E2 also achieved a 20% higher field strength of 120 kV/cm. However both deflectors did reach the required deflector field strength for the K250 prototype cyclotron.

	E1 (kV)	E1 (A)	E2 (kV)	E2 (A)
B=0	50	59	50	30
B=3.5 Tesla	35	5.6	35	3.8
	40	98	49	53
	52	125	56	34
	50	141	60	201

Table 1.

Water Cooled Vacuum High Voltage Feed Through

We want to move in the direction of water cooled shoes, both to reduce field emission and to mitigate the effects of beam power dissipation in the deflectors. Figure 1 shows the initial K500 test configuration of a K1200 water cooled vacuum high voltage feed thru. This new high voltage feed thru is shown attached to a simplified short straight test deflector. (The short, straight test deflector incorporates most of the important voltage limiting features, except a long curved shoe, which should allow us to make quick design changes during the development process.) Low conductivity water (LCW) is circulated around a standard high voltage cable, through a resistive water gap, to a spray tube assembly inside of the high voltage rod end. The resistive water gap will replace the external surge resistor, that decouples the cable capacitance from the deflector capacitance to limit energy deposition during sparking[3]. As can be seen, in this design, cooling water is stopped before the deflector cathode, so we are mainly testing vacuum isolation, water flow and resistance, dielectric strength and voltage holding of the feed thru design itself. Should this design prove successful, the transition to direct cathode water cooling will be made in a subsequent step.

Superconducting Cyclotron Deflector Development Collaboration

We have created an anonymous ftp site to serve as a repository for deflector development data at the compact superconducting cyclotron laboratories. To reach the system:

$ftp megapc.nscl.msu.edu
Name: anonymous
Password: your email address

Once logged in, change the directory to *pub/deflector*. A descriptive index of this directory will be found in the text file *readme.index*. The direct address of megapc is 35.8.32.181 if your domain server does not have a symbolic translation for megapc. Questions about the system should be sent to *antaya@ megapc.nscl.msu.edu*.

References

1. W.T. Diamond, et.al., Proc. 13th Int. Conf. on Cyclotrons and Their Applications, Vancouver (1992) 569.
2. R. Rogers, Texas A&M University, private communication.
3. T.A. Antaya, et. al., IEEE Trans. Nucl. Sci. NS 28 (1981) 2982.

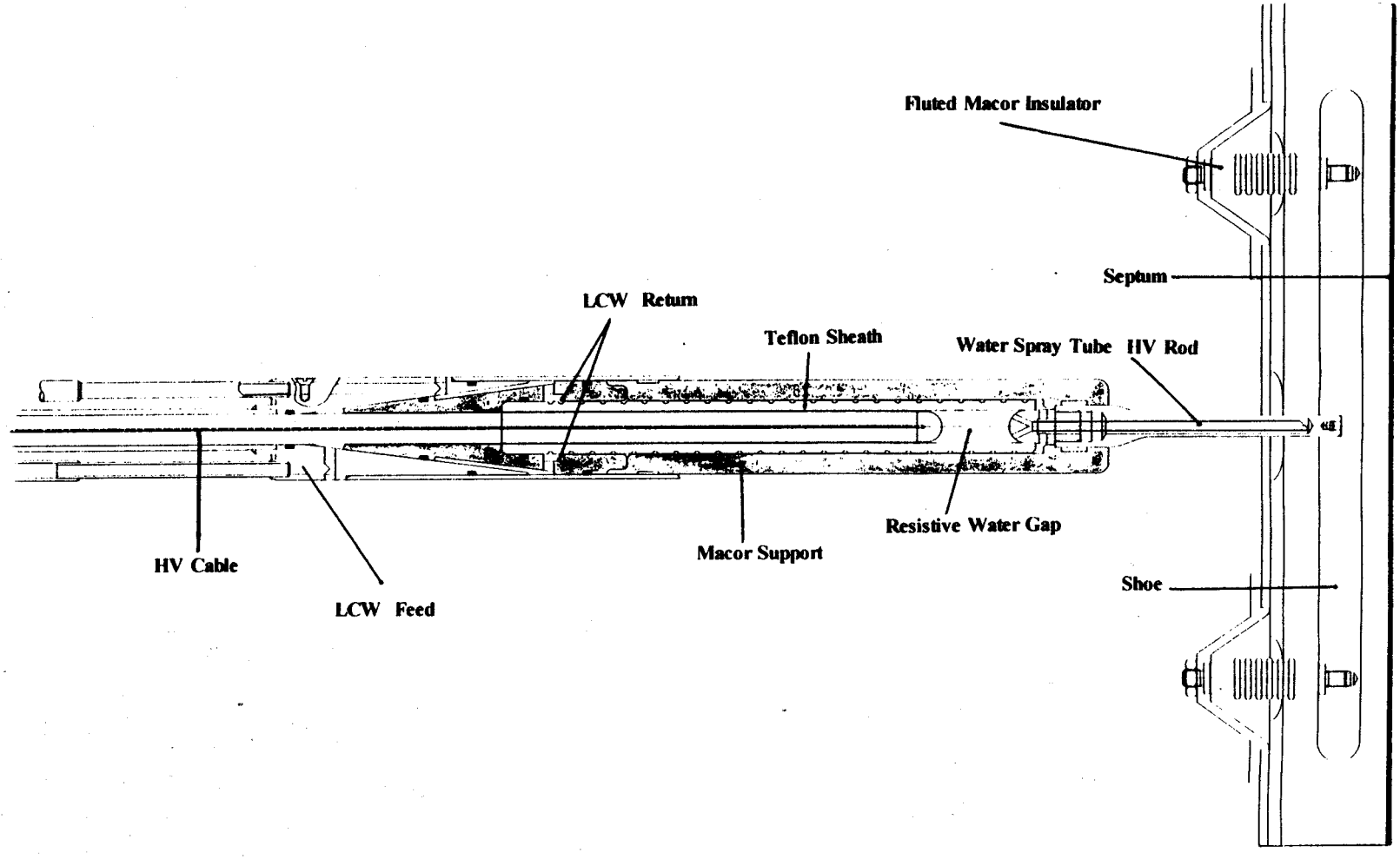

Figure 1: The K500 test configuration for a water cooled high voltage feed thru design for K1200 deflectors is shown.

K1200 DEFLECTOR INSULATOR HIGH VOLTAGE TESTS

W. Diamond, * D. Poe and T.A. Antaya

Introduction

In this report we will describe voltage holding tests of various K1200 cyclotron deflector support insulators, performed in the TASCC high voltage materials test stand at Chalk River Nuclear Laboratories (CRNL). Instances of these insulator types are either now in use, or have previously been used to support K1200 deflector cathodes. The purpose of the present effort is to compare the voltage conditioning characteristics and the voltage holding limit of each insulator type. For comparison purposes, we also tested a 'greened' alumina insulator not of K1200 design, but having very good performance. This surface treatment of alumina is a promising new technique that has been developed at CRNL [1]. The results of this test will also be reported.

Test Insulator Set

Figure 1 shows the K1200 insulator designs to be tested. Insulator type-A is a 0.312 diameter Macor insulator with titanium end caps. The end caps are attached via a solder-glass fusion. The metallic end caps fill the deflector shoe counter bores to give a 'planar' transition from metal to insulator. Insulator type-B is dimensionally the same as type-A, but using alumina insulator material and molybdenum end caps, attached to the alumina by brazing in a 50 torr argon atmosphere using active metal brazing alloy. Insulator type-C is a new fluted Macor design. It consists of a 0.375 inch flute base diameter, a 0.5 inch flute diameter and titanium end caps. It requires a modified deflector cathode with 0.375 inch mating counter bores. The sapphire insulator type-D is an earlier K1200 deflector insulator design and is included for comparative purposes. These sapphire insulators have been observed to have a peculiar failure mode in which the insulator is observed to glow during breakdown. [2] We wanted to know if we could learn more about this failure mode-- what was the onset voltage; and during failure, could we distinguish between surface and volume discharges? To make a sapphire insulator assembly, the sapphire ends are first metalized with Mo-Mn-W paint in a wet hydrogen atmosphere, then nickel electroplated using a "watts" bath. The molybdenum end caps are also nickel plated prior to brazing. The assembly is then brazed in dry hydrogen using a 72% Ag-28%Cu alloy. We also tested a 0.25 inch diameter by 0.68 inch long alumina insulator (sans end caps) in the test stand as well. This insulator had previously been 'greened' at CRNL to produce a resistive surface coating of chromic oxide.

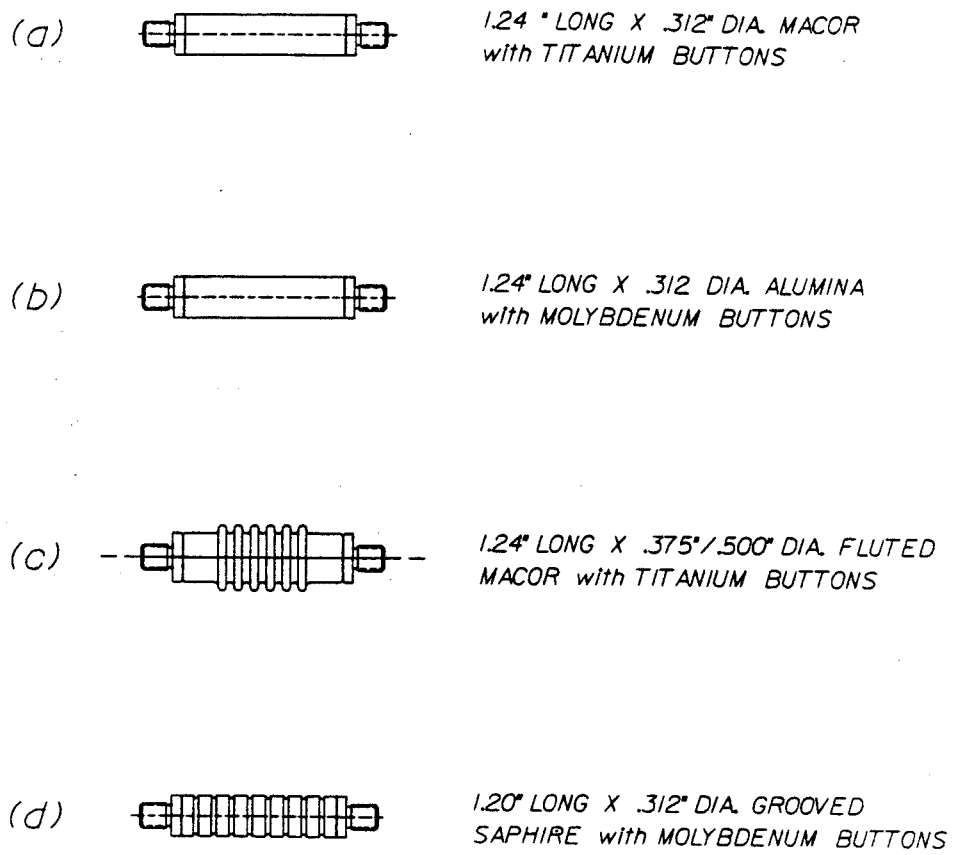

Figure 1: The four K1200 insulator designs tested in the present study are shown.

High Voltage Test Stand

The deflector materials high voltage test stand is shown in (highly) schematic form in Figure 2. The high vacuum test chamber mounts in the bore of an Alpha Scientific symmetric H-magnet. This magnet produces a gap peak field of about 6 kG.

The test stand cathode and anode have detachable end pieces. For these tests a set of end pieces were modified to hold the ends of the 0.312 inch diameter NSCL insulators, with the insulator end caps recessed, so that the insulator end is tangent to the end piece surface, as shown in Fig. 2. The chamber is pumped by a turbomolecular pump and achieves a base pressure of about 10 -7 Torr.

The test chamber has a number of available diagnostics. The upper and lower sparking plates and the anode are isolated from ground, permitting current monitoring, by converting currents to voltages which are then displayed on an oscilloscope. In the plane perpendicular to Fig. 2, x-ray and visible light emission from the high voltage region are monitored.

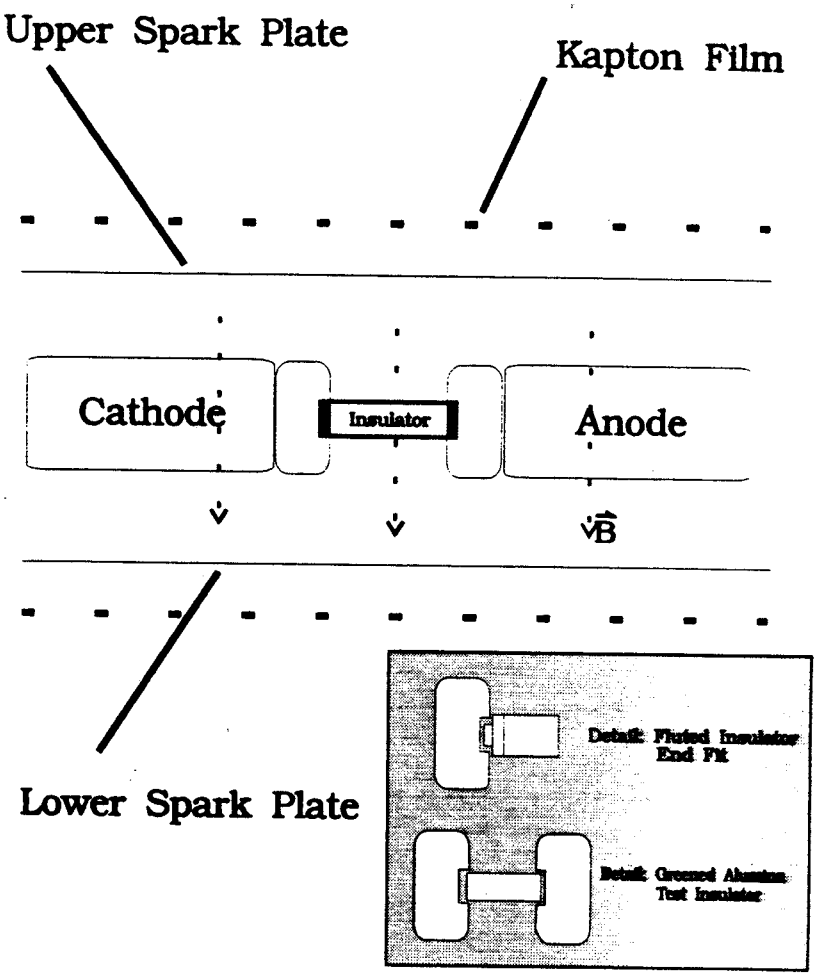

Figure 2: The TASCC Deflector Materials Test Stand is shown in schematic form for the testing of K1200 style 1.24 inch x .312 diameter macor or alumina insulators. The inset shows non-standard test configurations--see text for details.

Operation of the Test Stand

With floating spark plates and anode, it is possible to observe collected emission currents and their correlations with x-rays and photons. During HV ramping, the sparking plates generally had low average currents, ($\leq$ 10 microamps) but cathode sparks to ground would cause large excursions of the current on the sparking plates, and thus became a convenient way to separate average emission from sparking. During sparks, large increases in x-ray and visible light flux were also observed.

Raising the cathode voltage above the present conditioned level generally resulted in an increase in both visible light and x-rays, indicating increased cathode emission, even when sparking was not observed. Over a period of a few minutes, this emission would tend to die down. But in all tests, at the highest attained voltage, frequent cathode sparking was observed.

The cathode was isolated from the power supply by a water resistor of the type used in the Chalk River cyclotron deflector [3]. The resistance is approximately 20 megaohms. This resistor may have aided the testing by limiting spark plate damage during cathode sparking at high voltage, as no deep pits in the spark plates were ever

observed. However, the applied magnetic field of about 6 kG is low relative to that of superconducting cyclotrons, and may also be a factor in the limited damage observed. The presence of the water resistor in the HV vacuum feedthru to the test stand complicates a determination of the leakage current measurement, which has to be corrected for the resistor current.

The chamber pressure was typically in the low 10^{-6} Torr range during testing. This represents an increase in pressure of about 1 order of magnitude over the base pressure during testing. (Given that we were testing single insulators and not whole deflector assemblies, this large pressure increase was somewhat surprising, and suggests even more caution when trying to condition complete deflector assemblies.)

Insulator Type-A Testing

The type-A insulator initially conditioned to a leakage current of 50 microamps at a voltage of 60 kV. While at 60 kV we shut the magnet off to observe differences in cathode emission, and the cathode immediately began sparking to ground across the insulator to the anode. The voltage was reduced to 50 kV, but sparking continued. Turning on the magnet stopped the sparking, and the voltage was then ramped back to 60 kV. At 60 kV, continuous sparking was observed and the test was halted. The insulator was then removed for inspection. No visible damage or discoloration was observed, but a small crater in the surface near the HV end was observed under a microscope, which one of us (W.D.), considered to be a likely cause of the failure.

The insulator failure after shutting off the magnet was a surprise. At NSCL, we often re-condition failed deflectors *in situ* by raising the voltage with the magnet off. (It is thought that spark plate damaged induced during sparking at high field can be 'healed' by B=0 conditioning, but this has not been confirmed.) Here we have a situation where B=0 operation was clearly deleterious. What is probably important here is the B=0 insulator conditioning is different from B=6 kG conditioning, because the insulator is mounted perpendicular to the magnetic field. So, with some magnetic field, electron motion across the insulator surface to the anode is impeded. With B=0, electron motion across the insulator surface to the anode is actually preferred, making insulator tracking possible. The failure of the type-A insulator in our test would imply that B=0 conditioning is the more difficult case for insulator conditioning.

Insulator Type-B Testing

The insulator was ramped initially to about 60 kV and very large fluctuations in emission current (and all other observables: photons, x-rays, sparking plates) were observed. This insulator was clearly conditioning-- at each new voltage the total leakage current would increase when the present operating level was exceeded, and then drop, stabilizing finally at 50-75% of the initial leakage current at that voltage. It was not clear that we could go much

higher than 60 kV with the magnet on, so we started over with B=0 to condition the insulator. With B=0, the insulator did go all the way to the power supply limit of 100 kV. Again the deflector was observed to have numerous conditioning excursions. Finally the magnet was turned on, and the insulator was ramped successfully to 100 kV.

After testing, this insulator showed evidence of substantial emission from the area of the brazing material wetted alumina on the cathode side: the wetted areas and alumina were discolored and some brazing material transport to previously clean areas of the alumina were observed. However, the insulator nevertheless conditioned to 100 kV.

Insulator Type-C Testing

For this insulator, the high voltage could be raised to 100 kV with the magnet on, faster than for insulator type-B, with fewer conditioning events as well, and overall lower emission current.

The planar mounting scheme of these insulators, as exemplified by the standard mounting arrangement in Fig. 2, was intended to minimize emission at the junction of cathode to insulator [4]. As tested, insulator type-C did not meet the design criteria, because the type-C end caps did not fit into the electrode tips sized to fit .316 inch diameter end caps. Since the exposed insulator end caps effectively become a cathode projection, the field at the high voltage insulator end is enhanced, and a degradation of performance would be expected. The contrary was observed--at least, if there was some degradation, it occurs above the 100 kV operating level.

Insulator Type-D Testing

The grooved sapphire insulator is a previous NSCL design and was included for testing completeness. This insulator reached the 100 kV power supply limit, but with about twice the emission current as the fluted macor insulator. The grooves in this insulator are designed to reduce electron transport across this insulator, and that is evidently not as successful as fluting for reducing emission current. No evidence for the 'glow ' failure mode was observed.

'Greened' Alumina Insulator Testing

The support insulators and the high voltage vacuum feedthru insulator of the Chalk River cyclotron deflector are 'greened' alumina. Insulators are painted with CrO_3 and heat treated--the resulting baked-on green

CrO_2 layer is resistive. It is believed that this coating inhibits charge accumulation on insulator surfaces that can lead to electron cascades, tracking and sparks. A small sample insulator of 0.25 inch diam. x 27/32 inch long of this type was available and we tested it for comparison purposes.

This insulator was smaller diameter than the standard NSCL insulators, leading to another mis-match when mounting in the test stand, as also shown in the inset in Fig. 2. It was also shorter, having no end pieces. When mounted in the test stand, the net gap between the cathode and anode was only 0.68 inches, about 55% of the 1.24 inch gap of the standard NSCL insulators.

The insulator ramped to 85 kV in about 20 minutes with little conditioning. We stopped the test at 85 kV, where the electric field strength achieved was about 1.5 times higher than that for standard length NSCL insulators operating at 100 kV, in order to preserve the insulator (to bring it back to NSCL for further study!)

Summary and Conclusions

Table 1 summarizes the voltages attained and the corresponding leakage currents and electric fields at peak voltage. It is evident from this study that greened alumina insulators are worth investigating. It is also evident that type-C fluted Macor insulators with 1/2 inch diameter flutes, give comparable performance that is superior to the other NSCL designs tested--less conditioning, lower emission current and less sparking. While the type-B insulator eventually achieved 100 kV with low leakage current, the long conditioning cycle required would be prohibitive for a full deflector set of 6 insulators.

We came back with a new appreciation that the insulators themselves require careful high voltage conditioning, and this conditioning is sensitive to the presence or absence of an applied magnetic field. Finally, we note that testing only one insulator of each type hardly constitutes a reliable sample, and these results are probably sensitive to the preparation and handling of this particular set. There was also a variation in test cycle procedures, and this probably also has affected the results obtained.

a. Tandem Accelerator Superconducting Cyclotron, Chalk River Laboratories, Chalk River, Ontario.

References

1. W. Diamond, 13th Int. Conference on Cyclotrons and Their Applications, Vancouver, (1992), to be published.
2. J. Nolen, NSCL; B. Rodgers, TAMU--private communication.
3. B. Rodgers, Workshop on High Voltage Deflectors for Superconducting Cyclotrons, MSUCP-66, (1992).
4. T. Kuo, private communication.

Insulator	Max Voltage (kV)	Leakage Current (euA)	Max Electric Field (kV/cm)
Type-A	60 [1]	50	19
Type-B	100 [2]	40	32
Type-C	100 [2]	100	32
Type-D	100 [2]	150	32
Greened Alumina	85 [3]	40	49

1. Insulator failed at this voltage
2. Test-stand power supply limit reached.
3. Arbitrary voltage limit set to preserve insulator.

Table 1: Performance of Tested K1200 Deflector Insulators

CURRENT STATUS OF THE K1200 RF SYSTEM

F. Pigeaud, J. Brandon, W. Nurnberger and J. Vincent

The K1200 RF System operated for approximately 6500 hours during the 1992 calendar year as shown in figure 1. During this past year construction was completed on the NSCL designed Phoenix Power Supply which provides final anode bias to the three transmitters. No other significant changes were made to the RF System which operated reliably while being pushed toward its upper operating limits.

Electronics

Work has begun on converting both the dee fine tuner and input coupler systems from hydraulic motors to "bang-bang" servos. The hydraulic servos have operated adequately in the past, but several improvements in the operation and maintenance of the system can be made through this conversion. Some of the negative aspects of the hydraulic servos are their leaky cylinders which require regular maintenance, and the feedback loop which causes the servo to constantly 'search'. Additionally, during sparking events, the dee fine tuners deflect wildly before finding their proper set point. All of these problems will be addressed by using bang-bang DC motors which simply turn on and off when their error signal reaches a given magnitude. The speed of these devices is sufficient and the motors have run reliably in the magnetic fringe field of the cyclotron operating at maximum current. The design should be completed and implemented during 1993.

Final Anode Power Supply

The NSCL Phoenix Power Supply was completed this year with the addition of the Power Converter Cabinet. As described in last year's annual report, this element of the power supply system houses the rectifier stacks, filter choke and step-start circuitry. All the components operate in air and are housed indoors for easy maintenance and troubleshooting. This is a great improvement over the original factory assembly which submerged the choke and rectifiers under oil in an outdoor tank. After installation in the Fall of 1992, extensive testing and analysis was completed to ensure the supply operated as designed. The results of the analysis along with a complete description of the power supply have since been compiled into an operating manual. The

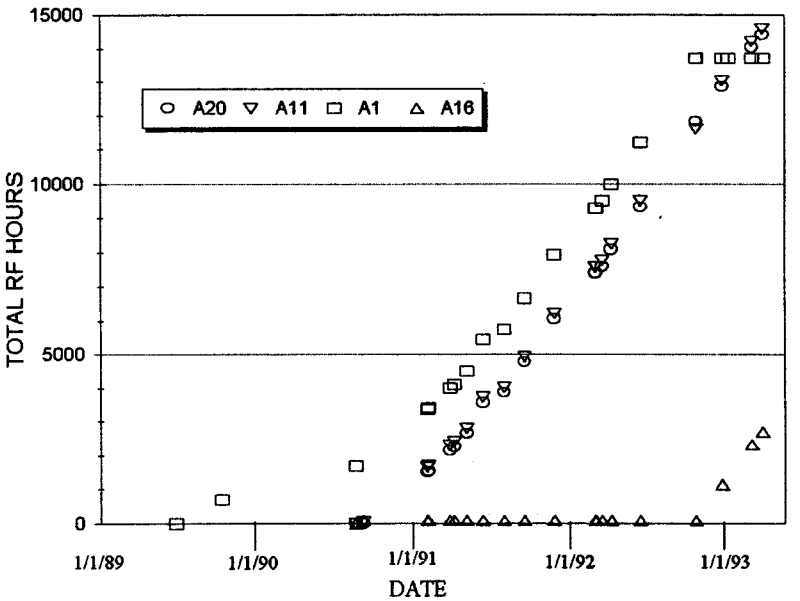

Figure 1: Total K1200 RF hours for each TH555 tetrode. The tubes are plotted by serial number, where A1 was the unit used during development. The four tubes have been interchanged between the three transmitters and storage , so the graph reflects RF hours of tetrode, not transmitter, operation.

final anode power supply chain is now complete with all the control cabinets and a backup transformer in place.

Conclusion

For the past two years we have run at a steady, predictable rate of 5500-6500 hours of RF operation per year with filament operating times of approximately 6500-7500 hours (The filament times are greater because they are usually left running in a lower current standby mode which extends their useful life). This data will be useful for predicting mean time to failure for the power tetrodes so this costly item can be appropriately budgeted in the future. At the present we do not have a good estimate for the filament lifetime of the Thomson TH555 power tubes, and they have not shown any of the signs of reduced performance which often precede tube failure.

In the last few years, two major RF projects have been completed: the Phoenix Power Supply and the redesigned amplifiers, which have both made the K1200 RF System a thoroughly understood, reliable, and easily maintainable system Although the large scale work has been completed, smaller upgrades can be expected in the coming years to augment this performance.

SCECR STATUS AND DEVELOPMENT

T.A. Antaya, D. Cole, K. Harrison, P. Osborne and K, Willard

While difficulties with both the 14.5 GHz transmitter and the hexapole have limited development of the 14.5 GHz, we have used this time to fully commission the Superconducting ECR source (SCECR) for operations, and begin a careful comparison of it with the Room Temperature ECR source (RTECR) at 6.4 GHz.

The RTECR is an exceptionally robust ECR source. It operates about 5000 hours per year, running largely unattended and self-protecting after each tune. The only component failures on the RTECR in the past few years have been turbomolecular pump bearings! Any new ECR source at NSCL must compete against a very high standard.

From an operations standpoint, the SCECR is also a stable, reliable ion source with a wide dynamic range for tuning--perhaps too wide. One question often asked is how is an ECR source limited by the cryogenics system. There are no operational difficulties with the cryogenic system. The SCECR magnet liquid helium feed system requires no adjustment. The cryostat operates isolated from vacuum pumps. The lack of heat associated with the generation of high magnetic fields, makes the source operating environment simple and robust.

Figures 1 and 2 show the optimized performance of the SCECR relative to the RTECR, for oxygen and neon. As can be seen, the high charge state performance of the SCECR is significantly better than the RTECR for these two species. For oxygen 7+, 6+, and neon $\geq$7+, the SCECR performance represents a 'world best' for a 6.4 GHz ECR. Table 1 summarizes the differences in the 'tunes' of these two sources for oxygen. Note that the SCECR total extracted current is higher, while the required microwave power is lower. Evidently, the energy lifetime in the plasma is higher, primarily a consequence of the higher operating radial magnetic field. In the SCECR, the hexapole is dynamically tunable. All optimized tunes of the SCECR have a radial magnetic field higher than that of the RTECR. Finally we note that the radial Xray emission from the SCECR approaches zero as the hexapole field increases, implying significantly increased confinement in the radial direction.

For high charged ions of any species, the RTECR has a similar tune: the axial magnetic field is roughly constant, the support gas is oxygen, the plasma chamber walls have a SiO_2 layer, and the operating pressure is about $9x10^{-8}$ torr. Generally the tuned parameters are the microwave power, ranging from 400-800 watts, and the mixture of the feed and support gases (or the solid feed rate and the support gas). And of course the radial magnetic field is fixed. The SCECR tune appears to be Z dependent. Figure 3 shows the optimized microwave power for the high charge state ion tuning from oxygen to xenon. The power required is seen to increase as the ion charge (or Z) is increased.

At present, the highly charged ion performance of the SCECR at 6.4 GHz exceeds that of the RTECR for light species, and we have preliminary tunes for argon and xenon. For argon, the SCECR performance exceeds the RTECR up to about 12+, and we are working on the tune for 13+-16+. We plan to continue to 'work up' the periodic table at 6.4 GHz until all systems are ready for source optimization at 14.5 GHz.

	RTECR	SCECR
B_{wall}	0.3 T	0.6 T
P_{rf}	400 W	90 W
I_{total}	0.5	2.0
XRAYS	> 1R/hr	< 10 MR/hr

Table 1: RTECR vs. SCECR settings for HCS oxygen tune.

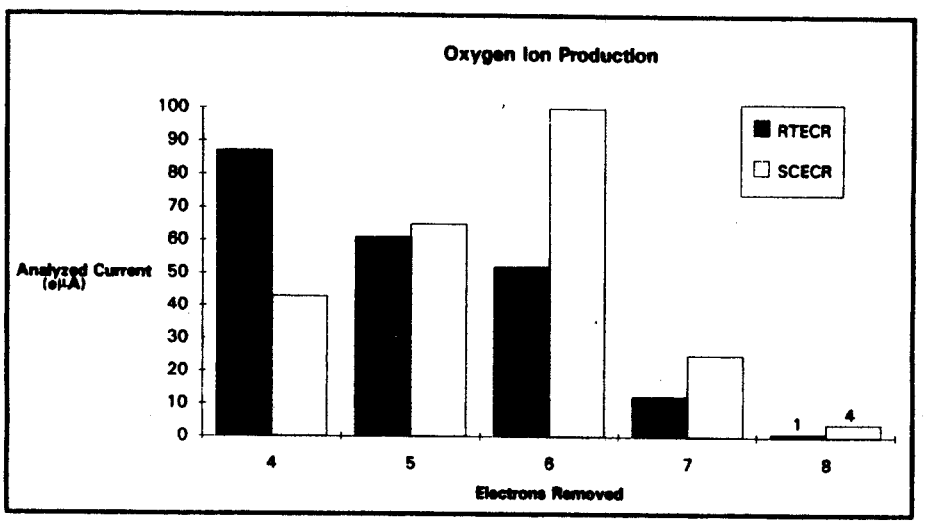

Figure 1: The best performance for oxygen ion production of the RTECR is compared to a high charge state tune of the SCECR.

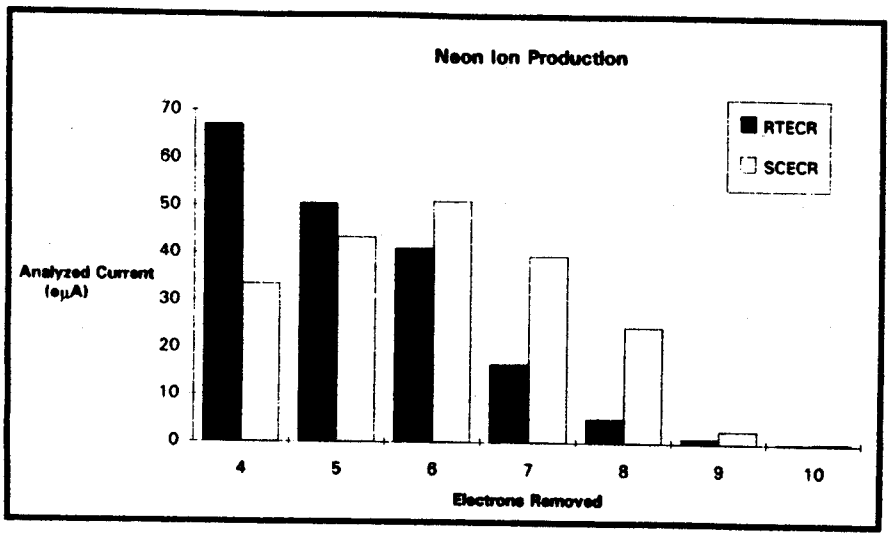

Figure 2: The best performance for neon ion production of the RTECR is compared to a high charge state tune of the SCECR.

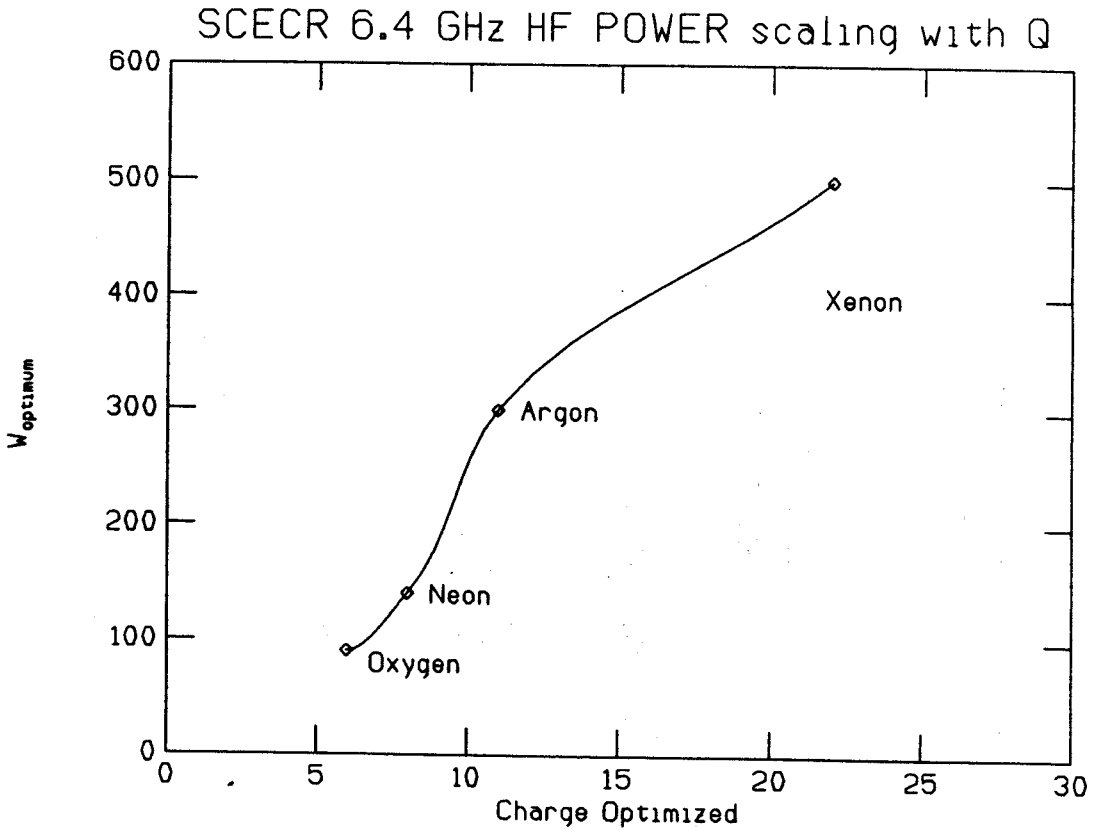

Figure 3: The microwave power required for highly charged ion tunes of the SCECR scales systematically with the charge optimized.

CPECR IONIZER CONFIGURATION

T. A. Antaya

With the success of the A1200 fragment separator, there is increased interest in more exotic primary beams, including radioactive species, such as ^{3}H or ^{14}C. The production of beams of radioactive species is greatly simplified if the ionization efficiency can approach unity. Our RTECR Super Gas Mixing technique for metallic species has such high efficiency, but results in a highly peaked charge state distribution with low intensity in any given charge state. And it will not work at all for low or intermediate charged ions.

For the purposes of the study of bulk ionization efficiency of low charged ions, we will introduce a third configuration for the CPECR in 1993, as shown in Figure 1. The metal vapor oven and the oven chamber vacuum pump are removed, and a small bore quartz tube is inserted in the main stage plasma chamber. The main stage is still pumped by off-axis slots in the extraction electrode, and will operate at low pressure ($\leq 10^{-7}$ Torr) to avoid the formation of a plasma outside the quartz tube. The quartz tube is pumped only through the 8mm diameter aperture in the extraction electrode, in order to reduce the gas flow rate required to achieve a given operating pressure.

The addition of the small bore quartz tube has a number of important consequences. First, it substantially reduces the radial confinement time, which will suppress hot electrons and highly charged ions. (An important loss mechanism for low and intermediate charged ions is their further ionization!) Second, the quartz tube is more chemically inert than the copper plasma chamber. Finally, the quartz tube will operate at elevated temperature, which should reduce sticking times.

At the present time, the hardware needed to perform this transformation is complete and awaits only a slot in the operating schedule to install it in the CPECR and perform measurements. A careful comparison of the ionization efficiency of this reduced ionization configuration with that of the more conventional gaseous feed configuration of the CPECR will be performed.

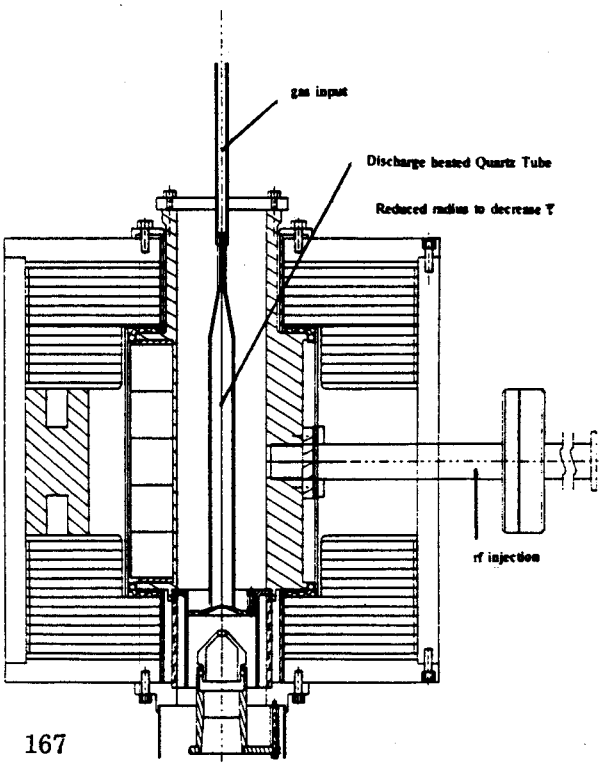

Figure 1: A prototype radioactive gas ionizer configuration for the CPECR.

METALLIC ION BEAM DEVELOPMENT ON THE RTECR

Dallas G. Cole and Timothy A. Antaya

Introduction

Production of metallic ion beams from typical solid feed or metallic vapor oven procedures, though often workable, can introduce difficulties associated with excessive and/or unstable consumption rates. Such difficulties as plasma instability, general source contamination, and uneconomical consumption rates preclude or make unattractive the regular use of expensive and rare feed materials such as highly enriched separated isotopes. A technique has been developed which allows the introduction by solid feed of very small quantities of pure metals or metallic compounds yielding extremely low feed material consumption rates, no appreciable source contamination, and good charge state distribution.

Sample Preparation

In this technique, which we have named 'Super Gas Mixing', minimal samples of pure metal powder feed material are supported on the end of a 3 mm diameter Alumina rod. By pressing the rod end into a small mound of metal powder a small 5 to 10 mg pellet or thin plate forms and adheres to the rod. Metallic compounds which may adhere less well to the rod's smooth end surface are tamped into the end of a 3 mm diameter Alumina tube with a 1 mm diameter bore. The resulting plug weighing 0.5 to 5 mg is well supported and flush with the tube end. In either case the Alumina support with sample is mounted on the end of a linear drive rod. The linear drive rod is then attached to RTECR midplane vacuum feedthrough where a servo drive unit with a precision position readout is used to carefully position the sample for interaction with a pretuned high pressure oxygen plasma as shown in figure 1. The feed sample becomes in effect a trace contaminant in the oxygen tune hence the name 'Super Gas Mixing'.

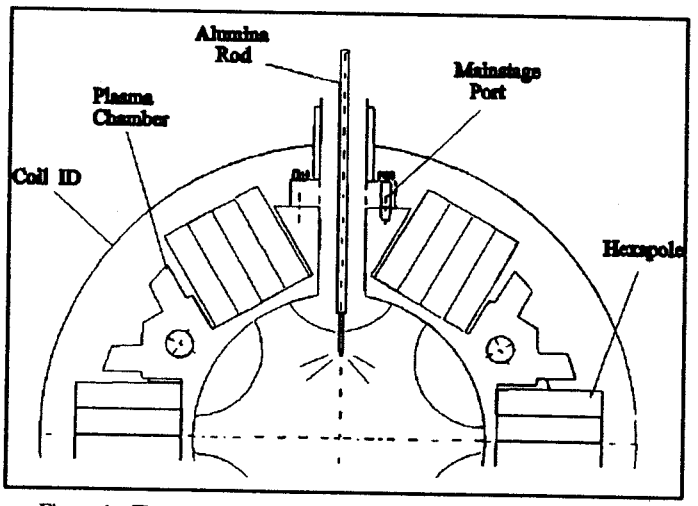

Figure 1. The metallic sample is inserted into the main stage plasma.

Alumina rod supports have been successfully used with Nickel, Molybdenum, and Uranium samples. Alumina tubes have worked well with Cr, Au, LiF, MgO, and CaO samples. While most samples have exhibited long lifetimes, in some cases exceeding 100 hours, the recycling time associated with the introduction of a renewed sample is typically one hour.

Super Gas Mixing

Pretuning of the RTECR for this technique consists of establishing a high pressure oxygen plasma yielding a strong high charge state tune of a noble gas species near the mass of the metal feed material. When this is complete the noble gas feed to the plasma is shut off and the metal sample is introduced to the plasma. It is presumed that a recycling mode is established when the feed material begins a coating effect on the plasma chamber wall which becomes a secondary source of metal feed to the plasma. Care is taken to keep the plasma interaction with sample minimal until a recycling mode is apparent as characterized by the appearance of the metal ions in the charge state distribution, and stability in the ECR source pressure and total extracted current. This technique offers high charge states, little source contamination, and minimal consumption. Typical consumption rates are for U <.14 mg/hr and for ^{48}Ca .07 mg/hr. Some K1200 heavy ion beams and intensities achieved using this technique are shown in Table 1.

Table 1. Some K1200 record Heavy Ion Beams

Ion	Energy	Pretune Species	Intensity pnA
$^{48}Ca^{16+}$	100	^{40}Ar	.11
$^{58}Ni^{15+}$	70	^{84}Kr	4.6
$^{92}Mo^{25+}$	70	^{84}Kr	.02
$^{197}Au^{35+}$	35	^{129}Xe	.001
$^{238}U^{39+}$	25	^{129}Xe	.0004

Conclusion

The technique of Super Gas Mixing produces metallic ion beams with charge state distributions comparable with the high charge state distributions and overall performance of the pretune gas species. Minimal consumption of the feed sample along with long sample life makes the production of many metallic beams such as those requiring expensive and/or rare separated isotopes a reasonable undertaking.

SUPERCONDUCTING BEAMLINE QUADRUPOLES AND DIPOLES

J.C. DeKamp, C.T. Magsig, and A.F. Zeller

The quadrupole triplet and dipole cryostats for the S800 beamline now have their basic overall design outlined and detailing of the cryostat parts is beginning. This beamline will transport beams to the S800 spectrograph[1,2] presently under construction. The magnet designs were already complete and the magnet steel in house as previously reported[3]. A cryostat for testing the first 20.3 cm. aperature quad is also being constructed. In addition, the dipole which bends beams into the N4 experimental vault and will also bend into the S800 beamline and the S2 experimental line presently under construction has been rebuilt and is operational. The S2 beamline quadrupole doublets have also been constructed and installed. A spare quad triplet, dipole core assembly, and a new quad doublet are under construction for the A1200 beamline[4], as well as a quad doublet for the S800 beamline.

Dipole Construction

The dipole at position D165 was rebuilt after having operation problems due to shorted turns in one of its potted superconducting coils. It was replaced for a time with a resistive dipole. This dipole was not capable of bending our highest rigidity beams and also consumed a lot of power (72 kW) and was only intended as a temporary replacement. The dipole will see a high duty factor in the future when it services the S2 and S800 experimental areas in addition to the N4 area. This region is shown in Figure 1. The rebuilt superconducting dipole is now installed with the N4 beamline back in service. It is 30% more efficient cryogenically since being rebuilt. Its design was modified to allow a faster cooldown time by using the space in the bobbin between the coils for LHe, giving a large enough volume so that LHe can be fed directly into the bobbin during a batch fill without the initial heat pulse causing a quench. Previously the LHe was fed into the batch fill container, which absorbed the heat pulse, and flowed into the bobbin by virtue of its own pressure head. This caused no problems for operation but did extend the initial cooldown time. It now cools in 16 hrs from room temperature compared to 84 hours previously. We are using this same design on the new S800 beamline dipoles. A spare dipole poletip/bobbin cryostat assembly is being built for the A1200 line. If this line goes down operation to experimental areas cannot occur. Having a spare dipole magnet core assembly allows down time to be reduced from 6 months to less than 2 months in case of a failure.

The S800 beamline dipoles have had their gap increased by 2 cm to 7 cm. This has made it

necessary to remake some of the coil bobbin parts which are already in house but otherwise has little effect on the design. The upper cryostat, which contains the batch fill containers is presently being detailed. Coil winding will begin in May, 1993, but will take only 2 months to complete. All 4 dipoles are forecast to be complete by July, 1994.

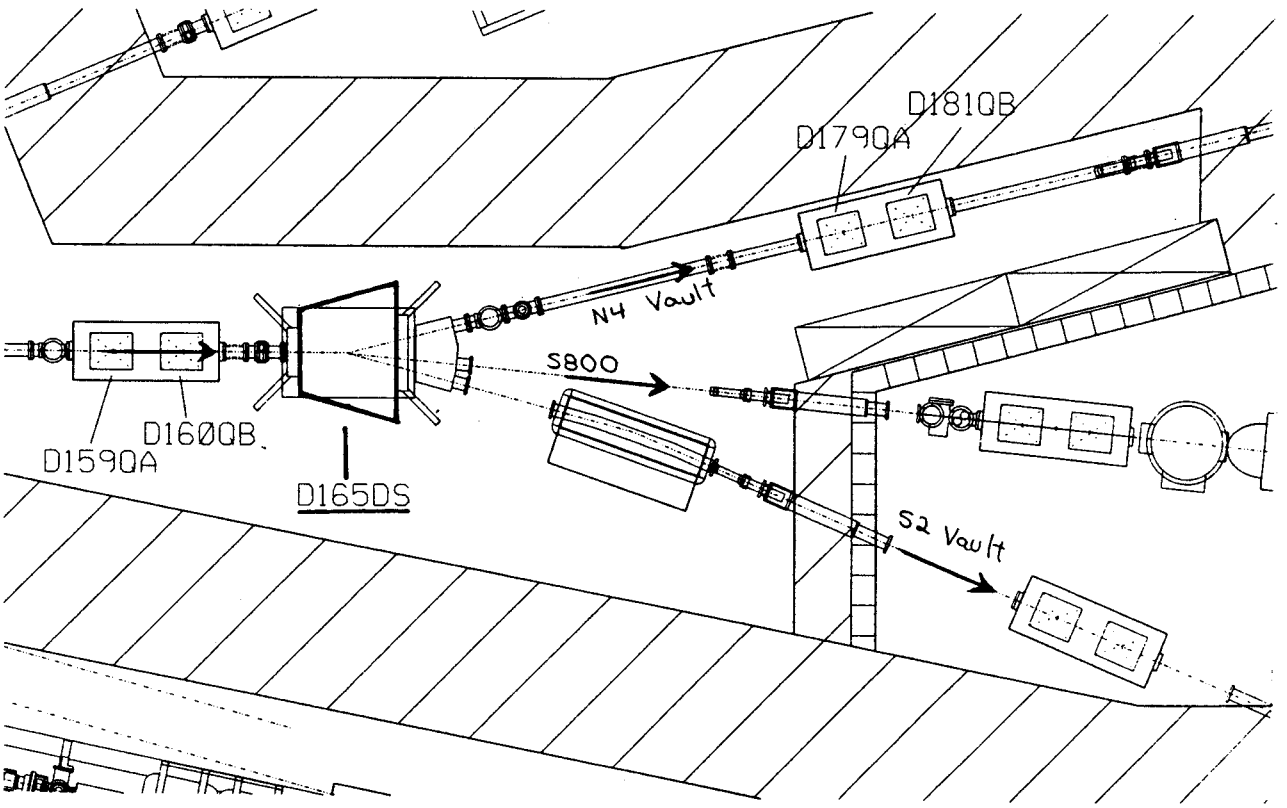

Figure 1: Location of dipole D165 showing the N4, S2, and S800 beamlines into which it will bend beams.

Quadrupole Construction

A spare quadrupole triplet cryostat for the A1200 line is presently under construction for reasons as mentioned for the spare dipole core assembly. One of the triplets also is irradiated significantly because of its location just downstream from the production target making it more subject to coil damage. The quadrupole doublet at the beginning of the S800 beamline and a new doublet to be added to the A1200 line just in front of the production target are also under construction. The triplet and one doublet have their magnet assemblies complete in their LHe vessels. The other doublet has its magnets assembled and cryostat parts are being ordered. The quadrupole doublet in the N2 experimental area (4π Array) was removed and replaced with a new doublet because of

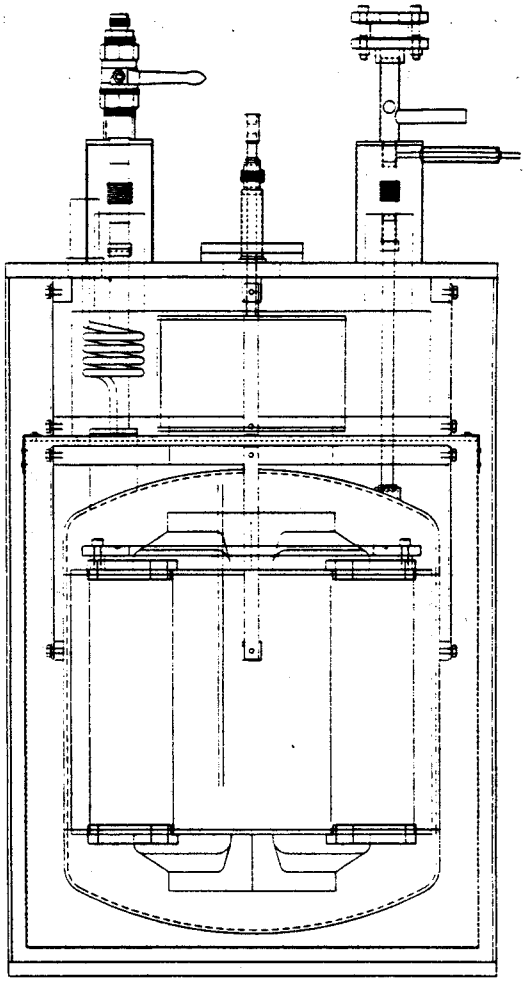

Figure 2: S800 beamline quadrupole test cryostat used for testing the prototype 20.3 cm. aperature quad magnet.

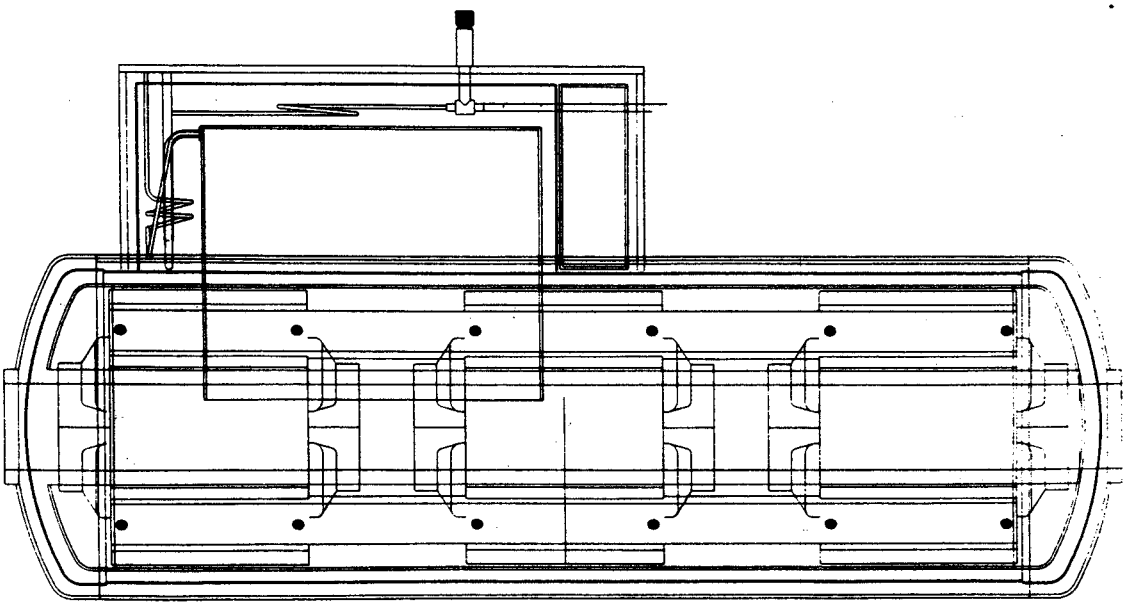

Figure 3: Preliminary design of the S800 quad triplet cryostat. Two of the 5 cryostats will be installed at a 45° angle. The other 3 cryostats will be installed horizontally.

shorted turns in one of the coils of one magnet. This made beam tuning difficult as the current would vary between the coils causing some steering whenever ramping voltage was applied. The defective coil was known at installation but only became a problem in recent experimental setups where stray particles during tuning could damage detector arrays. The doublet which was removed has now had its bad coil replaced, been reassembled, and is installed on the new S2 beamline along with another newly constructed doublet. A total of 36 superconducting beamline magnet cryostats are now installed, 34 presently in operation, containing 55 quadrupoles and 9 dipoles.

A test cryostat for the new larger quads for the S800 beamline is presently being built and is shown in Figure 2. Quadrupole steel machining is progressing well with poletips completed for 7 of the 15 magnet assemblies and the remaining poletips 50% complete. One yoke is fully machined making a complete steel assembly for testing. The remaining yokes have their O.D., I.D., and faces turned and now only require holes for bolting and doweling the poletips and flats milled for alignment. Three of the 4 coils needed for testing have now been wound. The winding forms and process has developed to the state where regular coil winding can occur as soon as successful testing is complete and conductor is ordered and in house. Testing should be completed in May, 1993, with coil winding beginning in July, 1993. Cryostat design is approaching the stage where detailing can begin. Some parts of the design are completed to the point where parts fabrication can occur. The LHe container will be a cylindrical pressure vessel with standard heads and a "hat" attached for LHe and LN2 reservoirs. A view of the cryostat at a 45 deg. orientation leading down to the S800 spectrograph is shown in Figure 3. The cylinders and heads for the LHe containers are in house. Completion of all 5 quad triplet cryostats is scheduled for completion in Sept., 1994.

References

1. J.A. Nolen et al., "A Proposal for Construction of the S800 Spectrograph", Technical Report MSUCL-694, National Superconducting Cyclotron Lab, July, 1989.
2. A.F. Zeller et al., MSU Annual Report (1991), p. 206.
3. C. Magsig et al., MSU Annual Report (1991), p. 209.
4. J. DeKamp et al., MSU Annual Report (1990), p. 203.

THE S2 VAULT: A NEW EXPERIMENTAL STATION

D. P. Sanderson

The laboratory expects to make the S2 vault operational as a new experimental station in the near future. The vault is displayed in Figure 1. It consists of the tail of the Reaction Product Mass Separator (RPMS) and a new beamline dedicated to the University of Rochester Superball neutron detector. The vault is already in use for RPMS experiments, so this article will concentrate on the changes necessary for the Superball beam line.

After being focused through the transfer hall, the beam is bent southward at superconducting dipole D165. The beam bends an additional 8 degrees after D165 and is focused by two superconducting quadrupole doublets into the center of the Superball. At the exit is a shorter version of the faraday cup in use in the N4 vault. Due to the shallow angle and low beam current, steel shielding is only needed on one side of the Faraday cup. Pumping for the line and detector is provided by three turbo pumps: one at D165, one immediately in front of the Superball, and one plumbed directly to the vacuum chamber of the Superball.

In terms of radiation safety, the S2 is common with the S3 vault. The short wall next to the superball protects the detector from neutron activation and residual activity due to the production target installed in the S800 beam line. Since the detector holds over 17,000 liters of liquid scintillator, both passive and active safety systems, which provide protection in case of accidental spills, will be in place. Once the superball is installed, a thin steel wall will be erected on the east side to allow the darkening of the vault. Appropriate cabling for both the main detector and the installation of the NSCL miniball detector array inside will be available.

The completion of this vault will naturally depend on the construction schedule of the superball. It is hoped that the first experiments will take place in late 1993.

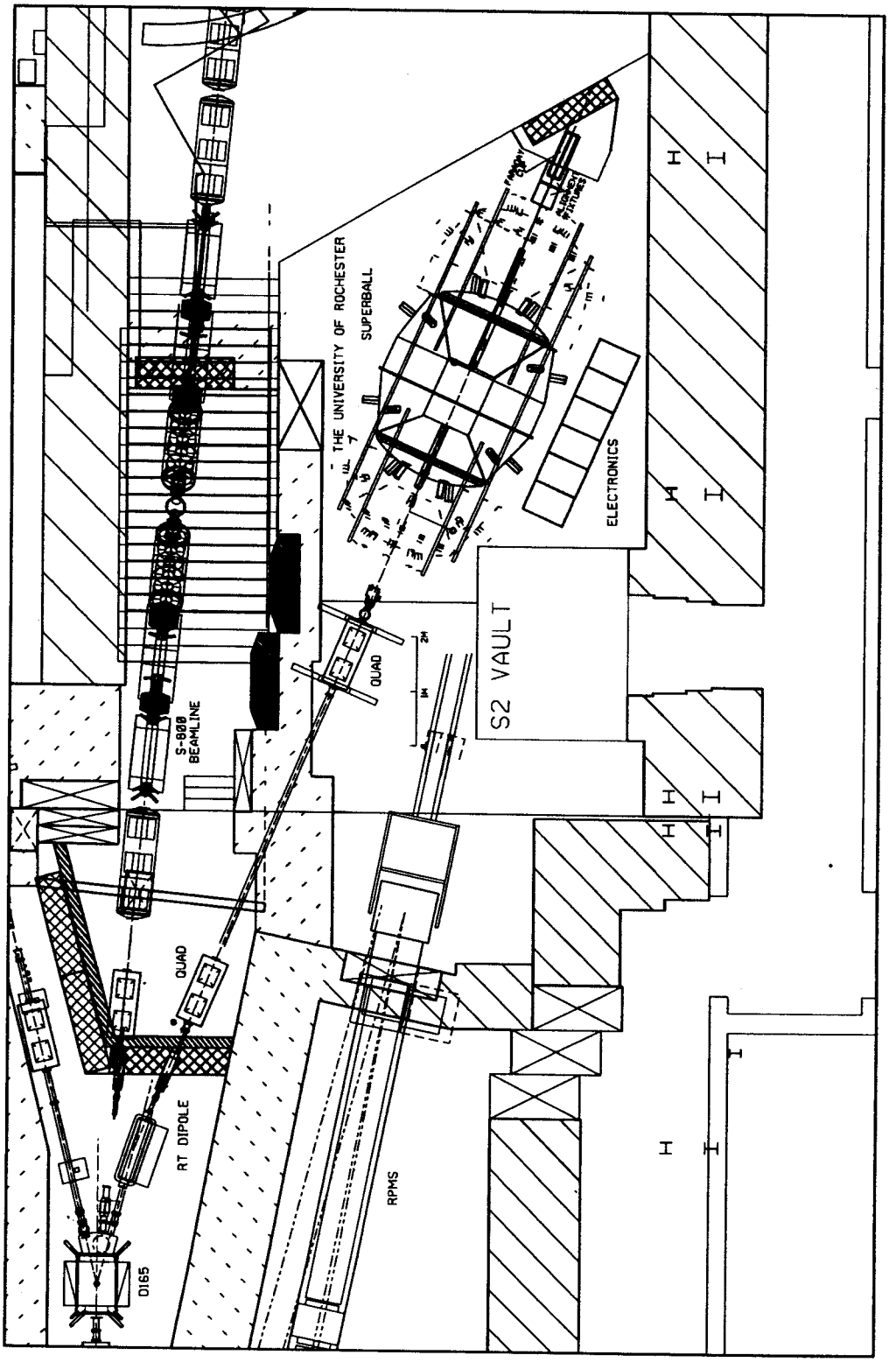
THE UNIVERSITY OF ROCHESTER
SUPERBALL
ELECTRONICS
S2 VAULT
QUAD
S-800
BEAMLINE
QUAD
RT DIPOLE
D165
RPMS

Figure 1.

CRYOGENIC SYSTEM STATUS

H. Laumer

The consumption rate of the cryogens, liquid nitrogen and liquid helium, continues to increase. The liquid nitrogen is delivered by tanker truck every second day on the average. The liquid helium needs are met by operating continuously a main refrigerator of 600 watt nominal capacity and as needed a CTI-1400 for special applications. During this operating period the U-M 7 tesla solenoid, a few beamline magnet tests, the lead test chamber, and the solid hydrogen target development depended on liquid from the CTI-1400. A transfer line station has been added to the beamline liquid transfer system in vault N4 so that the U-M 7 tesla solenoid can be filled in a batch fill mode from the main liquefier. This will be necessary when the CTI-1400 is used to test and operate the S-800 spectrograph.

It is very likely that the additional load of the S-800 spectrograph and the beamline magnets leading to it will strain our liquid helium supply system as presently configured. To determine what our total requirements will be, it is useful to know our present refrigeration load. The heat load of a device, including the transferline system serving it, such as the K-1200 cyclotron coil or the K-1200 cryopanels, could be measured by recirculating liquid helium from a dewar and measuring the rate of liquid consumption. The practically continuous operation of the lab facilities makes this technique impractical. As a result the load contributed by devices is measured indirectly. The operating speed of liquefier expanders is held constant, and the liquid production rate is determined from the liquid level rise in the liquid distributing dewar as the device is cut off from liquid supply or is put on line. A heater is installed in the dewar and can be used to try to match the load of a device cut off from liquid supply. Time and operation requirement constraints limit this technique. The simpler mode of running the heater at a known power and then operating with the heater off and measuring the increase in rate of level rise is more common. Tests of this type have yielded a conversion constant of 2.6 watt/hr of registered liquid level rise. Maintaining constant engine speeds has been possible only since 10/93, when computer control of all expanders was implemented. Table 1 includes a summary of heat loads of individual devices measured by this technique. The values are based on a number of observations, and the variance of the observations is noted. Since the distribution system is multi-branched, it is somewhat arbitrary how the individual measurements are made; they were, however, carried out consistently. For example, when the Superconducting ECR measurements were made, the K-1200 coil was always in operation. In the case of the K-1200 coil and

the K-500 coil it is possible to obtain a static load by measuring the "liquid boil-off rate" right after liquid supply is cut. This is based on the known volume and geometry of the coil cryostats and the liquid level sensors mounted in them. The combined heat load of the beamline magnets was determined by the same technique. The actual liquid requirements to keep these devices filled can be independently determined by monitoring the dewar level during the filling cycles. These values are also noted in Table 1.

The information obtained indicates that liquid transfer losses are a significant part of the operating load. It is also evident that no single branch of the distribution network contributes a large fraction of the load. It is thus not possible to single out one piece of equipment and claim rebuilding it would be cost effective. There are some retrofits that may cut transfer line losses -- for example, using vapor cooling at bayonets and safety pop off lines -- but installing them in a global manner would require a significant down time for the liquid helium supply system.

The capacity of the liquefier is not a constant quantity. The rate of liquid production depends critically on the efficiency of the expansion engines. As the critical engine parts wear during operation, especially piston clearances and valve seats, the efficiency declines and the liquid production rate drops. The other significant process which slowly degrades performance is due to oil carryover from the compressors. The partial plugging of heat exchanger tubes leads to pressure losses which also affect production rates. As the system requirements increase, the tolerance to these effects declines and more frequent maintenance is required. We are in the process of establishing the maintenance schedules which promise maximum performance of in-house equipment. If we allow for a 15% decline from peak production during a maintenance cycle and set aside 15% of capacity to handle peak loads during operation (cool-down of equipment, etc.) then the total load as estimated in Table 1 will require a plant of 740 watt capacity. The present re-liquefaction resources are close to 680 watt.

The medium-pressure (<250psig) gas storage capacity is presently smaller than the average liquid helium inventory. We were fortunate to be able to acquire the high-pressure(<2450 psig) gas storage tubes from the Tantem Lab at the University of Pittsburgh this year, doubling our gas storage capacity. Even though we do not have the means to return gas to high pressure, the fact that the medium pressure gas storage can be maintained at a relatively low pressure most of the time increases the effective storage capacity.

Table 1: Equivalent refrigeration load at 4.5K

DEVICE	EFFECTIVE LOAD ON RE-LIQUEFIER (WATT)	STATIC LOAD (BOIL OFF TEST) (WATT)
K-1200 coil	144 ± 31----------	27
K-1200 cryopanels	45 ± 20	
K-500 coil	62 ± 13----------	22.5
K-500 cryopanels	40 ± 26	
SCECR	48 ± 27	
Beamline magnets	65 ± 7 ----------	10
U-M 7 T solenoid	65 ± 7	
S-800	50 (estimate)	
S-800 beamline	50 (estimate)	
Total	569 ± 55	

STATUS OF THE A1200

J.S. Winfield, D.J. Morrissey, B.M. Sherrill, and J.A. Winger

The A1200 fragment separator continues to be heavily used by experimenters at NSCL. A report on the initial operating experience is given in Ref. 1. Experiments making use of the device fall into three broad classes: those producing and analyzing fragments within the A1200, those producing secondary beams in the A1200 which are then transported to external target locations, and those which use the A1200 as a zero-degree energy-loss spectrometer.

Various small improvements have been made to the A1200 over the last year which make the A1200 a more user-friendly device.

- The precision of control for the magnetic elements has been increased by changing the DACs for the quadrupoles from 12-bit to 16-bit resolution.
- A Hall probe has been installed in the switching magnet immediately after the A1200 focal plane. In addition, a set of moveable horizontal slits for each of the three beam lines in the Transfer Hall has been installed immediately after the swithing magnet, These improvements facilitate the tuning of radioactive beams to target locations in other vaults.
- Indium seals on the detector boxes at the focal plane and the second dispersive image have been replaced by O-rings, since these boxes are opened on a regular basis and the ultimate vacuum is generally limited by gas-filled detectors and not by O-rings.
- Monitor detectors similar to the ones previously installed in the medium acceptance target position have been installed in the high acceptance target location.
- A user's manual has been written to serve as a reference guide for operation of the device.

The optics of the A-1200 for the various modes of operation are continuously being refined based on experience. One result is that the standard mode of operation with the target in the 'medium acceptance' location uses an acceptance of 30 by 34 mr rather than the original design of 20 by 40 mr. Also, several spectrometer modes have been developed during the past year, with the target location being at either the medium acceptance position, the high acceptance position, or the second dispersive image. For the latter case, an array of silicon PIN diode detectors have been used in coincidence with the A1200 focal plane counters, to look at the particle decay of excited resonance states.

A major re-arrangement of the target area is planned for later this calendar year. This will involve the insertion of an additional quadrupole doublet before the present 'high acceptance' target location giving larger a solid angle. A single larger target box will replace the present target chambers.

References

1. B.M. Sherrill, D.J. Morrissey, J.A. Nolen Jr., N.A. Orr, and J.A. Winger; Nucl. Instrum. Meth. **B70**, 298 (1992).

AN INTERNAL PROBE FOR MEASURING BEAM TIME SPECTRA IN THE K1200

J. Bailey, D. Au, D. Blue, J. Kuchar, F. Marti, J. Ottarson, and J. Yurkon.

A timing probe, designed to study the distribution of the beam in time, has been installed in the K1200 cyclotron. A specially cut and mounted Si detector is inserted directly into the internal beam, providing a fast electronic signal when struck by a beam particle. Referencing this start signal to a stop signal derived from the accelerating RF waveform, a beam time spectrum can be accumulated at any point along the probes path. For use only with extreme low intensities, 1000–3000 counts/sec, the probe can be used in tuning the phase slits, measuring beam phase, studying beam dynamics, and observing relative intensities of low current beams. This probe is not capable of measuring space charge effects, but this is not yet a problem with K1200 beam intensities.

Using the standard K1200 probe design[1], the Timing probe can be installed in either the A2 or A5 probe drives. Interchangeable with the TV and Current probes, the operator can simultaneously mount two probes, permitting rapid alternation between different beam observation methods. Installing a probe is a half-hour job.

The beam spot size on the detector is the lesser of the radial beam width of a given turn, and the radial gain per turn. The latter is also the greatest distance from the leading edge at which a particle can strike the detector for a centered beam. This distance, 900–600 microns in the last 8 in. of the K1200, necessitates a special detector design to reduce dead area as well as edge effects. After examining the responses of specially cut detectors produced by Senter for Industriforskning[2,3], one cut outside the inner guard ring seemed best suited for use in the cyclotron.

The detector cut inside the inner guard ring, which had the smallest dead area, estimated at 10–100 microns by SI, had high leakage currents and actually collected more charge than the uncut detector 3% of the time, when tested with an alpha source. (Equivalent to an area equal to the width of the cut edge times the thickness of the detector.) The detector cut outside the inner guard ring amplifies the signal .3% of the time, and has a dead area estimated to be 150–190 microns wide. Both detectors though were tested successfully inside the cyclotron, with the greater edge effects of the first not adversely effecting the timing spectra. This is with the detector slightly over depleted, biased at 47 V with depletion at 35 V. The guard ring was biased at 80 V.

An LBL time pick-off amplifier, between the detector and its charge sensitive pre-amplifier, picks the fast response of the detector. This signal, with a 5 ns rise time is later amplified and input to a constant fraction discriminator. (Fraction 1/5, delay 3.3ns.) The output is latched with a computer not busy signal, and input to the start of a CAMAC time to digital converter. A pick-up loop inside dee C provides the RF voltage waveform to a leading edge discriminator, whose output is used as the stop signal in the TDC. The results are histogrammed and displayed using a program written for color X-Windows on a VAX. The energy deposited in the detector can be histogrammed simultaneously using a shaping amplifier and a CAMAC ADC in the same program.

Detector resolution has been seen to be as good as 150 ps FWHM (fig. 1, peak at -2 ns.) The detector will not measure the time distribution of a single turn, unless there are separated turns. Instead it samples pieces of succeeding turns, measuring particles with the largest energy gain first, losing some in the dead area, repeating with the remaining particles in each subsequent turn, until the bunch is exhausted. This is true even in the operating condition of a particle per 10000 bunches. The dead area is sufficiently small, that in the normal operating regime, particles collected in adjacent turns overlap in phase. The graph in figure 1. is an extreme condition. ϕ is large and negative, and will shortly approach the point where energy gain per turn is insufficient to clear the detector dead area. Here the $r-\phi$ correlation due to the $\cos(\phi)$ dependance of energy gain combines

with the phase slip per turn to remove this overlap. These two effects are still present in the operating regime, working to slightly compress or expand part or all of the measured spectra, with respect to the spectra of a single bunch at a given turn. Other effects can broaden a spectrum. These include the range of incidence angles of particles (calculated to always be negligible.) Also, particles that leave the active region before traversing the full depth (up to 20% can appear 100 ps early, if the threshold is not low enough, these are lost.) Finally, a broadening can result from RF pickup (for every 6% of RF pickup voltage with respect to signal voltage at 32 in., the spectra will be broadened 30 ps/10° RF width at 32 in. and 12 ps/10° RF width at greater radii.)

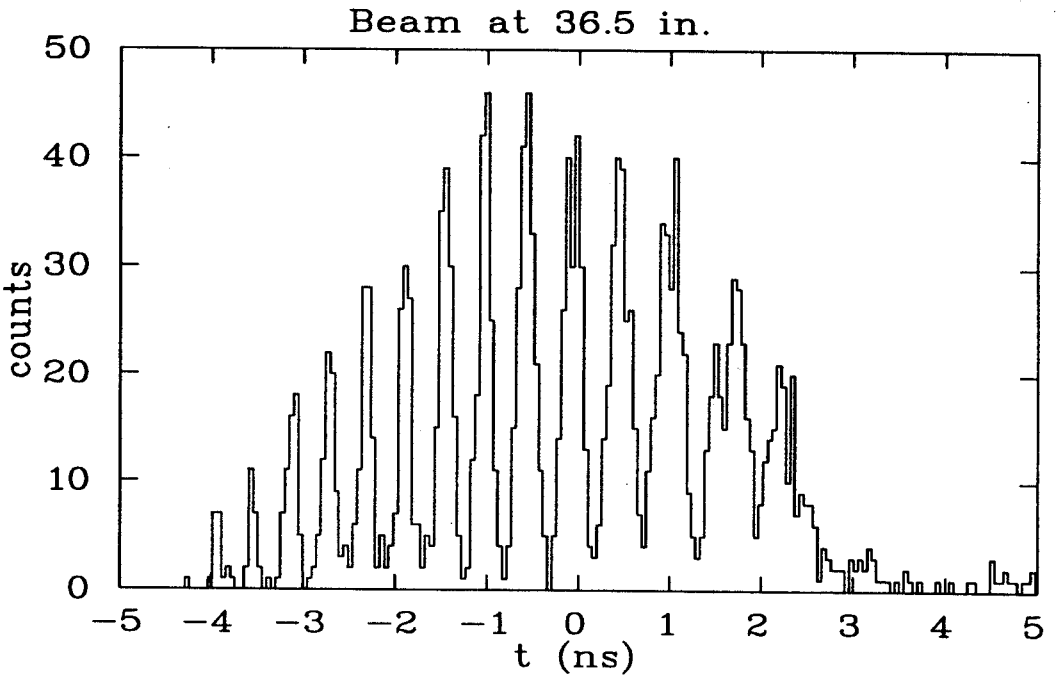

Figure 1: This beam will shortly slip off resonance. The distinct peaks are from separate turns. Note FWHM as low as 150 ps. 28 Si 8+ and 35 Cl 10+ are extracted at 70 MeV/A (not shown.)

There are also effects on the relative position of spectra at different radii. The chief of these is from the linear path of the probe, the reference line is the dee center which is a spiral in most of the K1200. This time of travel can be calculated with orbits run in design fields at appropriate energies. SPRGAPZ was used to run orbits in fields created by MONSTER[4], the program used for current and extraction settings. The RF pickup can also create a drift of 300 ps/6% of signal voltage. Finally, the actual variation in signal strength with radius is ignorable unless the Bragg peak can lie in the detector. Calculations have shown a 80 ps drift for a 25 MeV Ar beam exiting the detector at maximum energy, and a 64 ps drift for a 30 MeV Xe beam exiting at 36 in.

References

1. Marti, F., et al., in **Proc. 12th Int. Conf. on Cyclotrons and their Applications** (World Scientific, Sin 1989) p. 268
2. J. Yurkon et al., MSU Annual Report (1991) pp. 170–171.
3. Evensen, L. Private communication, Senter for Industriforskning, Norway, 1992.
4. Harwood, L., MSU Annual Report (1986) pp. 147–148.

S800 PROGRESS REPORT

A.Zeller, B.Sherrill, S.Bricker, L.Morris, R.Swanson, R.Fontus, M.Berz, H.Blosser, J.DeKamp, R.Degenhardt, P.Johnson, C.Magsig, H.Laumer, T.Jones, H.Hilbert, J.Nolen, D.Pendell, D.Sanderson and B.Zhang

Several important milestones have been met in the construction of the S800. The biggest was the completion of the coil winding for the first spectrometer dipole magnet. The coils have been sealed in the bobbin and the bobbin is leak tight. The nitrogen shield is being assembled around the bobbin, with the intention of using it to cool the bobbin to liquid nitrogen temperature as a cold shock to test the weld integrity (there are about 80 meters of weld per cryostat). After the final leak check, the installation of the bobbin in the cryostat will begin. The trim coils have been wound, and several have been test fitted to the pole tip assembly. They can not be attached until holes have been added to the side plates to allow attachment of Faraday Cup bars. The projected date for putting current into the dipole is September 1993.

Because of the vertical assembly sequence, holes through the return yokes into the pole tip assembly have to be made to hold the pole tip/cryostat assembly to the top and bottom yokes. This requires considerable movement of the large pieces of the yoke and flipping of the pole tip assembly. Additionally, the inner return ring has to have a key way cut into the hole for the compressional support link to allow assembly. The carriage and the track have been designed and all parts have been ordered or are in house.

To leave more room in the target area, the beam height has been raised by twelve inches. This allows more access for large detector arrays (eg, the Miniball), but compresses the beamline element spacing. This small inconvenience is more than made up in the enhanced flexibility in the target chamber area. To allow further access the last beamline quadrupole triplet can be removed, and for some types of experiments, the Q1-Q2 cryostat can also be removed. Removal of Q1 and Q2 is also required to service the slits between Q2 and the first dipole. A side view of the complete spectrograph and associated is shown in figure 1.

The forces on the bobbin and the support links are such that excitation of the dipoles to 600 A is possible. This gives a central field of 1.7 T, but with a significantly reduced region of "acceptable field quality". Although some of the resolution and solid angle/momentum acceptance will be lost, more rigid beams can be accommodated.

The mapping apparatus which uses a stainless steel "comb" with an optical sensor has been tested in a magnetic field. The field does not effect the sensor, which would have been the case if we had used the system built to map the K1200 and the K250 cyclotrons. Testing of the system with five search coils is in progress.

The S800 should be ready to accept beam in December of 1994. After testing and optimizations, the first experiments should begin in early 1995.

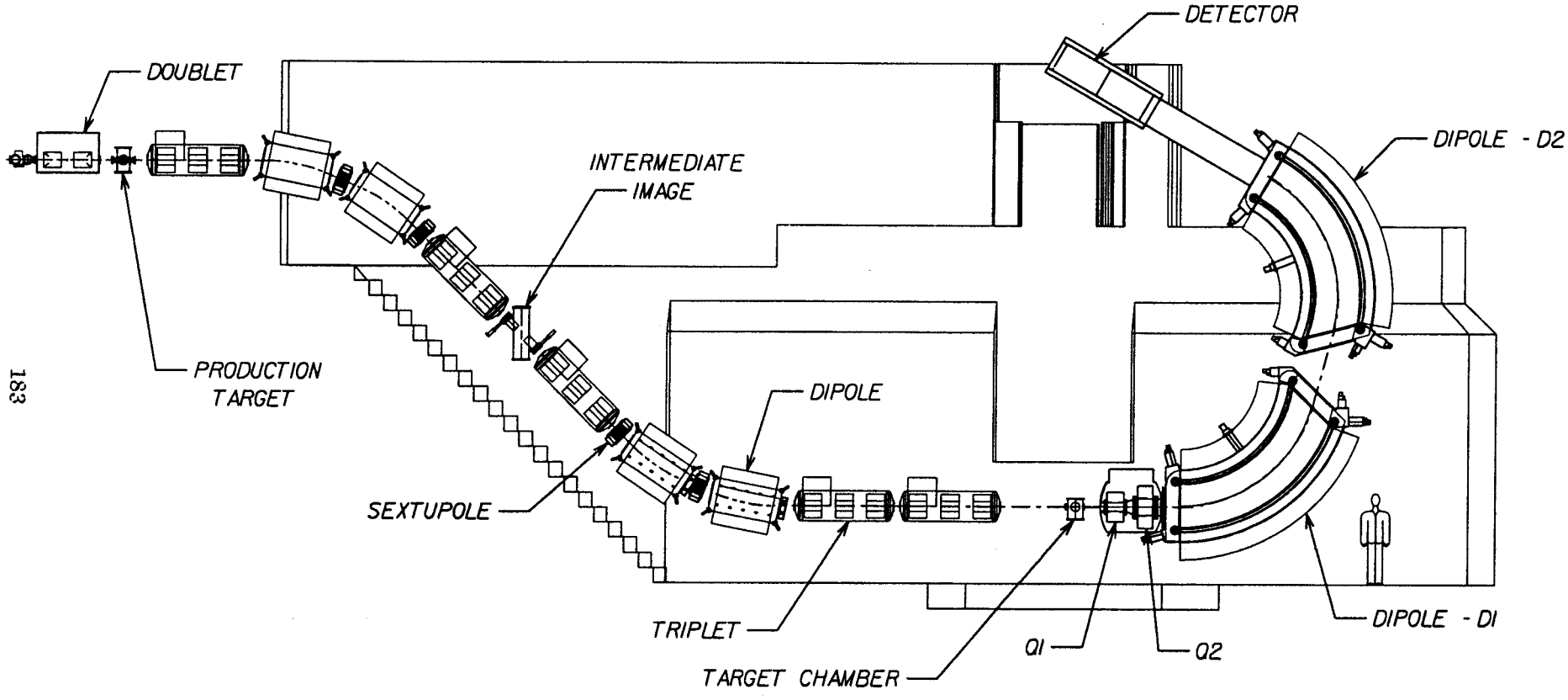
DETECTOR
DOUBLET
DIPOLE - D2
INTERMEDIATE
IMAGE
PRODUCTION
TARGET
DIPOLE
SEXTUPOLE
TRIPLET
TARGET CHAMBER
Q1
Q2
DIPOLE - D1

S800 ELECTRONIC CONTRUCTION STATUS

T.R. Jones

Introduction

The Electronic Shop is currently involved with the manufacturing of the basic devices needed for the S800. These include the 20v/20a and 10v/100a power supplies, two types of servo controllers, vacuum gauge controllers, and two types of cryomonitors. The S800 project will require approximately 4.25 man-years of labor from the electronic shop to complete. To enable us to build the needed electronics with the labor available, we will build each type of module using a production line. This will help us maximize the available labor and minimize the costs for outside assembly services.

As construction continues on the spectrograph, all of these parts will have to be installed and tested. The installation process includes work from the electricians, plumbers, and mechanical group which must be coordinated with the electronic shop. Thus, to better utilize them, the power supplies, servos, etc will have to be built in a specific order. To facilitate this, the 20v/20a and 10v/100a power supplies and the standard type of cryomonitors are being built first due to the need for these instruments for the testing of various magnets and running of the S2 vault. The other units will be built according to the time they will be needed.

20v/20a Beam Line Power Supply

The 20v/20a power supplies we have been using in the previous sections of the beam line will again be used for the new additions for the S2 and S800. We will need four for the S800, four for the S2 and two for a modification of the A1200.

The new power supplies will have two improvements over previous versions. These changes are a new shunt output interface printed circuit board for better tracking and a safety switch for the output terminals which renders safe the coil leads upon removal from the power supply.

Each 20v/20a will require approximately 1.7 man-months to assembly and test. The work was started in mid February of this year and is expected to be completed by mid October of 1993. As of writing time, the shop has 25% of the work completed for these power supplies.

10v/100a Beam Line Power Supply

We currently require 21 10v/100a power supplies to drive the five triplet magnets and six dipole magnets

planned for the S800 beam line.

Each 10v/100a requires approximately 1.1 man-months of work to build. Due to that and the need for these supplies in the summer of 1994, work began in late April of 1993. They were partially funded so that we could buy the components necessary to maximize the usage of available labor in the electronic shop and minimize the work required from the machine shop. The items which require a large amount of machine shop time will be made at a later date when the shop's workload is not as heavy with more critical work.

These power supplies will require more resolution from its computer section than previous 10v/100a's. To meet that requirement, a new microcontroller circuit is being developed to replace the 68701 board now in use. The new controller will utilize the 68332 processor which allows us to have 16 bit analog resolution.

In previous beam line expansions, the 10v/100a power supplies were placed directly under the magnet they drove. However, due to space and accessibility considerations, all 10v/100a's will be placed together in a central rack cluster.

Cryomonitors

The S800 and S2 beam lines require two types of cryomonitors due to the different styles of magnet cryostats used. The first type is a standard unit similar to what is in use now and which is configured for either a quadrupole or dipole magnet by changing a few components on the controller printed circuit board. The other type is new and will be used on the triplet magnets on the S800 beam line. This new type will have only one lead drop voltage read out and none of the helium/cryogenic readings. This will be accomplished by using a standard unit and modifying it by only entering the components needed for the single lead drop section. It will be used in conjunction with a standard unit. By modifying an existing design we save both design time and the money required to make a new version.

The S800 requires twelve quadrupole/dipole units and five single lead voltage units. The S2 requires two quadrupole units and the modification to the A1200 requires one new quadrupole cryomonitor.

Work is progressing on the first group of 15 quadrupole/dipole cryomonitors. Since March, when the work began, approximately 60% of the work has been completed and we expect to have all 15 assembled by mid July. Work for the single lead version will start in September.

Vacuum Gauge Controllers

The beam line for the S800 has been divided into seven sections. Each section will require a vacuum gauge controller. We will be using the same model as is used elsewhere in the lab.

They will be made starting in February of 1994. The seven units will be ready for installation in April of 1994.

Servos

The S800 will require two types of motion control drives to run the various servos used in the spectrograph. They include 15 Bang Bang Servos of the type used throughout the lab and nine other drives of a type not yet specified but will most likely DC Motor Servos.

Construction on the Bang Bang Servos will begin in December of 1993, and, they will be ready for installation in April of 1994. Each servo requires .33 man-months to assemble. The DC Motor Servos will be manufactured in parallel with the Bang Bang Servos.

Beam Current Meters

The S800 will require four BCM's. The shop will not have to build any of these units due to the quantity we have in stock.

Installation

The size and shape of the spectrograph pit has presented some challenges as to where the electronics, Modicon, ac power, and VME systems can be installed. As was stated above, we would like to place the power supplies as close to the magnet they drive as possible. However, due to the approach to the pit, this is not possible. So, we must place the 21 10v/100a supplies and the supplies which will drive the sexapole magnets (which will be purchased later) in a relay rack cluster located near the north wall and under the main walkway.

The computer control rack which will house the VME and Modicon interfaces and other electronics will be located under the stairs. In order to allow for the possible movement of large items into the pit by way of the elevator, this equipment rack will be on rollers and have enough slack in the cables to allow it to be temporarily moved out of the way.

The main ac power leads us to another challenge. First we must bring in various voltages to power a wide variety of equipment. Second, the current levels which are required are significant. Thus, not only will we need several electrical boxes to accommodate the various types of power but these boxes must be large enough to allow for the number of circuits required. The solution we are going to use for the first problem is to place the main feed box in the transformer vault and run just the main lines we need to the secondary box thus eliminating one panel in the pit. The answer to the second problem is to place the secondary 208vac box near the north door of the pit straddling the door mechanism. This area is unusable for other applications and it will work well for our needs.

The Modicon drop which will control the spectrograph will require four boxes for I/O modules, interface

modules, and the phone blocks for the various devices. To meet the Modicon requirements, we are going to place the main I/O box outside the S800 vault on either the north wall near the door or southwest corner going into the high bay. The exact location will be decided upon in the future. Placing it at either of these locations has the advantage of not cluttering the pit and enabling work to be performed on the Modicon without breaking radiation safety. The other three block boxes will contain phone terminals and be located as close to the devices as possible. One will be on the north wall near the stairs for the beam line, one will be on the north wall below and east of the door and the last one will be on the carriage.

Conclusion

The electronics portion of the S800 will require a significant amount of labor and money to build. However, with the resources available, the required modules can be built and installed when needed if the work is properly planned. At the current rate, the electronics should be completed in June of 1994. This date assumes there will be adequate funding and manpower. Refer to figure 1 for the status of the major modules as of the time of writing.

3D MAGNETIC FIELD CALCULATION OF THE S800 SPECTROGRAPH

F. Marti and A. Zeller.

Introduction

The original design of the S800 spectrograph [1] was based mostly on 2D magnetic field calculations performed with POISSON [2]. We report here the more recent calculations done with the 3D codes ANSYS [3] and TOSCA [4].

One of the topics of interest to be determined with the 3D calculations was the size of the magnetic interaction between the dipoles themselves and between the dipoles and the two quadrupoles Q1 and Q2 (placed just after the target and in front of the dipole D1). The Q2 quadrupole presents an unusual configuration with a bore diameter of 44 cm and a length of 30 cm.

Interaction between the dipoles

The main question to answer is the effect of the fringe field of one of the dipoles on the field of the other dipole. This point is important because of the difficulties associated with mapping both dipoles simultaneously. It is much simpler to measure the magnetic field for each dipole independently. Figure 1 shows the grid utilized to calculate the dipole fields with TOSCA. Two calculations were performed. In one of them only one dipole exists while in the second one both dipoles are present and interacting. A polar grid was obtained for each map and then subtracted point by point. This exercise was repeated for two different excitations corresponding to central fields of 1.65 and 1.41 Tesla. The subtracted fields showed a decrease in the central field in the beam region of 110 and 50 gauss respectively. A third calculation was performed at low excitation to verify that the difference goes to zero for low fringe field situations. The lines of constant difference are approximately lines of constant radius, with the minimum effect near the center of the pole tip and maximum near the edge. This could be interpreted as being produced by the saturation of the iron in the pole tip that follows the same behavior. The value of the interaction was checked also with ANSYS, giving similar values.

Interaction between the dipole and Q2

A different TOSCA grid was setup where one of the dipoles and the quadrupole next to it were included. The purpose was to calculate the departure from field superposition due to the mutual fringe fields.

Three different excitations were used. The results are summarized in the following table where the error row corresponds to the peak difference in the field perpendicular to the dispersion plane in the beam region inside the quadrupole. This value indicate the departure from field superposition.

Dipole B (T)	1.74	1.46	0.63
Q2 Gradient (T/m)	7.3	7.3	3.2
Error (gauss)	200	100	5

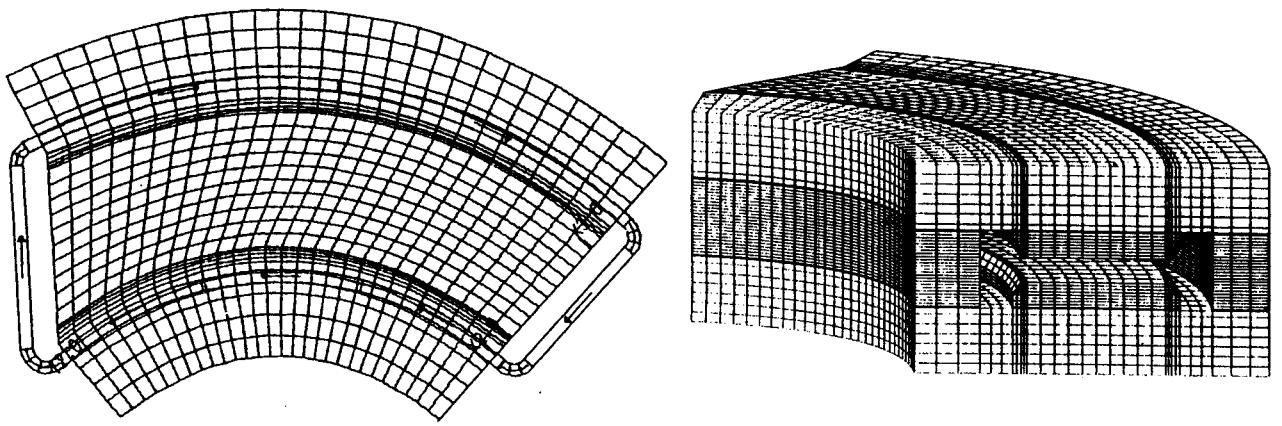

Figure 1: TOSCA mesh utilized to study the interaction between the two dipoles.

Q2 Quadrupole

Two different designs were considered. The first one had the pole pieces tapered at 45 degrees, while the second case had straight edges. Figure 2 shows the mesh utilized in the straight edge case.

The quadrupole consists of a cylindrical yoke with an inner radius of 0.336 m and an outer radius of 0.432 m. The length is 0.3 m. The pole tips inscribe a circle with radius 0.21 m. The design current density is 6821 A/cm^2.

The TOSCA results give a magnetic field in the pole tip region of approximately 23 kG, indicating values in the saturation region. This is confirmed by calculations done at half the current. In this lower excitation case the field in the iron drops to 15 kG and the integral of B_y component (x=0.2 y=0) drops from 12.93 to 7.89 kG.

We have calculated the effective length of the quadrupoles by integrating the transverse component $B_\perp$ along a path parallel to the beam axis for r=0.01, 0.05, 0.10, 0.15 and 0.20 meters. These integrals were calculated for $\theta = 0$ and for $\theta = 45$ (towards the pole tip) between z=0 and z=0.6 m. We must note that the integration path is one half of the total magnet.

Dividing these integrals by the r value in meters gives the following results:

Tapered Edge Quadrupole				
	$\theta = 0$		$\theta = 45$	
r	$\int_0^{0.6} B_\perp dz$	$\int_0^{0.6} B_\perp dz/r$	$\int_0^{0.6} B_\perp dz$	$\int_0^{0.6} B_\perp dz/r$
m	kG-m	kG	kG-m	kG
0.01	0.1267	12.67	0.1241	12.41
0.05	0.6323	12.64	0.6297	12.59
0.10	1.2780	12.78	1.2593	12.59
0.15	1.9156	12.77	1.8970	12.65
0.20	2.5863	12.93	2.5293	12.65

Straight Edge Quadrupole				
	$\theta = 0$		$\theta = 45$	
r	$\int_0^{0.6} B_\perp dz$	$\int_0^{0.6} B_\perp dz/r$	$\int_0^{0.6} B_\perp dz$	$\int_0^{0.6} B_\perp dz/r$
m	kG-m	kG	kG-m	kG
0.01	0.1476	14.76	0.1444	14.44
0.05	0.7369	14.74	0.7348	14.70
0.10	1.4851	14.85	1.4740	14.74
0.15	2.2006	14.67	2.2429	14.95
0.20	2.8875	14.44	3.2299	16.15

The straight edge quad shows a larger variation of the effective length as a function of position.

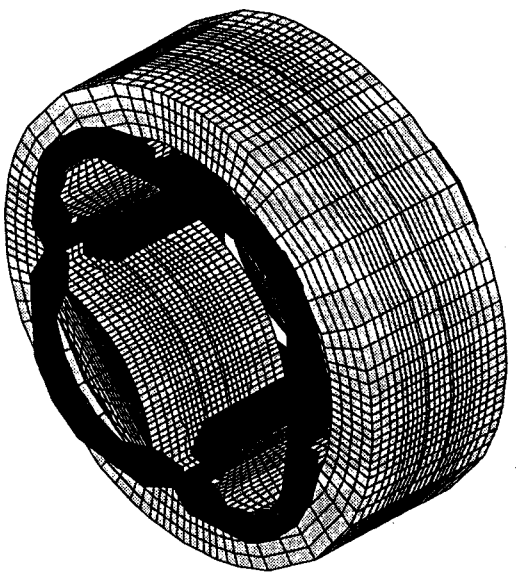

Figure 2: TOSCA mesh utilized to study the Q2 quadrupole.

References

1. MSUCL-694, July 1989.
2. R. Holsinger and K. Halbach, 1981 (unpublished).
3. Swanson Analysis Systems, Inc. Houston, PA 15342, USA.
4. Vector Fields Limited, Oxford, England.

REDESIGN OF THE K-500 CYCLOTRON EXTRACTION SYSTEM TO WORK WITH 250 MEV PROTONS

L.S. Lee, H.G. Blosser, F. Marti, D.A. Johnson, M.M. Gordon, D.O. Jeon and J. Schubert.

The design features of the extraction system for the proposed proton cancer therapy machine are presented here. We had hoped to save money by converting the K500 cyclotron into the K250 proton synchrocyclotron needed for cancer therapy. Unfortunately, the computations presented here indicate that the K500 magnet is unsuitable due to resonance limitation.

The general features of the K-500 magnetic configurations are extensively reported in ref. [1]. The energy and radius at which resonance occurs in the 120^0 main field predicted by the E.O. code [2] are listed in Table 1. It can be inferred that the major resonances lie very close to one another and can not be avoided in the extraction process.

The K-250 machine would utilize the regenerative extraction method [3], [4], [5], [6], [7] which has been used successfully in many synchrocyclotrons [8], [9], [10], [11]. An artificial field bump which simulates the field of the regenerator assembly has been employed in the orbit calculations which were carried out using the Z^4 code [12] and deflz800 program [13].

The amplitude of the average magnetic field and the two leading harmonics of this mathematical regenerator field in the extraction region are given in Figure 1 (left). Note that there is almost no field imperfection in the proximity of the $\nu_r = 1$ resonance.

Figure 1 (middle) shows the radial and vertical focusing frequencies vs. energy corresponding to the fields with and without the mathematical regenerator. The beam is expected to be extracted at an energy of 248 MeV, at which the ν_r value returns to 1 very quickly under the influence of the regenerator field, the radial stable region vanishes rapidly, and particles are peeled off of their orbits.

The extraction element parameters are listed in Table 2.

The pre-extraction central ray orbit is given in Figure 1 (right) .

In addition to the central ray, sixteen rays were calculated which started from 240 MeV, each with different initial displacements on a (r, p_r) and a (z, p_z) eigen-ellipse, respectively. The radial eigen-ellipse was determined by choosing $\Delta r = 0.01''$; for the axial eigen-ellipse $\Delta z = 0.01''$. The radial half width $0.01''$ was chosen because only the beam with initial radial width $\leq 0.05''$ could survive passing through the $\nu_r = 1$ resonance and reach the extraction energy of 248 MeV, as will be shown later. The results of these calculations are summarized in a p_r vs. r phase space diagram presented in Figure 2 (left) which shows the evolution of these pre-extraction orbits. The eigen-ellipse starts to deform dramatically at an energy of 248.08 MeV and the displaced rays were peeled away from the stable region six turns later at an energy of 248.14 MeV owing to the rapid vanishing of the radial stable region.

Table 1: The resonances vs. average radius and energy

resonances	R_{av}(inch)	energy(MeV)
$\nu_z = \frac{1}{2}$	26.03	241.2
$\nu_r = 2\,\nu_z$	26.06	241.6
$\nu_r = 1$	26.20	243.8
$\nu_r + 2\,\nu_z = 3$	27.15	251.8

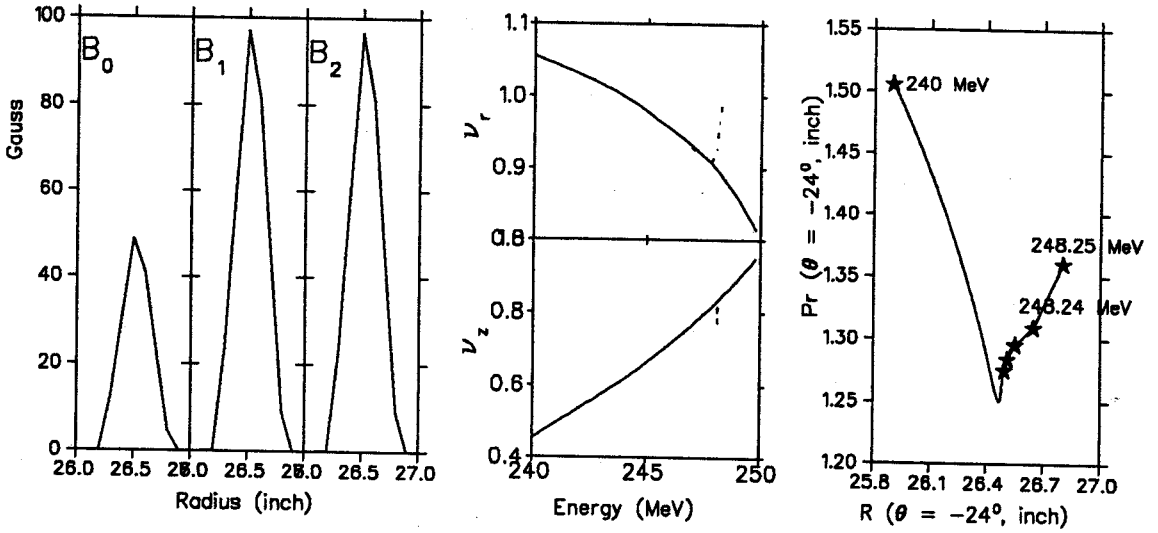

Figure 1: (At left) Plots of the amplitude of the average field and two leading harmonics vs. radius for the mathematical regenerator field. (middle) Plots of ν_r and ν_z vs. energy in fields with (solid curves) and without (broken curves) the field bump added. (right) Radial phase space diagram for the central ray. Plot shows evolution of p_r vs. r at azimuthal angle $\theta = -24^0$ to the entrance of the electrostatic deflector.

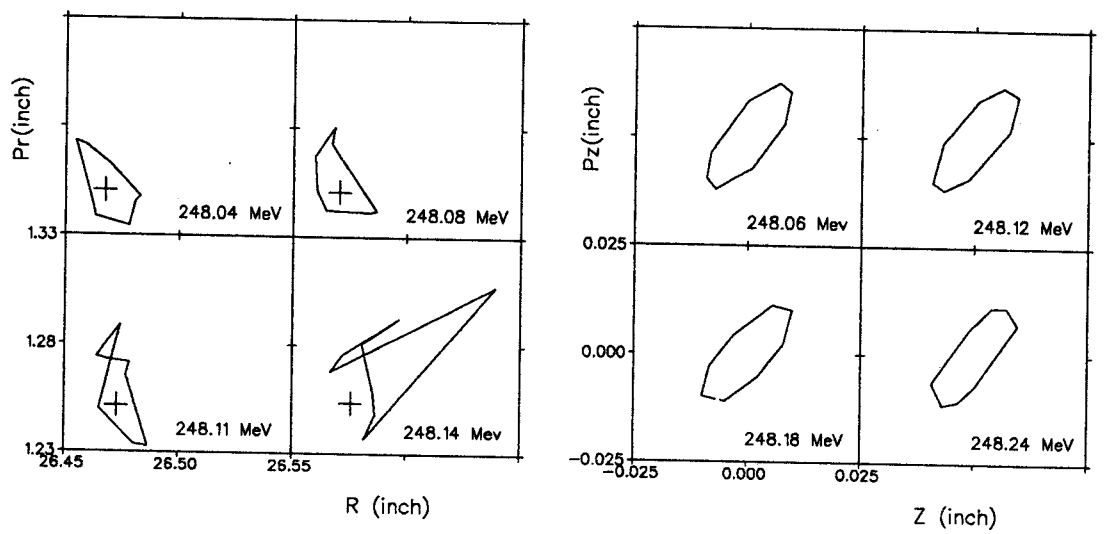

Figure 2: (Left) Pre-extraction radial phase space plots for the representative eigen-ellipse. The central ray position had been indicated by the crosses. (right) Pre-extraction axial phase diagrams for the representative eigen-ellipse.

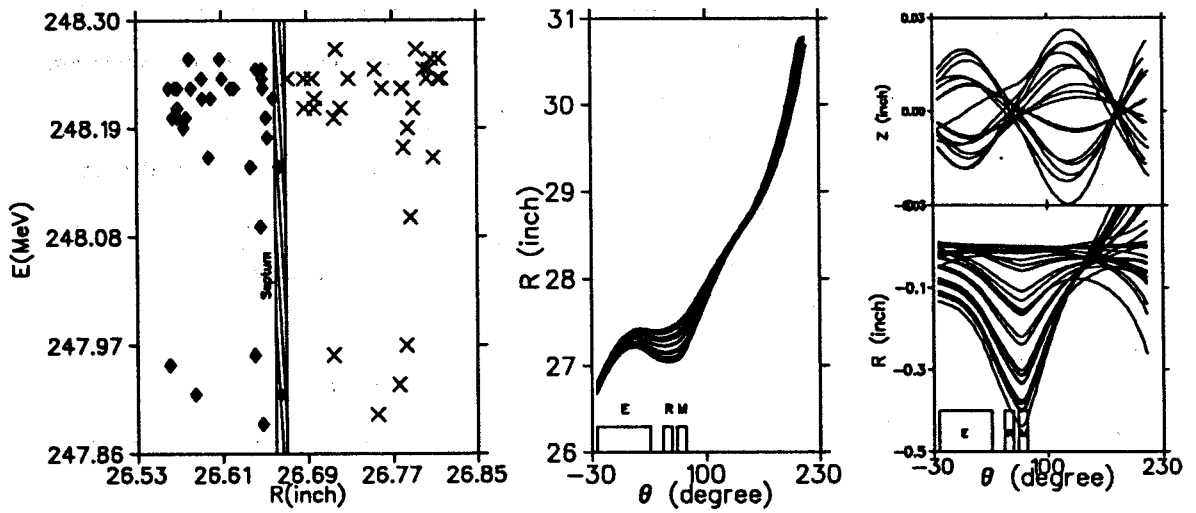

Figure 3: (left) Plot of E vs. R at the entrance of the electrostatic deflector ($\theta = -24^0$) showing the distribution for the central ray and the sixteen displaced orbits. (middle) Extraction trajectories on a Cartesian (θ, R) plot. (right) Radial and axial beam envelopes along the extraction path.

The vertical motion of pre-extraction orbits is summarized in a set of p_z vs. z phase space diagrams presented in Figure 2 (right). The vertical motion is well behaved and confined.

The last two turns of the pre-extraction orbits for the central ray and those sixteen displaced rays which start on the eigen-ellipses of width $0.01''$ are shown in Figure 3 (left). As can be seen from this graph, the clear separation between these two groups of points is only $0.02''$, which obviously could not provide enough clearance for the deflector septum. The electrostatic deflector septum with a thickness of 0.3 mm is chosen and plotted in this graph. The channel entry efficiency turns out to be 64% and the energy spread is 0.11 MeV (about 0.04%) at the entrance of the deflector.

The beams which successfully enter the aperture of the electrostatic deflector, shown in Figure 3 (left), provide the input data for the extraction optics calculations. The results of these calculations are presented in Figure 3 (middle) which shows on a Cartesian (θ, R) plot the extraction trajectories up to a radius of $31''$. From this figure it is evident that an electric field of 100 kV/cm is sufficient. In addition, an aperture as large as 10 mm, calculated according to the empirical VE law, can be used.

The beam envelopes are very well confined along all the extraction path both in the radial and axial directions as can be seen in Figure 3 (right). The axial beam envelopes for four rays which survive the regenerative process and the radial displacement from the central ray are plotted. Any particle with too small or too large

Table 2: Extraction element parameters

	Θ_i (deg)	Θ_f (deg)	E (kV/cm)	ΔB (kg)	$\partial B/\partial x$ (kg/in)
E	-24	36	100		
R	49	61			
M	66	76		1.2	8.8

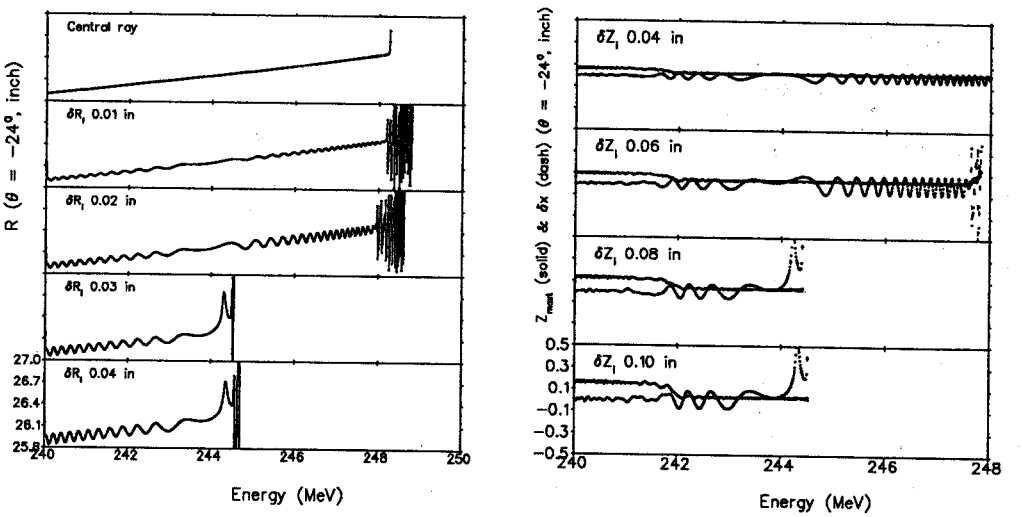

Figure 4: (Left) Plots of R ($\theta = -24^0$) vs. E for five median plane orbits. (right) Plots of R ($\theta = -24^0$) vs. E for orbits with combined radial and axial motion.

values of p_r will hit the inner or outer wall of the deflector. Our estimate of the transmission efficiency of the extraction channels is about 81%.

The median plane orbits with initial displacement of $0.01''$, $0.02''$, $0.03''$ and $0.04''$ are plotted in Figure 4 (left), together with the central ray orbit. It is obvious that the $\nu_r = 1$ resonance at an energy of 244 MeV puts a limit on the initial beam size (full radial width about $0.05''$) at 240 MeV which can reach a final energy of 248 MeV.

The orbits with combined radial and vertical motion are given in Figure 4 (right). It reveals that the relatively large axial amplitudes, those exceeding $0.06''$, produce an unacceptable growth in the radial oscillations due to the $\nu_r = 2\nu_z$ resonance. The particle cannot be recaptured by the stable region with such a radial oscillation amplitude after passing the $\nu_r = 1$ resonance and it will be lost by either hitting the septum or the wall of deflector during the extraction process.

We conclude that only the well centered beams at an energy of 240 MeV with physical size $\Delta r = 0.05''$ and $\Delta z = 0.08''$ could pass the $\nu_r = 1$ resonance and reach the final energy 248 MeV, and about half of them are successfully extracted.

The computation results and some important parameters of the K250 are summarized in Table 3.

The maximum intensity of 30 nA, calculated by utilizing the mathematic recipe, marginally meets the requirement for a medical machine. Unfortunately, the actual output current is expected to be less, probably much less, than this theoretical limit. Much of the beam is lost due to the resonance transition at the extraction region. This loss would have to be compensated by increasing power consumption. Besides, in order to produce a sharp and localized bump, needed for extraction, it is clear that a small vertical gap of the regenerator assembly is required and this will no doubt cause axial losses. In summary, the whole performance of the extraction system is restricted by the field imperfection near the $\nu_r = 1$ resonance. It is impossible to reduce the field imperfection to the tolerable range (≤ 0.1 gauss) since we would need to compensate the strong nonlinear edge field of the regenerator near the $\nu_r = 1$ resonance. In addition, we cannot totally avoid logistical problems such as machining errors, misalignment, etc..

Table 3: Parameters of the K-250 proton synchrocyclotron

Beam	
type of ions	H^+
output energy	248 MeV
maximum intensity	$\leq$ 30 nA
energy spread	$\leq$ 0.2 %
Magnetic structure	
number of sectors	3
spiral angle constant	4.407 deg/in
average field at extraction	3.591 Tesla
average field at center	3.314 Tesla
hill gap	2.5 inch
valley gap	$\sim$ 22 inch
RF system	
dee voltage	15 kV
resonating system	2 dees galvanically coupled in the C.R.
harmonic number	h=1
Central region	
type of source	P.I.G.
slit area of chimney	50 mm^2
distance between slit and puller	4 mm

In addition to the problems with the extraction system, conversion of the central region [14] appears to be extremely difficult. For both of these reasons we have abandoned the option of converting the K500 cyclotron into the K250 proton synchrocyclotron.

References

1. G. Bellomo, et. al., Magnetic field mapping of the K-500 cyclotron at M.S.U., MSUCP-30, 1980.
2. M. M. Gordon, Computation of closed orbits and basic focusing properties for sector-focused cyclotrons and the design of CYCLOPS, Particle accelerators 16, 1984, 39.
3. K.J. Lecouteur, The regenerative deflector for synchrocyclotrons, Proc. Phys. Soc., London, B 64, 1951, 1073.
4. K.J. Lecouteur, Perturbations in the magnetic deflector for synchrocyclotrons, Proc. Phys. Soc., B 66, 1953, 25.
5. K.J. Lecouteur, Non-linear regenerative extraction of synchrocyclotron beams, Phil. Mag. 46, 1955, 1265.
6. H.G. Blosser, et. al., Resonant extraction from three-sector low-spiral cyclotron, Nucl. Inst. Meth. 18&19, 1962, 488.
7. M.M. Gordon and X.Y. Wu, Beam extraction studies for a 250 MeV superconducting synchrocyclotron, N.S.C.L. annual report, 1986, 198.
8. A.V. Crewe and K.J. Lecouteur, Extracted proton beam of the Liverpool 156-inch cyclotron, Rev. Sci. Instr. 26, 1955, 725
9. A.V. Crewe and U.E. Kruse, Regenerative beam extraction on the Chicago synchrocyclotron, Rev. Sci. Instr. 27, 1956, 5.
10. J. Rosenblatt and R.J. Slobodrian, The magnetic deflector of the Buenos Aires 180-cm synchrocyclotron beam, Rev. Sci. Instr. 31, 1960, 863.
11. B. Allardyce, et. al., The extraction system of the improved synchrocyclotron, Proc. 7th Int. Conf. on Cyclotrons and their Applications, 1975, 287.
12. M. M. Gordon and V. Taivassalo, The Z4 orbit code and the focusing bar field used in the beam extraction calculations for superconducting cyclotron, Nucl. Inst. Meth. A247, 1986, 423.
13. D.A. Johnson, Private communication
14. Steve Synder, Private communication

AUTOMATED BEAM FOCUSING WITH BEAMMIN

J. Abate

The BEAMMIN program has been developed to automate the focusing of the beam exiting the cyclotron and reduce the human participation previously needed for this task. The program uses a mix of both hardware and software elements to focus the beam. While there are still a few corrections to be made, several tests have shown that this method is a viable alternative to the traditional method.

On the hardware side, a scintillating plate is inserted into the beamline to image the beam. A video camera aimed at the plate is linked to a MicroVAX workstation by a Data Translation DT2651 framegrabber. [1] Also used is a Data Translation DT2658 auxiliary frame processor to speed up computation intensive image processing such as image subtraction. The A-10QS, A-08QB, and A-06QA quadrupole magnets are used to focus the beam and the A-02DS dipole magnet is used to maintain the centering of the beam.

The program sets the quadrupole currents, recenters the beam if necessary, and captures the beam image. Background noise and other effects are filtered out and the beam area is measured. This process is repeated for each iteration of the minimization routine. This routine determines the settings of the quadrupoles that will give the minimum beam area and is the bulk of the BEAMMIN program. Several common routines for minimizing mathematical functions were tried, but they proved unsuccessful. Unlike mathematical functions which can generally be calculated rather quickly, each iteration of the minimization routine can take several seconds to perform, so it is crucial that the minimization be performed in as few steps as possible. Also, the minimization routine must deal with other complications such as fluctuations in beam quality and the possibility that the beam gets steered out of the field of view of the camera. Because none of the standard minimization routines could compensate for these effects, a custom minimization routine was written. In a limited number of tests, this minimization routine has performed fairly well. After some more trials have been performed and some improvements have been made to the user interface, BEAMMIN will be routinely used for beam focusing.

References

1. F. Marti, et al., "Beam Diagnostics Developments at NSCL", Proceedings of the 12th Int. Conf. on Cyclotrons, Berlin, 1989, pp 268-277

PROGRESS ON THE 8 TESLA MAGNET

J. Kim, L. Lee, and J. Schubert

I. Introduction

The main coils of the 8 tesla magnet have been wound and tested. The winding required roughly four weeks for each of two coil sets. The coils were wound on a winding form rather than on the bobbin directly, so that the inner surface floats from the bobbin [1]. This scheme was realized by removing the winding form after the winding was completed. The advantage of the floating coil is that the large shear stresses on the boundary between coil and bobbin are completely avoided.

After the superconductor and banding were wound, the two sets of coils are welded onto the midplane structure, and electrical connections between two were made before testing the coils in a commercial liquid helium dewar. The coils were energized in the test dewar to detect possible faults in the winding process. No flaws were found, but the current could not be delivered up to the level generating maximum hoop stress on the coil (equivalent to the 8 tesla field with iron yoke) due to the effects of strong magnetic forces on the nearby iron structure and the excessive voltage drop on the temporary current leads. Training behavior was not observed, but the big coil quenched once at 250 amps when the LHe level was below 75% of the entire coil height. The quenching is thought to be initiated by disturbances near the lead joint from which the normal region propagated into the coil.

II. Winding of 8 T coils

The materials and procedures for winding superconducting (sc-) coils had been prepared carefully. One of the main items in preparation was layer transition spacers which are made of G-10 fiberglass composite. They were cut from sheets of G-10 stock with a saw blade installed at the horizontal milling machine and thermally formed to a round shape to match the curvature of the bobbin without a strong bending tension. The thickness of G-10 spacers was an important parameter because any difference in thickness between the sc-wire and spacer would be multiplied by the number of layers wound. After test winding a smaller coil, we decided that the spacers should be 0.001" thinner than the sc-wire. The rationale for choosing the thinner spacers was that they could easily be thickened by adding paper shims, while thick spacers would need to be ground to the proper dimension. After about 20 layers were wound, the coil was visibly convex, with the center higher than the edges by about 0.005"-0.01". The correction was not made by adding paper, but rather by adding extra epoxy

underneath the spacer so that a further significant non-uniformity was prevented. The maximum variation in diameter after winding was finished was 0.016".

Another problem requiring correction was the non-uniform width of the sc-wires. The width of the wire for each spool differed by a maximum of 0.002" owing to the non-uniform thickness of formvar insulation. The wider wire was used for the first set of coils. In order to have the same number of turns (1362 turns for the small coil and 2904 turns for the big coil) for the second set, it was necessary to make the final layer incomplete. The empty space was filled with two G-10 plates which were thermally set to the round shape like layer transition spacers.

The potted coils were cured in the big oven for one day. The coil temperature was measured to ensure sufficient heating time for an entire volume. The diameter of the coil was measured before and after curing with pi-tape. A quite uniform reduction of diameter by 0.008" was measured. Almost all of the prestress of the banding seemed to be relaxed during curing, presumably since the epoxy seeps into the empty spaces in itsfluid state. The STANSOL [2] calculation tells us that the hoop stress on the conductor at an 8 tesla field may reach 20000 psi without a banding preload. The relaxation of the preload during the curing process should be investigated more carefully.

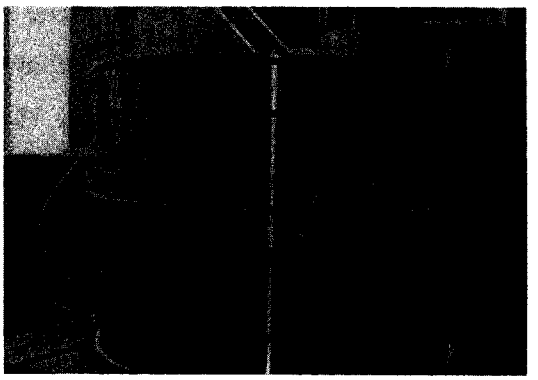

Figure 1: The coil package is ready to be tested. LHe level and temperature sensors are attached, and one of the leads is showing.

III. Coil Test

Two mirror image coil sets were welded onto the midplane structure before testing (Fig. 1). The coil package was then moved into a small LHe container built to reduce the quantity of LHe (Fig. 2) required for the test. A relatively long current lead (4 meter) was needed to make a connection from coil to existing 500 amp commercial current leads. The connection leads are made of four conductors in parallel obtained from spare K500 superconductors.

In the first test run the big coils quenched at 250 amps. The quench occurred at a LHe level of 75% of the entire coil height. At this level the current leads leading to the upper coil could not be directly cooled by liquid helium. One probable explanation is that the normal zone near the joint propagated into the coil with the help of disturbances by wire motion or by contact with warm He gas. As the test was continued immediately after the LHe feed was stopped, the gas motion inside the dewar

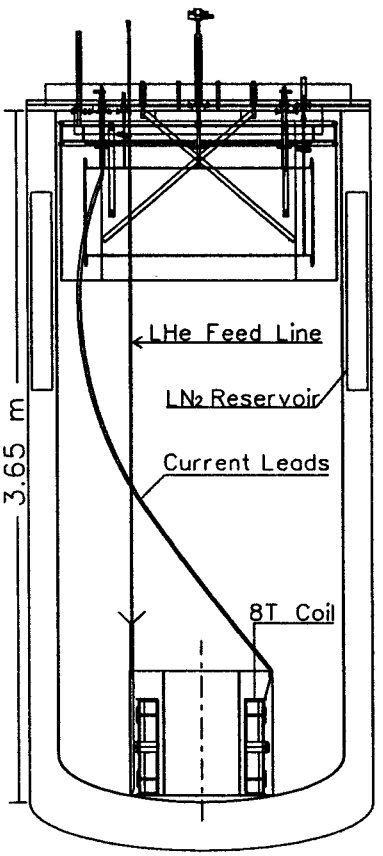

Figure 2: A schematic view of the test dewar with the coil inside. Long current leads reaching to the 500 amp commercial current leads and LHe feed line are shown.

might not bave been stabilized enough for a proper test. The heat generated on the joint is roughly estimated to be 10^{-4}watt at 200 amps, which is usually negligible under good cooling conditions. However, with small disturbances this normal region could propagate into the coil. The next test was done with the LHe container full. The big coils ramped up to 350 amps without quenching. The hoop stress on the coil at that current level corresponds to 6 tesla with iron yoke in place. The current was ramped up at the same rate as in the first test to see if eddy current heating was the cause of the quench during the first run, but this turned out not to be the cause. A higher current was not tried as the voltage drop in the commercial current leads rose to 150 mV (100 mV is considered to be the maximum safe operating voltage), and more importantly, so as not to induce strong magnetic forces on the iron structures nearby.

The small coils reached 430 amps without quenching. To reach a higher current than in the big coil test, the dewar pressure was raised from 1 psig to 3 psig, allowing more gas flow through the current leads and thus holding the voltage drop to 150 mV for a short period of time. The heat leak in the dewar plus current leads was measured to be 4.7 l/hr with no current, and 7.2 l/hr with a current of 250 amps.

IV. Present status

The winding and testing of all coils has been completed without major problems, and the machining of the magnet steel is in progress. The assembly of the whole magnet will be completed in the near future.

References

1. J. Kim et al.,"Progress on the 8-tesla magnet",NSCL Annual Report(1990), p215
2. W.H. Gray, D.L. Levine, Oak Ridge National Lab (1976)

EXPERIMENTS WITH THE LIQUID HELIUM CRYOVESSEL

J.W. Kim

I. Introduction

Even though the cryovessel was built about two years ago, the experimental results have not yet been published. Further experiments have been carried out recently with flow and pressure control systems, but this report is confined to the initial experiments performed immediately after construction was completed.

As the first experiment, the heat leak on the vessel was measured. The boil-off helium gas was vented to the atmosphere as well as to the suction line of compressor (helium recycle mode). The minimum heat leak was obtained when the effluent gas was vented to atmosphere. The convection heat transfer in the current leads when the lead is horizontal [1] was simulated first with a test tube (first empty, then filled with many teflon tubes), and then with real current leads designed for the 8 tesla magnet [2]. The temperature difference between top and bottom of the tube indicated the large convection current when the tube was empty. It seems that there are heat transfer mechanisms caused by helium pressure oscillations inside the vessel. These acoustic oscillations were observed by a microphone connected at the end of the test tube filled with teflon tubes.

II. Heat leak

To measure the heat load on the vessel itself, the current lead port was blanked off. The boil-off helium gas was then vented to the atmosphere to avoid the pressure fluctuations from the suction line of the refrigerator. The heat leak and temperatures on the shields are shown in Fig.1. The characteristics of the vessel are displayed clearly here; the heat leak is determined by the temperatures of the shields, which are determined by three factors: 1) the heat influx from the outside, 2) the cooling power of outgoing helium gas, and 3) the thermal mass of the shields. The first two factors determine the final equilibrium temperatures. The third determines the speed of temperature changes. The slope of the curve is not reproducible, since the initial temperatures on the shields are determined by the particular liquid helium transfer conditions for a given experiment.

To reach the equilibrium state faster, the shield temperatures should be kept near their equilibrium values at the beginning of an experiment. We tried opening the pumping port during the filling process as a return path for outgoing gas, so that the cold gas does not cool down the shields by direct contact. However, since both shields are thermally connected to the neck tube, their temperatures dropped with nearly the same rate as when all of the boil-off was used to cool them.

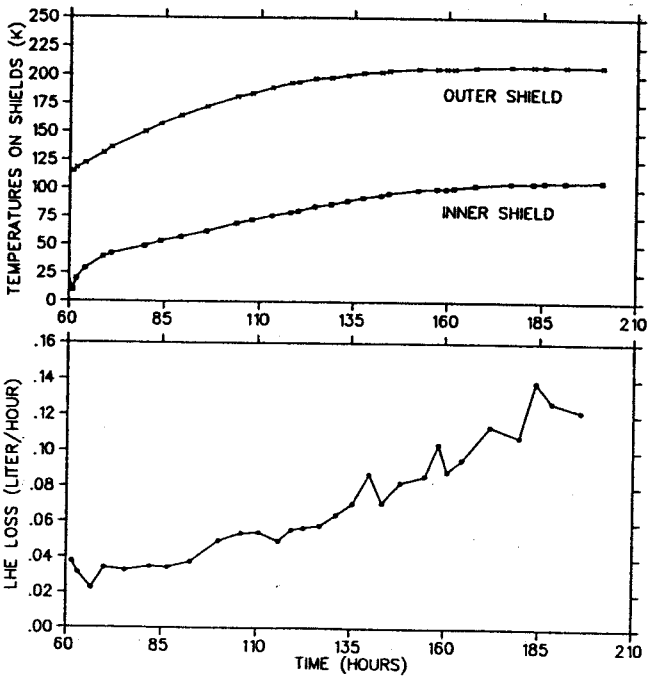

Figure 1: Heat leak and temperatures on shields when the test tube port is blanked off. The boil-off gas is vented to atmosphere.

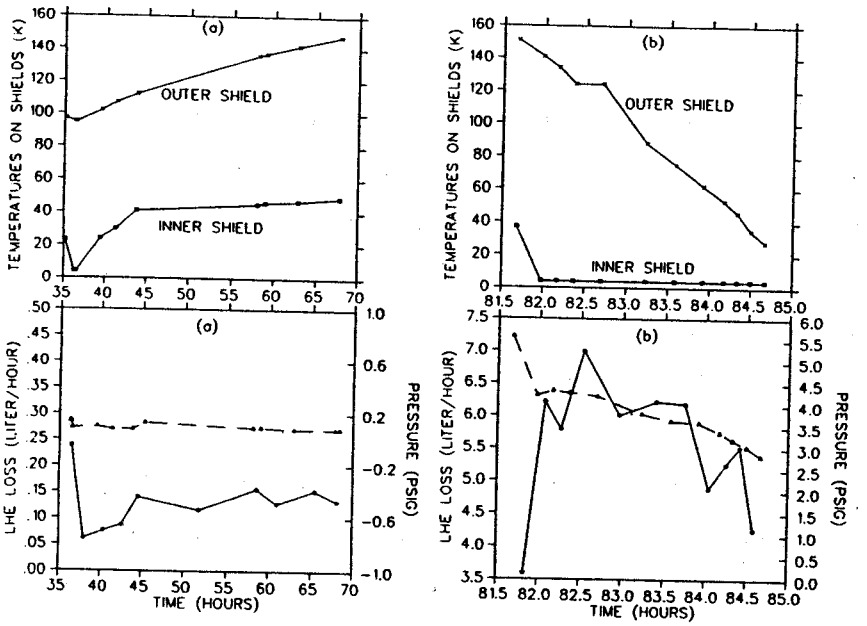

Figure 2: Measurements when the test tube is empty and vented to the suction line a) for a vertical orientation of the test tube, and b) for a horizontal orientation. More than 10 times greater heat leak is measured for the horizontal orientation, which is explained by a large convection current in the 5/8" OD tube. The dashed line corresponds to the pressure in the vessel. The LHe loss should be converted to heat leak (taking the pressure into consideration) for a proper comparison.

Controlling the shield temperatures by a heater was considered, but it was not tried since the heat leak on the vessel itself could be calculated from the inner shield temperature. This is possible as the heat leak curve at Fig.1, for example, can be calculated roughly by assuming that conduction and radiation are the only heat transfer mechanisms. Therefore the measured helium boil-off rate can be used to identify the heat transfer by other sources if they are large enough for proper estimation.

III. Convection in the test tube

The heat transfer by convection in the test tube which connects the ambient and LHe temperature region like the actual current leads was studied first. As mentioned in ref.[1], the magnitude of convection currents depends on the dimensions and orientations of the tube. The effective diameter of the tube was varied by filling it with smaller teflon tubes (O.D.=0.062"), and orientation was varied by tipping the vessel 45 degreee in either direction. With test tube empty the heat leak was measured for each orientation shown in Fig.2. While the heat leak for vertical orientation was about 0.14 l/hr, an average of 5.5 l/hr is measured for the horizontal orientation (corrections for the different pressures should be made for a proper comparison). The negative slope in the case of the horizontal tube presumably indicates that additional heat loss is added while reaching a new equilibrium temperature distribution inside the helium container (this process should be fast in principle, so other phenomena may happen inside). Another indication of the strength of the convection current came from the temperature difference measured between top and bottom of the tube in the horizontal orientation. The difference measured by platinum sensor was 21K (20K and 41K at the bottom and top of the tube, respectively). With test tube filled by smaller teflon tubes the large convection disappeared; no temperature difference was observed.

Table. 1 Test tube filled with smaller size teflon tubings (vented to air).

Position & Flow in tube		Heat load	LHe consumption
Vertical	0.8 SCFH	0.12 Watt	0.16 liter/hr @1.0atm
	No flow	0.20 Watt	0.27 liter/hr @1.0atm
Horizontal	0.9 SCFH	0.16 Watt	0.22 liter/hr @1.0atm
	No flow	0.34 Watt	0.47 liter/hr @1.0atm

The helium boil-off rate was varied by the helium gas flow through the test tube. The results are shown in Table 1. The convection still seems to exist for the horizontal orientation since the table shows that the heat leak decreases as the gas flow destroys the convection current, but the strength is much smaller than in the case of the empty tube. The heat leak is also reduced when the helium gas is allowed to flow through the vertical tube. It is believed that some portion of the heat influx through the test tube, as well as the convection current, is removed by gas flow. From these observations the convection in the real current lead, which has many tiny paths through the conductor, is inferred to be small. Later experiment confirmed this hypothesis within the error range.

IV. Pressure fluctuations

When the helium boil-off was returned to the suction line, the heat leak was much higher than when it was vented to the atmosphere. Therefore, there must be additional heat leak mechanisms which occur in the vessel. Some explanations have been considered. First, as the suction line pressure rises, warm gas flows back into the vessel. This phenomenon was observed by an increased temperature measured by a platinum sensor attached on the return line near the main neck tube. A relief valve was then inserted to control the pressure and to prevent a reverse flow. This reduced the heat leak, but it was still higher than when venting to the atmosphere. Secondly, a small thermal oscillation could be developed by flow disturbances, even those caused by the action of the relief valve. The acoustic oscillation has been detected with a microphone connected at the end of the test tube when it was filled with teflon tubes. The schematic display on the oscilloscope is shown in Fig. 3.

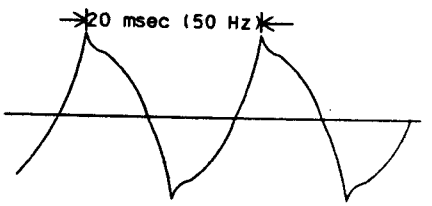

Figure 3: Schematic shape of the acoustic oscillation observed on the oscilloscope with a microphone connected at the end of the test tube filled with teflon tubes.

Disturbances of the outgoing gas may occur partly due to the copper liner covering the liquid helium. This could be observed by turning on the level sensor. The heat generated by the liquid level sensor which is usually intercepted by outgoing helium gas seemed to be transferred to the liquid helium via the copper liner. With the sensor turned continuously on, an average of 1 watt of heat leak was observed while the liquid level changed from 46% to 16%.

V. Current lead test

The cryovessel was used to test prototype 500 amp current leads. The heat leak as a function of current is shown in Fig. 4. The data include the heat leak from the vessel itself, which is not

subtracted because it is difficult to know how much additional heat leak the flow disturbance contributes. In comparison with other lead tests [3] the heat leak looks higher at low currents. The reason for this is not known yet.

VI. Conclusion

The heat leak in the cryovessel seems to follow the inner shield temperature changes, which is a result of the vessel utilizing the boiled-off helium gas as its only cooling agent. To satisfy the constant heat leak requirement as a test vessel, the shield temperature should be controlled, and, to avoid thermal oscillations, the outgoing gas flow should not be disturbed (this is required in all circumstances). The convection heat transfer resulting from different dimensions and orientation of the test tube was demonstrated with the tube empty and then filled with smaller teflon tubes. The thermal acoustic oscillations were observed. These are thought to be driven by disturbances of the outgoing gas partly due to the copper liner covering the top of the liquid in the vessel. The measurement of LHe boil-off had contributions from heat sources other than radiation and conduction, except when the outgoing gas was vented to the atmosphere. A complete analysis of helium vessel would be a difficult task. A more systematic approach may be needed for a better understanding of phenomena occuring inside the vessel.

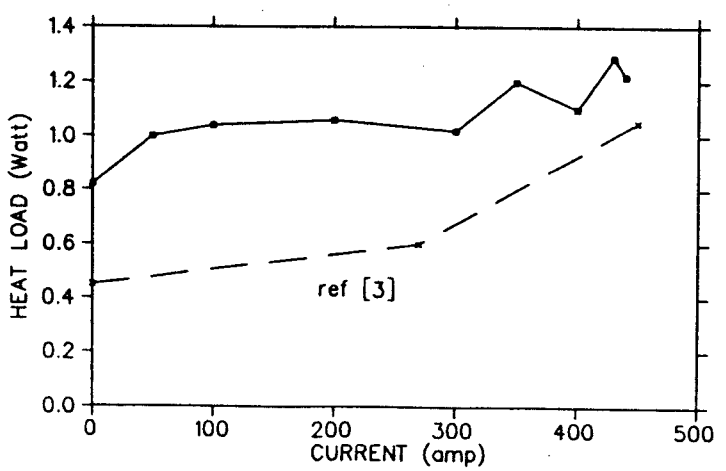

Figure 4: Heat leak through current leads shown as a function of current. The higher heat leak at the low current values, compared with other leads, has not been investigated.

References

1. J. Kim et al., Cryovessel for the current leads test, NSCL Ann. Report(1990), p195
2. J. Kim et al., Progress on the 8 tesla magnet, NSCL Ann. Report(1990), p215
3. J. Purcell, private communication with H. Blosser

APPLICATIONS OF SYMPLECTIC SCALING

G. H. Hoffstätter and M. Berz

The particle transport through beamlines, isotope separators, spectrographs, and other devices often depends strongly on the fringe fields of the optical elements involved. A method to compute those effects efficiently was developed; its use will be demonstrated for several properties of the A1200 isotope separator.

In last year's annual report[1], it was discussed that the computation of transfer maps can be performed very quickly using differential algebra evaluation of the propagator of motion in the case that the maps describe particle motion through the main–field region of optical elements[2]. However, if the fields change along the central trajectory, very time consuming numerical integration has to be used. We developed an efficient approximation method using the scaling properties of maps. To ensure the symplecticity of the approximated maps, we analyzed which implications these scaling properties have on symplectic representations of the map, namely the generating functions and the Lie exponents[3,4]. This approach is usually very accurate and much faster then numerical integration. Meanwhile this method was tested on several examples, some of which will be presented here. An analysis of accuracy and speed was made with the result that symplectic scaling is now included in the most resent version 6 of COSY INFINITY[5], which was distributed to the users at the end of 1992.

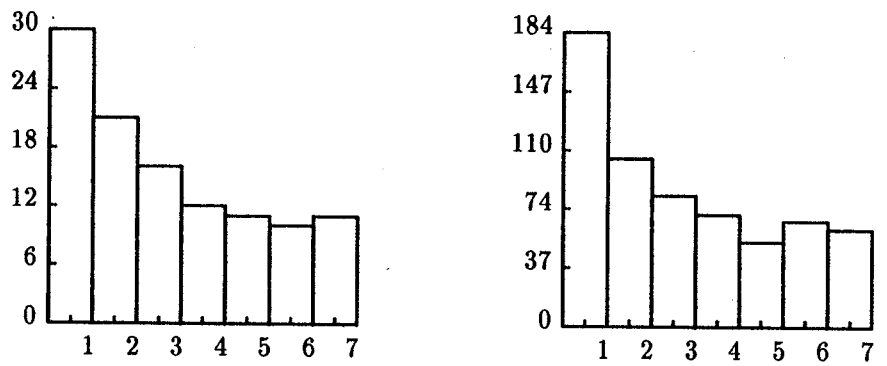

Figure 1: Factor of time advantage of SYSCA to numerical integration with as a function of the order of the map. Left: Quadrupole, Right: Dipole.

The symplectic scaling (SYSCA) approximation is especially helpful in the design of a realistic system after approximate parameters of the elements have been obtained by neglecting fringe fields. These values can be used to create a reference file for symplectic scaling. In this way, a very high accuracy almost equivalent to accurate but time intensive numerical integration of the map can be obtained. The time advantage of this method is illustrated in figure 1.

Fringe fields do have noticeable effects already in first order. In the example of the A1200[6] isotope separator at the NSCL, the effect of the fringe fields on the calculated setting of the field strength is shown in figure 2. The fringe fields were described by Enge functions, and the Enge coefficients had been fitted to measured field data. Here the time advantage of the proposed approximation in the fit is three minutes versus two hours. As a measure of accuracy, we study the tilt angle Θ of the dispersive image plane and the opening aberration C_0 for various approximation methods. In the discussed device the coefficient $(x|aa)$ vanishes because of symmetry of the axial ray and anti symmetry of the dipole fields; therefore $(x|aaa)$ is the relevant opening

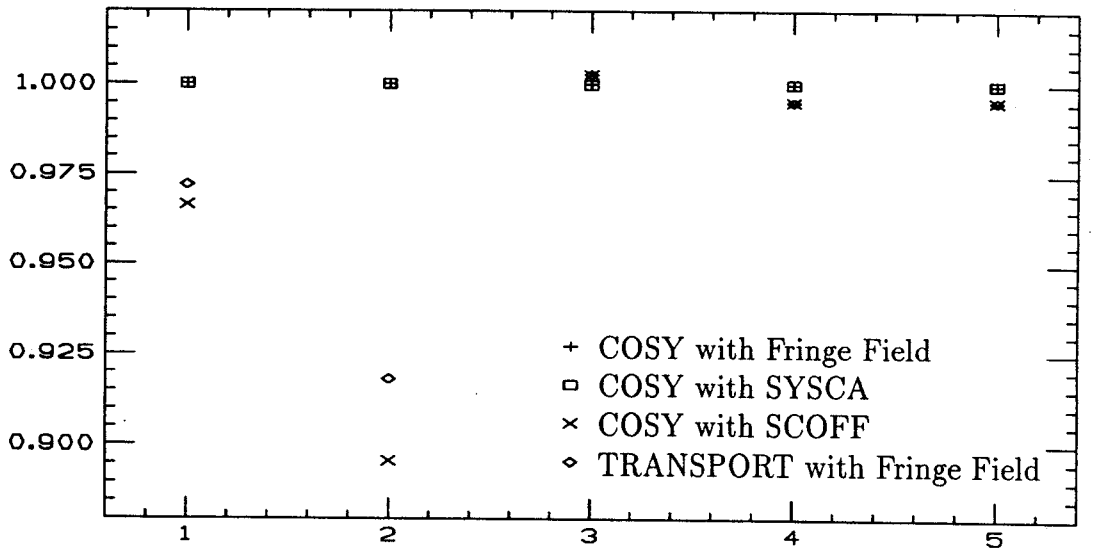

Figure 2: Relative deviation of predicted field settings with SCOFF and SYSCA from the correct settings for five quadrupoles. The standard fringe field approximation of TRANSPORT is given as a reference; the deviation is mainly due to the approximation of quadrupole fringe fields.

aberration,

$$\Theta = -\frac{(x|a\delta)}{(a|a)(x|\delta)} \quad , \quad C_0 = (x|aaa) \; . \tag{1}$$

Table 1 shows Θ and C_o for various fringe–field models. The values of Θ with and without fringe fields differ by 0.5% for the first dispersive image plane in the A1200; the third order aberration, however, is completely wrong if fringe fields are disregarded. This comparison also shows that quadrupole fringe fields, although often disregarded, can have effects which dominate over dipole fringe fields. Nonlinear effects can be seen by sending a cone of particles through the 7^{th} order A1200 map. The images with SCOFF and SYSCA approximation are shown in figure 3. The maximum angle used is 15mrad.

The effort involved in generating a symplectic approximation is rewarded when repetitive tracking is being performed. The example lattice of choice is the proposed PSR II Ring at Los Alamos National Laboratory. The 9^{th} order 5000 turn tracking pictures are displayed in figure 4. The tracking was performed with the described standard numerical integration, SYSCA, and a nonsymplectic fringe–field approximation obtained by low accuracy numerical integration. Nonsymplectic tracking rapidly destroys the phase space. SYSCA yields

Θ and C_0 with SCOFF approximation	80.8840°	−65.96m
Θ and C_0 with dipole fringe fields only	81.1696°	−65.96m
Θ and C_0 with quad fringe fields only	81.2694°	−682.68m
Θ and C_0 with SYSCA approximation	81.2701°	−687.10m
Θ and C_0 with actual fringe fields	81.2702°	−687.10m

Table 1: Tilt angle and opening aberration for various fringe–field models.

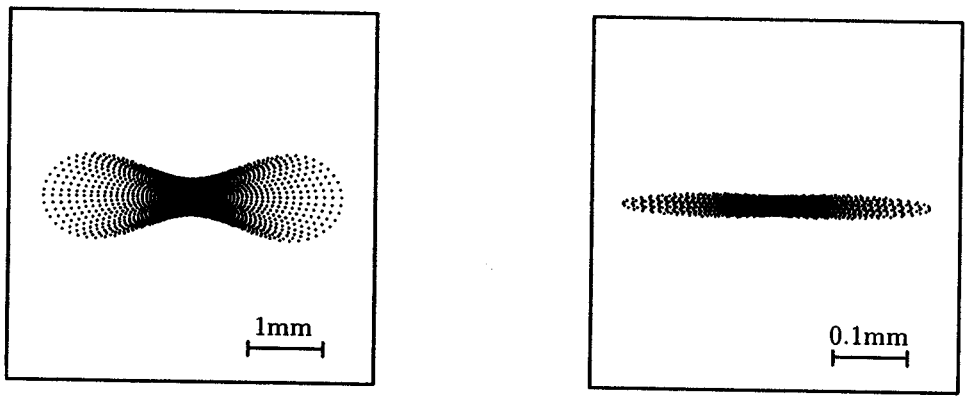

Figure 3: Beam spots with SYSCA (left) and SCOFF (right) approximation. The plot produced with the exact fringe fields can not be distinguished from the plot produced with SYSCA.

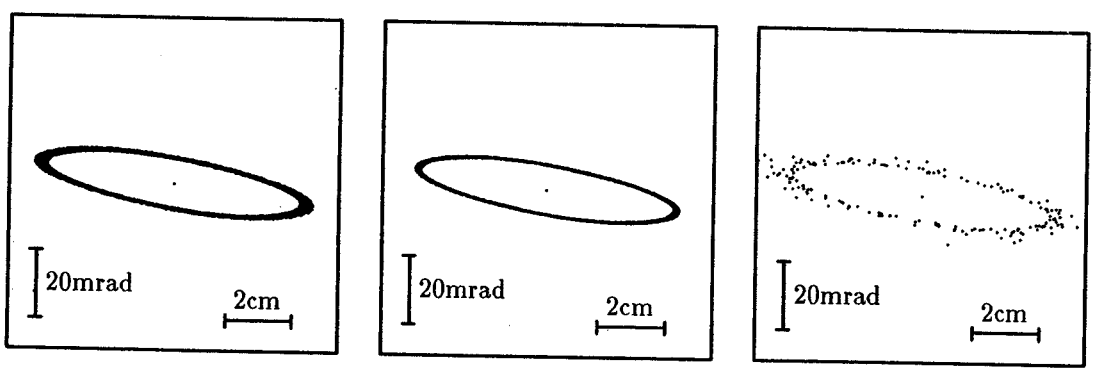

Figure 4: 5000 turn tracking with fringe fields obtained by numerical integration (left), SYSCA (middle), and a nonsymplectic fringe field approximation (right). The initial position of the particle is $(x, y) = (3\text{cm}, 3\text{cm})$ with no initial inclination.

more stable results than the numerical integration since the limited accuracy of the numerical integrator slightly violates symplecticity. The corresponding 9^{th} order maps were produced with the SYSCA mode in COSY INFINITY in 30 minutes, whereas the standard numerical integration took 15 hours, and the nonsymplectic approximation took 44 minutes on a VAX 4000–90 computer.

References

1. G. H. Hoffstätter, M. Berz, NSCL Annual Report, 236 (1991)
2. M. Berz, Nucl. Instr. and Meth. A298, 426 (1990)
3. G. H. Hoffstätter, M. Berz, Proc. to Comp. Accel. Phys., to be publ., (1993)
4. G. H. Hoffstätter, M. Berz, Proc. to Part. Accel. Conf., to be publ., (1993)
5. M. Berz, COSY INFINITY User's Manual, MSUCL-869 (1993)
6. B. M. Sherrill et al. The First Intern. Conf. on Radioactive Nucl. Beams, Berkeley, World Scientific Publishing (1990)

FOUR CELL THIRD ORDER ACHROMATS AND THEIR APPLICATION TO MULTI-PASS TIME-OF-FLIGHT SPECTROMETERS

Weishi Wan and Martin Berz

Due to the Hamiltonian structure of motion in particle optical systems, the time of flight in an achromat depends only on energy [1]. So we adopted the idea of converting a storage ring into a high resolution time-of-flight energy spectrograph by redesigning it as a third order achromat. In [2],[3],[4] we displayed a new method to design third-order achromats which for the first time made use of mirror symmetries. The designing process of the achromat is presented below, where the strengths of the multipoles are found quite feasible. Also shown in this report is our analysis of the new ring which includes the long term stability of the system and the resolution it can achieve.

In order to design a circular machine as a third order achromat, no switched (S) or switched-reverse (C) sections can be used. Therefore the only choice is patten FRFR. This means that the first order map of the forward cell has to have $\mu_x = 90deg$ or $270deg$ [3]. The ring contains six dipoles, twenty quadrupoles, eight sextupoles as well as RF cavities, beam cooling devices, and the injection-extraction system. Two long straight sections divide it into two identical parts, each of which is symmetric about its center [5]. It is much easier to take half rather than a quarter of the ring as the forward cell. Consequently, the other half should be the reversed cell, and an achromat corresponds to two turns of the ring. Since there are five conditions for a symmetric cell to meet [4], it is sufficient to fit only the quad strengths to find a desired solution. Thus the first order layout of the existing ring is preserved. Also because of the symmetry, the forward cell is a first order achromat. The field gradients of the quads are displayed in Table 1.

Ten sextupoles were placed symmetrically in the forward cell. The values of the field satisfying the conditions for the second order map were found using the nonlinear optimizer in COSY INFINITY (Table 1). The same was done with the third order correction except that there are more octupoles after the third bend than before the first one. The positions of some of the multipoles were carefully chosen to limit the required field strengths (Figure 1 and Table 1).

Since our goal is to make the ring a multi-pass time-of-flight spectrograph, the long term behavior becomes of vital importance. It was studied with an 11th order one turn map which was generated by COSY INFINITY and used for non-symplectic tracking. The 200 turn dynamical apertures for both horizontal and vertical motion were determined by analyzing phase space plots. For particles of momentum spread $\pm 0.5\%$ to survive 200 turns, they are roughly 100 π *mm mrad* horizontally and 15 π *mm mrad* vertically. As an example, Figure 2 shows the horizontal motion of on-energy particles up to 200 turns.

The resolution of this machine was determined in a statistical way. First, the 9th order one turn map was computed. Secondly, a large number of particles (1000) inside a certain phase space area were produced randomly by COSY. Then these particles were sent through the one turn map n times, therefore the n-turn time-of-flight of each particle was computed. Considering the random errors of the detector, which were assumed to be about 100 *ps*, the predicted energy deviation of each particle was calculated. Finally the difference between the predicted and initial energy deviations was obtained and the resolution of the ring was determined by calculating the inverse of the average differences. The dependence of the resolution on the number of turns and the emittance is presented in Figure 3.

Element	Field Strengths (T/m,T/m^2)	Element	Field Strengths (T/m^3)
Quadrupole1	5.2141708710097464	Octupole1	-285.07749404229136
Quadrupole2	-3.7780943756357911	Octupole2	368.94910085314347
Quadrupole3	-0.2757583566872618	Octupole3	614.99793829516426
Quadrupole4	-1.0861967098567489	Octupole4	680.30311596846740
Quadrupole5	2.1018617072758571	Octupole5	-5442.7323531935168
Sextupole1	-12.655855454352217	Octupole6	4250.2409995782432
Sextupole2	8.0550942902064335	Octupole7	-837.91940849587759
Sextupole3	-14.549046698823922	Octupole8	-1920.2296769772195
Sextupole4	15.697993340520378	Octupole9	3595.6586358546853
Sextupole5	0.8844613366417970	Octupole10	-2187.7620170696497
Sextupole6	-53.905125612548678	Octupole11	2622.2366537113714
Sextupole7	66.227372392466883	Octupole12	-1494.9597751428264
Sextupole8	-16.648568962020669	Octupole13	-757.00955057500670
Sextupole9	-0.1067654043405714	Octupole14	305.17394857470414
Sextupole10	3.4540652334940187	Octupole15	-146.44242626707558

Table 1: The field strengths of the multipoles

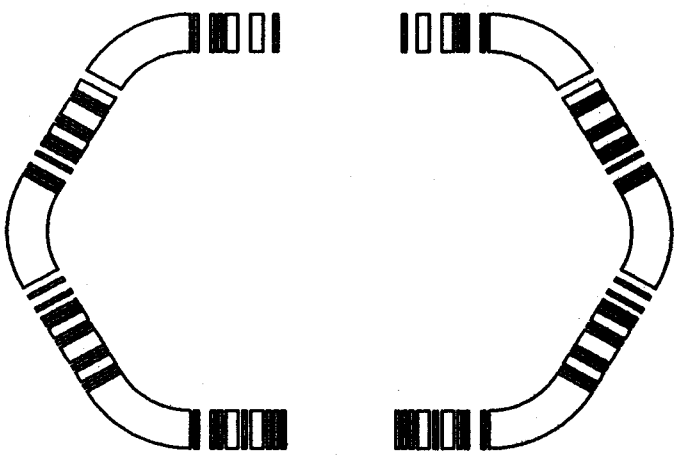

Figure 1: The layout of the ring; the long multipoles are quads and the short ones are sextupoles and octupoles

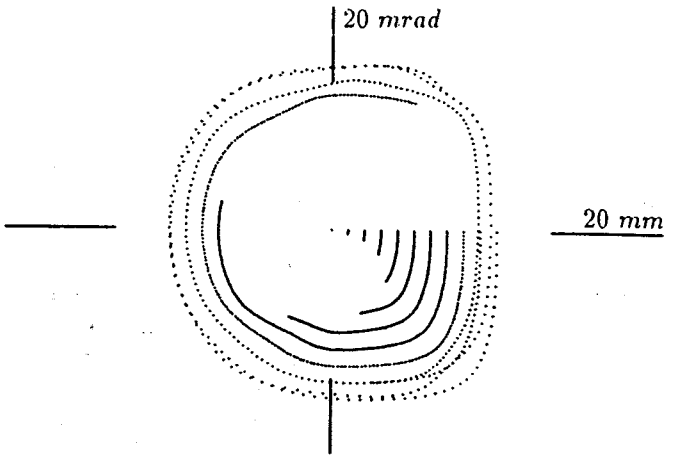

Figure 2: 200 turn 11th order tracking of the x-a motion of on-energy particles

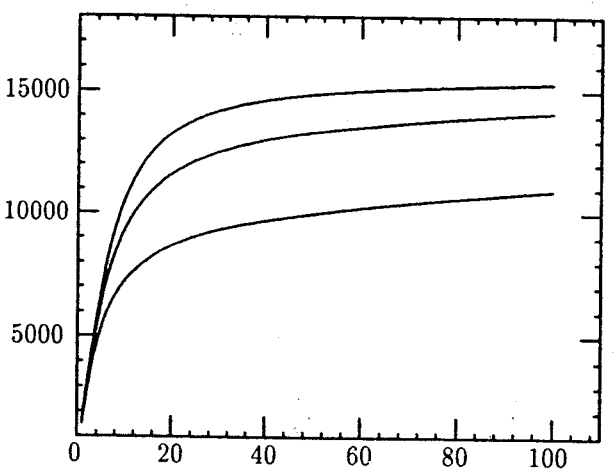

Figure 3: Resolution vs number of turns at different emittances

References

[1] H. Wollnik and M. Berz, *Nucl. Instr. Methods* A238 127 (1985).

[2] W. Wan, E. Goldmann and M. Berz, *Proc. Workshop on Nonlin. Effects Accel. Phys.*, Berlin (1992). M. Berz, S. Martin and K. Ziegler (Eds.), IOP Publishing, Bristol.

[3] E. Goldmann and M. Berz, *NSCL Annual Report* 232 (1991).

[4] W. Wan, E. Goldmann and M. Berz, *Proc. Comput. Accel. Phys. Conf.* (1993). To be published.

[5] B. Franzke, *Nucl. Instr. Methods* B24/25, 18 (1987).

TREATMENT GANTRIES WITHOUT A MIDPLANE SYMMETRY FOR CANCER THERAPY

Martin Berz and Weishi Wan

The past years have seen an increase in the use of particle beams for cancer treatment. The last peace of the beamline delivering the beam to the patient, the gantry, usually rotates around the patient to deliver beam from different directions. Among the ideas which have been developed in the past, probably the simplest one is to bend the beam by 90 degrees three times in one plane and lead it back perpendicularly to the gantry's axis of rotation where the patient is located. Because of space requirements, other designs are usually favored, including a design from a group at Harvard University [1]. It contains two parts which are first order achromatic individually. The mid-plane rotates 90 degrees from the first part to the second, and the total system is achromatic in both planes.

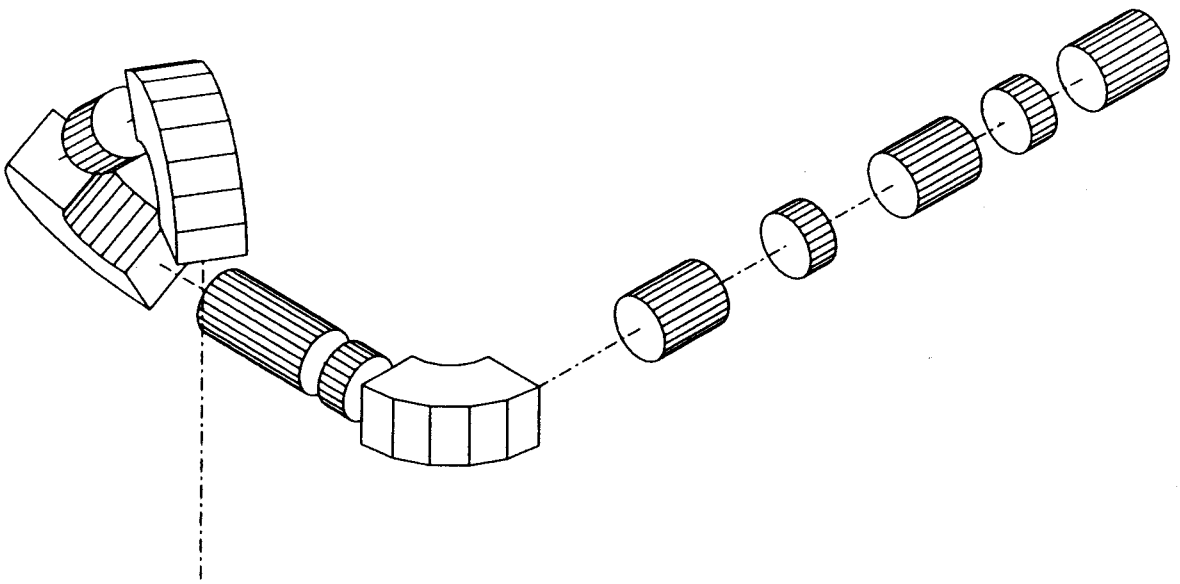

Figure 1: Our three dimensional gantry

In order to optimize the space requirements of gantries, we studied achromatic systems which do not separate in two achromatic subsystems but which are still globally achromatic. By introducing one more plane into the system, we adopted a new idea which enables us to achieve compactness and free space simultaneously. The resulting system is fully three dimensional because it guides the beam from and to the axis perpendicularly at different places and from different directions (Figure 1). The core idea of connecting the three different planes is based on using solenoids which rotate by exactly the angle of tilt between two consecutive planes. In this way, the linear motion still appears to be in one plane and can be corrected similar to any other one plane achromat. In order to adjust the whole system for small final spot size, higher order correction of the midplane and non-midplane terms is required. This is performed with COSY INFINITY, which allows a full simulation of the non-midplane motion and simultaneous optimization of even large numbers of variables.

Figure 1 shows the three bending sections with one dipole each. Dipole1 bends by 90-degrees and the

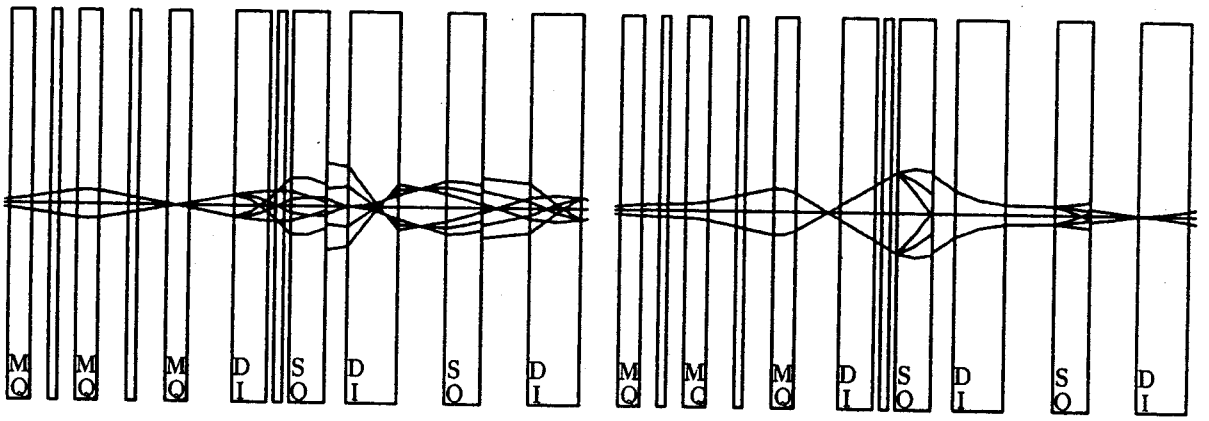

Figure 2: First order beam layout (achromatic). Left, x-z plane; right, y-z plane; same below.

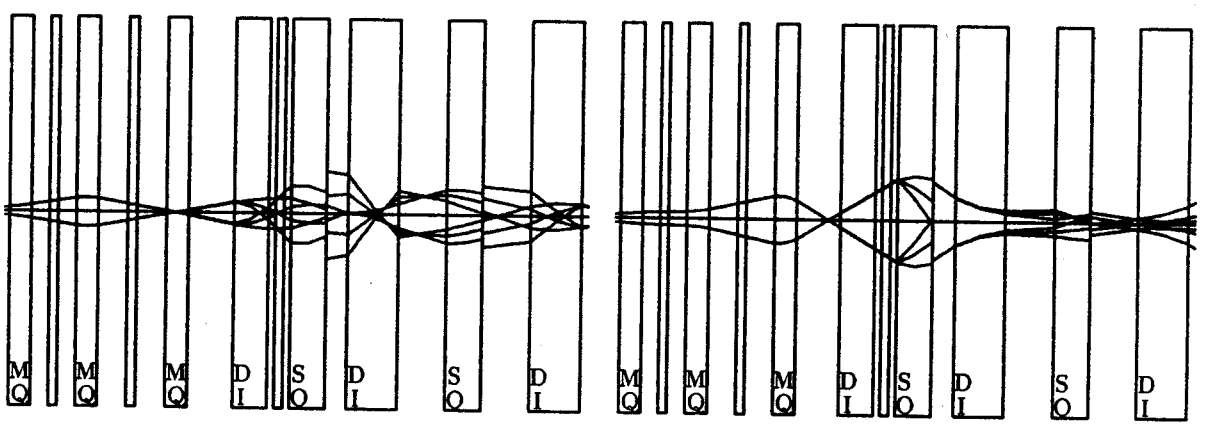

Figure 3: Third order beam (achromatic) without higher order correction.

other two are identical 139-degree dipoles with edge focusing. Two identical solenoids are placed in the two intervals among the dipoles. All three quadrupoles are before dipole1 in order to minimize space and the number of moving parts.

The first step of our design is to fit the strengths of the solenoids so that they rotate the mid-plane 60 degrees (solenoid1) and -41.4 degrees (solenoid2) respectively . This was done by fitting the solenoid-rotation map to be x-y decoupled. Next, the whole system was fitted to a first order achromat by varying the strengths of the quadrupoles and the edge angles. Figure 2 displays the resulting first order beam layout and Figure 3 presents the corresponding third order one. Both of them show that the beam is quite narrow transversely and uniform longitudinally. The linear magnifications of both x and y direction are about $2 \sim 2.5$, which is quite small.

The sharp difference between Figure 2 and Figure 3 implies that substantial second and third order aberrations remain in the system. This is particularly obvious in the y-z plane where the outgoing beam in Figure 3 is 3.5 times wider than that in Figure 2. Sextupoles and octopoles are added to correct those aberrations. Clearly their number is critical, and after several attempts, a feasible solution with only one octopole and three sextupoles was found without worsening the beam quality. During the above process, it proved efficient to give

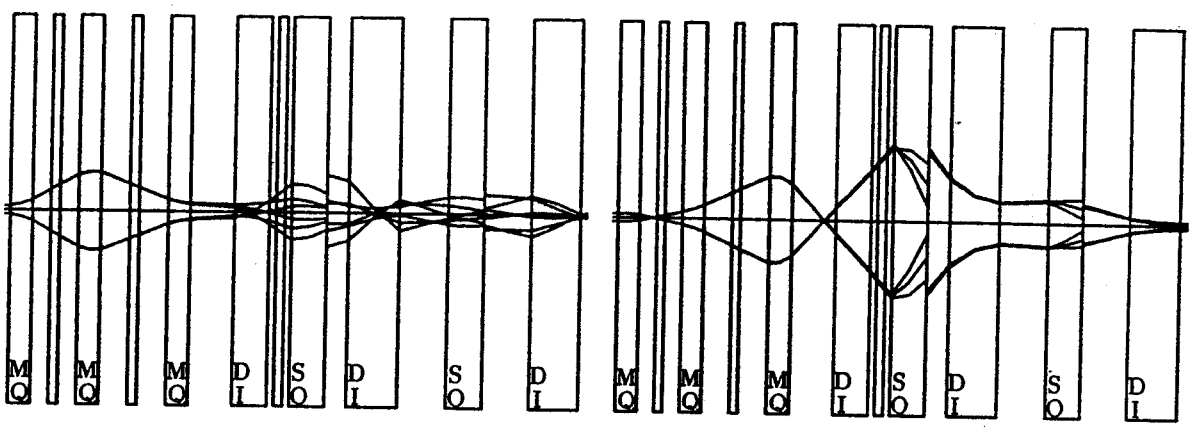

Figure 4: Third order beam (nonfocusing) with higher order correction.

Element	Field(T)/Angle(DEG)
Dipole	4.30
Solenoid1	-5.60933474052
Solenoid2	3.87044084989
Quadrupole1	-0.693223982592
Quadrupole2	0.234756307840
Quadrupole3	-0.345110812079
Angle2	-28.2356288039
Angle1	-22.2146351454
Sextupole1	0.495824883950E-01
Sextupole2	-0.591266144844E-01
Sextupole3	-0.768441284703E-01
Octupole	-0.391648872021E-01

Table 1: The field values and edge angles of all elements for guiding 200MeV proton

up the condition of linear imaging but rather demand a minimum total spotsize, resulting in a smaller spot size. In this process, the x-magnification drops from 2.7 to 1.6 and y-magnification from 3.1 to 2.1. (see Figure 2 and Figure 4). The final parameters of the gantry are listed in Table 1 for a proton energy: 200MeV. It suggests the dipole and solenoids to be superconducting, while for the other magnets also conventional techniques seem reasonable.

We have designed a feasible compact gantry beamline without mid-plane symmetry. The role of solenoids in rotating the mid-plane has been studied. The final spot size has been minimized by tuning the system away from imaging and correcting the higher order aberrations simultaneously. The number of magnetic multipoles has been minimized without affecting the beam quality. This design presents a new alternative of cancer therapy gantry beamline.

References

1. A. Koehler *U.S. Patent No. 4,812,658 Mar. 14, 1989*

HIGH ACCURACY DESCRIPTION OF THE FRINGE FIELDS IN PARTICLE SPECTROGRAPHS

Ralf Degenhardt and Martin Berz

The precision with which one can approximate measured field data by analytical functions depends crucially on the accurate description of the fall-off of the fringe field. The less accurate an analytical model approximates the fringe field, the more higher-order derivatives will deviate from their actual values. This means that higher-order optical properties might be calculated less precise, since derivatives of the midplane field of order n contribute to the nth-order aberrations.

We apply the image-charge method to approximate an analytically given reference field and obtain a maximum relative inaccuracy smaller than 10^{-4} in the relevant field area. In addition, derivatives of the image-charge field up to the fifth order approximate the analytical values very well. For our approach we used the field information in the midplane and in two additional planes both above and below the midplane. In this case noise on the field data can be compensated up to a certain extent.

The fringe field of dipole magnets has an essential influence on their optical properties. Field inhomogeneities at the dipole edges possess higher multipole components which considerably contribute to the individual aberrations. In the case of large aperture spectrographs (solid angles $\geq 10\,\mathrm{msr}$) with high energy acceptance ($\geq 10\%$), the hardware correction of these aberrations requires so many multipole elements that software-correction methods seem to be more appropriate [1]. The S800 [2] is such a spectrograph designed for an energy resolution of one part in 10000 and is currently under construction at the National Superconducting Cyclotron Laboratory. Because of its large phase space acceptance, aberrations of at least up to fifth order are assumed to be relevant and may impair the achievable resolution.

The required computation of the higher-order transfer map is only feasible if the (three-dimensional) magnetic field of the particle spectrograph can be approximated with sufficient precision in an analytical form. Only then one can take full advantage of differential algebraic methods [3]. For this purpose we apply the image-charge method generating the magnetic field by a superposition of Gaussian charge distributions so that Maxwell's equations are automatically satisfied. A critical estimate of the precision of our method, in particular in the case of field data with noise, is the multipole content of the fields. The multipole-moment decomposition of the different fields is readily performed by using the differential algebra based code COSY INFINITY [4].

As reference field we consider the field of rectangular iron bars with inner surfaces ($y = \pm y_0$) parallel to the midplane ($y = 0$). The geometry of the in $\pm y$-direction infinite extended magnetized bars is defined as follows:

$$-x_0 \leq x \leq +x_0, \quad |y| \geq y_0, \quad -z_0 \leq z \leq +z_0. \tag{1}$$

For this geometry one obtains for the y-component of the magnetic bar field $H_y(x,y,z)$ an analytical solution of the form [5]:

$$H_y^B(x,y,z) = H_0^B \sum_{i,j} (-)^{i+j} \left[\arctan\left(\frac{x_i \cdot z_j}{y_+ \cdot R_{ij}^+}\right) + \arctan\left(\frac{x_i \cdot z_j}{y_- \cdot R_{ij}^-}\right) \right] \tag{2}$$

with $i, j = 1, 2$ and introducing the following abbreviations:

$$x_1 = x - x_0 \quad , \quad x_2 = x + x_0, \tag{3}$$

$$y_- = y_0 - y \quad , \quad y_+ = y_0 + y, \tag{4}$$

$$z_1 = z - z_0 \quad , \quad z_2 = z + z_0, \tag{5}$$

and

$$R_{ij}^{\pm} = (x_i^2 + y_{\pm}^2 + z_j^2)^{1/2}. \tag{6}$$

H_0^B is determined by the maximum field at the bars.

Considering the y-component of the magnetic field, we generate from $H_y^B(x, y, z)$ reference field points on a regular grid in the midplane (see Fig. 1) as well as in planes above and below the midplane.

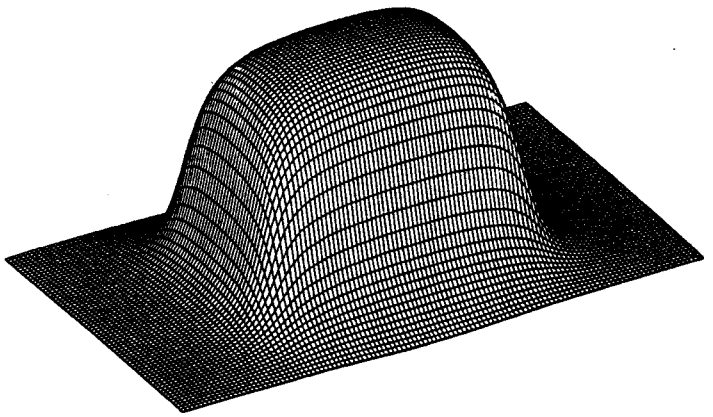

Figure 1: Analytical reference field $H_y^B(x, 0, z)$. Here we assume $x_0 = 2.5D$, $z_0 = 3.75D$ and $y_0 = D/2$ in units of the gap distance D between the two bars.

Placing image charges on grids parallel to the midplane, we approximate the field data obtained from the reference field described above. Note that we chose those planes not to coincide with the horizontal surfaces of the iron bars. Eventually our method will be applied to approximate measured field data.

Using the image-charge method in the magnetostatic case, one can not assume that the scalar potential is constant on the surfaces. Therefore, we determine the strengths of the individual charges by a least-square fit of the field values at the reference points which eventually will be given by the measured field data. In order to reduce a fine structure due to the influence of individual charges, we use three-dimensional Gaussian charge distributions [6]:

$$\rho(r) = \rho_0 \cdot e^{-(r/a)^2}. \tag{7}$$

Here a is a measure for the width of the Gaussian.

Adjusting their width appropriately, the superposition of regularly distributed identical Gaussians has proven to result in a rather smooth total distribution. Assuming three-dimensional Gaussians, each contribution to the y-component of the magnetic field is of the form:

$$H_y^{C_i} = y/r_i^3 \cdot \tilde{\rho}_0 \left[-\frac{a^2}{2} r_i \, e^{-(r_i/a)^2} + \frac{\sqrt{\pi}}{4} a^3 \, \mathrm{erf}(\frac{r_i}{a}) \right], \tag{8}$$

where $\mathrm{erf}(u) = 2/\sqrt{\pi}\int_0^u e^{-u'^2}du'$ is the error function. The total field $H_y^C(x,y,z)$ is the sum over all individual Gaussians.

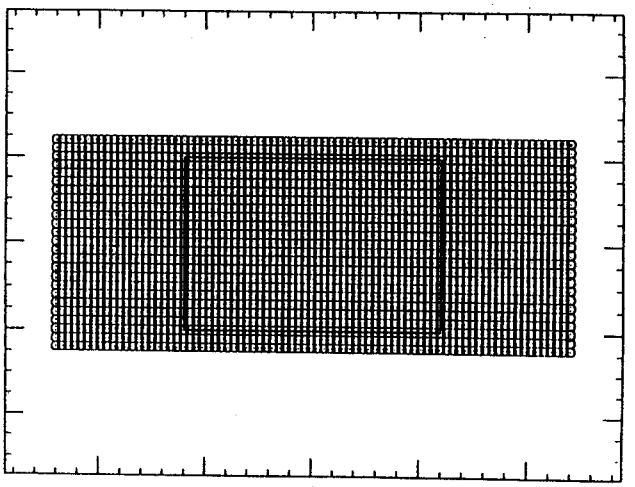

Figure 2: Grid with Gaussian charge distributions. The bold inner rectangle indicates the cross-section of the bar. Note the smaller stepsize in the horizontal direction in order to describe the fall-off of the fringe field in more detail.

For the following calculations we make use of the midplane symmetry of the magnet. One of the grids with the Gaussian charges is located at $y = \pm D$ and is larger than the cross-section of the bars (s. Fig. 2). The distance between the Gaussians is chosen to be approximately a. A second grid with $a = 1.5D$ is placed at the planes $y = \pm 5D$, so that eight Gaussians cover almost the entire area shown in Fig. 2. Note that at a distance of $3a$, the Gaussian distribution is approximately zero. Therefore, it is assumed that $\rho = 0$ at the reference planes, which are located at $y = 0, \pm 0.125D$, and $\pm 0.25D$.

In total we placed $N_C = 535$ image charges on a quarter of the whole arrangement, taking advantage of the geometrical symmetry of the bars. Their strengths are determined by $N_R = 10125$ reference field points.

In the following we concentrate on the calculation of the difference between the charge field and the reference field on a stripe through the magnet in order to test the applicability of our method to the description of sector magnets. In this case we are mainly concerned with the simulation of the entrance and exit region of the magnet. The stripe covers 75% of the width of the bars and is twice as long as the bars. In this area considered as relevant, the maximum difference between the y-component of the two fields in the midplane $\Delta H_y(x,0,z) = H_y^C(x,0,z) - H_y^B(x,0,z)$ normalized on $H_y^B(0,0,0)$ is smaller than 10^{-4}. The maximum differences occur in a rather limited region of the fringe-field fall-off. It is important to note that the average error over the whole stripe can be estimated to be one order of magnitude smaller.

In order to simulate noise on measured field data, we add/subtract on every point of the reference field a field difference ΔH^N which is randomly distributed in an interval $\pm\Delta H^N_{max}$. In the case $\Delta H^N_{max}/H_y^B(0,0,0) = 10^{-4}$, the precision with which we can approximate the reference field is essentially unchanged. All over, the average error increases slightly due to the noise. Nevertheless, as long as the amplitude of the noise is within the range of the precision of the image-charge method, noise does not deteriorate the accuracy of the approximation.

It is interesting to notice that the method provided smoothing of the noisy data after we increased the noise amplitude by a factor of five. In this case the relative field difference $\Delta H_y(x,0,z)/H_y^B(0,0,0)$ is smaller than $1.5 \cdot 10^{-4}$. The areas of maximum field difference are not restricted to the fringe field fall-off anymore creating a difference pattern that is dominated by the noise.

In order to determine the multipole content of the different fields, we perform an expansion of the

magnetic scalar potential

$$\psi(x,y,z) = \sum_{lm} a_{lm}(z)\, x^l y^m. \tag{9}$$

In the case of midplane symmetry ($a_{l0} = 0$), the multipole coefficients a_{lm} with $m \geq 2$ are uniquely determined by the coefficients a_{l1}.

If the components of the fields or the magnetic scalar potential in the midplane are known in an analytical form, the individual multipole components can immediately be calculated within a DA based framework [3]. For particle optics calculations up to fifth order, the relevant coefficients are $a_{01}(z), a_{21}(z)$, and $a_{41}(z)$. The coefficient $a_{01}(z)$ describes the field distribution while $a_{21}(z)$ and $a_{41}(z)$ determine the second and fourth derivative with respect to x. In the case of the bar field, derivatives in x-direction are more sensitive than for a homogenous sector magnet. Therefore, we assume that the accuracy which we obtain for the bar field is a reasonable estimate for the accuracy that we can expect in the case of homogeneous sector magnets including higher-order derivatives.

Using the code COSY INFINITY [4], we calculated the distribution of the coefficients $a_{01}(z), a_{21}(z)$, and $a_{41}(z)$ for the bar field and its approximated field. The results are shown in Fig. 3-4. As one can see, the second derivatives agree very well while a slight deviation is noticeable for the fourth derivative.

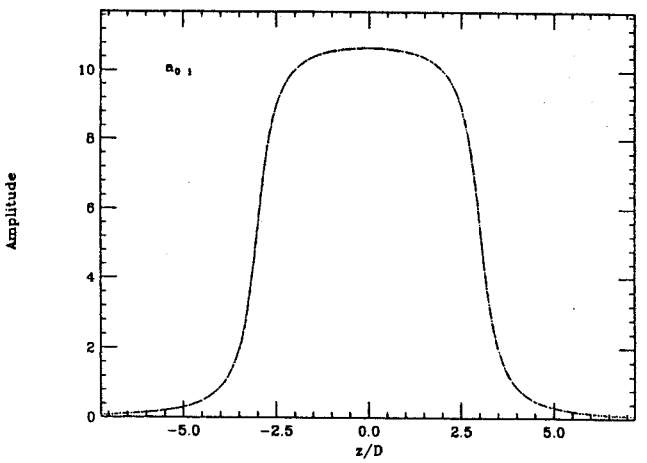

Figure 3: Multipole coefficient a_{01} along the (straight) z-axis through the magnet for the analytically known bar field ($\cdots$) and its approximation by the image-charge method (---).

Besides this, our calculations have shown that, although noise does not have an essential influence on the y-component of the field, its effect on the derivatives is not negligible. Therefore, a smoothing of noisy data is advisable as soon as higher-order optics calculations are performed. Nevertheless, since the image charge method itself compensates for the noise up to a certain extent, the importance of the actual smoothing algorithm should be less critical.

References

1. M. Berz, K. Joh, J.A. Nolen, B.M. Sherrill, and A.F. Zeller. Reconstructive correction of aberations in nuclear particle spectrographs. *Phys. Rev C*, 47:537-544, 1993.
2. J.A. Nolen, A.F. Zeller, B.M. Sherrill, J.C. DeKamp, and J. Yurkon. Technical Report, National Superconducting Cyclotron Laboratory. *MSUCL-694*, 1989.
3. M. Berz . Differential algebraic description of beam dynamics to very high orders. *Particle Accelerators*, 24:109-124, 1990.
4. M. Berz. COSY INFINITY (Version 6), Reference Manual 1992. *MSUCL-896*, 1993.

5. M.M. Gorden and T. Taivassalo. The Z^4 orbit code and the focusing bar fields used in beam extraction calculations for superconducting cyclotrons. *Nucl. Instr. and Meth.*, A247:423-430, 1986.
6. M. Berz. Differential algebraic description and analysis of trajectories in vacuum electronics devices including space-charge effects. *Trans. Electron Devices*, 35:2002-2009, 1988.

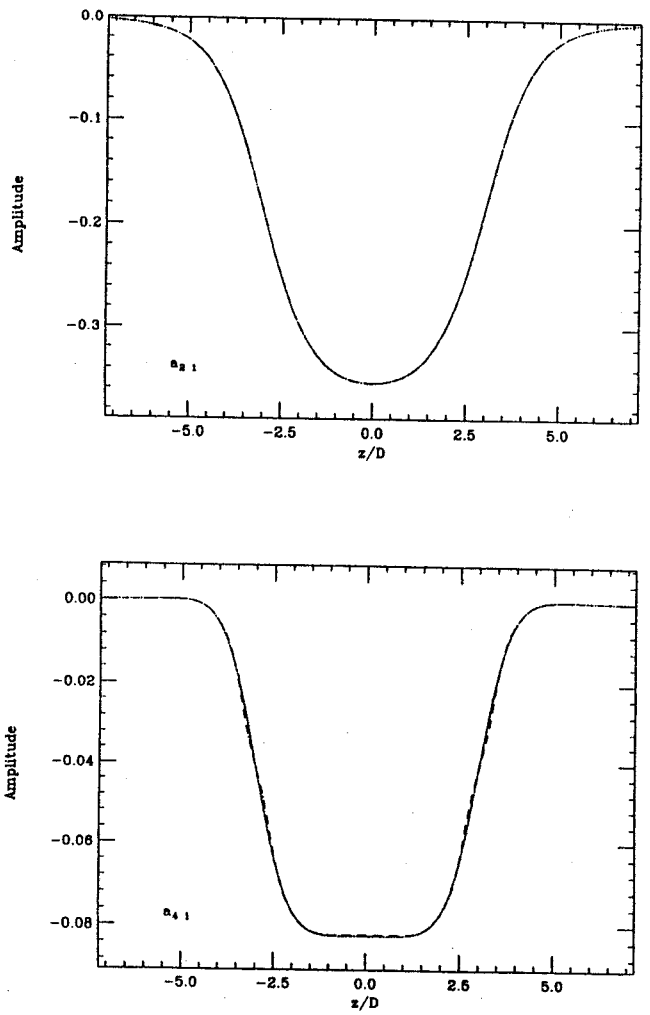

Figure 4: Multipole coefficients a_{21} (top) and a_{41} (bottom) as in Fig. 3.

SURVIVAL TIMES OF PARTICLES IN STORAGE RINGS

G. H. Hoffstätter and M. Berz

Storage rings are designed to hold particles for a long time. In the SSC this time is in the order of one day, which relates to $3 \cdot 10^8$ turns around the machine. To ensure that the machine design is capable of holding the required emittance for that number of turns, it is important to develop a method to find out how long a particle with a given initial condition will remain inside the ring. This could be done by tracking the paths of particles through 10^8 turns, which in an accurate way is far too time consuming with todays computing power, and the stability of motion can only be checked for a limited number of particles. There are, however, some programs available that follow this approach using kick approximations for the optical elements to speed up the computation [1]. Other approaches look at the one turn transfer map that relates initial phase space coordinates $\vec{z}_i$ to final coordinates after one turn $\vec{z}_f = \vec{M}(\vec{z}_i)$. This one turn map contains all information about particle motion after many turns since many turns are described by successive action of the one turn map.

The transfer map can be approximated in different ways. Recently an appropriate choice of spline functions and fourier series has been applied [2]. More Commonly, the Taylor expansion of the function is used. This Taylor map can be obtained automatically to an arbitrary order when DA codes are used [3]. Time considerations often restrict calculations to about order 12. Usually the Taylor map approach is justified since in accelerators motion near the closed orbit is weakly nonlinear. Once the one turn map is obtained, particles can be tracked through the map to find out how long they stay inside the accelerator. Applying high order maps the required number of turns can still be very time consuming and, like in the case of element by element tracking, the stability can only be checked for a very limited number of particles.

We want to propose a method which analyses the one turn map directly without tracking through it several times. Furthermore this method will not only test single particles but will give information about all particles in a given region of phase space. We assume that there is a closed orbit in the ring. Particles with phase space coordinates near the closed orbit will not be lost, particles which are too far away from the closed orbit will be lost during their motion around the ring. We therefore divide the phase space $\mathcal{P}$ into the allowed region $\mathcal{O}$ and the forbidden region $\mathcal{P}\backslash\mathcal{O}$.

The question we want to answer is: How many turns does a particle which starts in a given region of phase space $\mathcal{N}$ circle the ring without leaving the accelerator. We therefore look for the number

$$N_{\max} = \max\{n | \vec{M}^n(\mathcal{N}) \subseteq \mathcal{O}\} \tag{1}$$

where $\vec{M}^n(\mathcal{N}) = \{\vec{M}^n(\vec{z}) | \vec{z} \in \mathcal{N}\}$, and $\vec{M}^n(\vec{z})$ means applying the map n times. The different regions are shown in figure 1 a). With the following method we will find a strict lower bound N for $N_{\max}$.

If we find a real valued test function $f(\vec{z})$ which does not have common values in $\mathcal{N}$ and in $\mathcal{P}\backslash\mathcal{O}$, then successive action for the map must bridge a gap Δf as shown in figure 1 b). Particles start to bridge this gap by entering the phase space region $\mathcal{S}_i = \vec{M}(\mathcal{N})\backslash\mathcal{N}$. The gap is bridged when a particle has reached the region $\mathcal{S}_f = \vec{M}(\mathcal{O})\backslash\mathcal{O}$. If $\mathcal{S}_i$ or $\mathcal{S}_f$ are empty, particles in $\mathcal{N}$ will never leave $\mathcal{O}$. If they are not empty, the gap goes from f_i to f_f with $f_i = \max\{f(\vec{z}) | \vec{z} \in \mathcal{S}_i\}$ and $f_f = \min\{f(\vec{z}) | \vec{z} \in \mathcal{S}_f\}$. The function $d(\vec{z}) = f(\vec{M}(\vec{z})) - f(\vec{z})$ describes how much the gap is closed by the action of the map. If we assume $f_f \geq f_i$, the maximum step from f_i towards f_f is

$$\delta = \max\{d(\vec{z}) | \vec{z} \in (\mathcal{O}\backslash\mathcal{N})\} \quad . \tag{2}$$

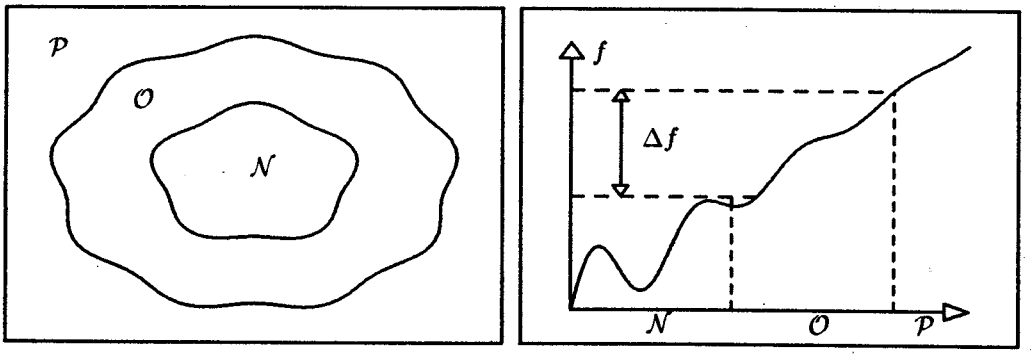

Figure 1: a) The initial region $\mathcal{N}$ and the allowed region $\mathcal{O}$ of phase space $\mathcal{P}$ with $\mathcal{N} \subset \mathcal{O} \subset \mathcal{P}$. b) The gap Δf that has to be bridged.

A particle that starts in $\mathcal{N}$ therefore survives at least N turns with

$$N = [\frac{f_f - f_i}{\delta}] \ . \tag{3}$$

We are thus left with four problems:

1. finding a suitable test function $f(\vec{z})$ such that N becomes favorable.
2. finding f_i, the maximum of $f(\vec{z})$ on $\mathcal{S}_i$.
3. finding f_f, the minimum of $f(\vec{z})$ on $\mathcal{S}_f$.
4. finding δ, the maximum of the change of $f(\vec{z})$ under the action of the one turn map in the appropriate region.

Describing the initial region and the allowed region is essential to finding $\mathcal{S}_i$ and $\mathcal{S}_f$ and therefore to finding a function that changes substantially between those two regions. The allowed region of an accelerator is typically given by the acceptance in the x–p_x phase space, the y–p_y phase space, and the time–energy phase space while it is assumed that the liner map does not couple these phase spaces. The linear motion follows invariant ellipses in every plane. A canonical transformation can be applied, which transforms those ellipses to circles. The new coordinates are the linear normal form coordinates. Since the product of two circles is topologically a torus, the particle moves on the so called invariant torus, and the radii of those circles are the linear invariants of motion.

Giving those linear invariants of motion to describe the allowed region is equivalent to specifying the acceptances ϵ_i of the machine. The pictures a) and b) in figure 2 describe the ellipses which specify the boundary of the allowed region. The allowed region can also be expressed in figure 2 c) by drawing the allowed radii. The linear invariants are described by $I_i^{(1)}(\vec{z})$ and the conditions for the allowed region is $I_i^{(1)}(\vec{z}) \leq r_i = \sqrt{\epsilon_i}$ for all subspaces i. For $p_x = 0$ and $p_y = 0$ the radii are proportional to x and y. Since beamlines are circular, it is appropriate to change the allowed region in figure c) by requiring:

$$\sum_i (\frac{I_i^{(1)}(\vec{z})}{r_i})^2 < 1 \ . \tag{4}$$

To keep the notation simple we describe the initial region $\mathcal{N}$ in a similar way with radii αr_i where $\alpha < 1$. The boundaries are most easily described when a norm is introduced which measures the distance from the closed orbit according to the invariant torus on which the particle moves in linear approximation

$$||\vec{z}|| = \sum_i (\frac{I_i^{(1)}(\vec{z})}{r_i})^2 \quad . \tag{5}$$

The different regions are given by:

$$\mathcal{N} = \{\vec{z}|\alpha^2 \geq ||\vec{z}||\} \quad , \mathcal{O} = \{\vec{z}|1 \geq ||\vec{z}||\} \quad . \tag{6}$$

To make the desired estimate as good as possible, we should find a function $f(\vec{z})$, which tends to increase when $||\vec{z}||$ increases and should at the same time be close to an invariant to make δ as small as possible.

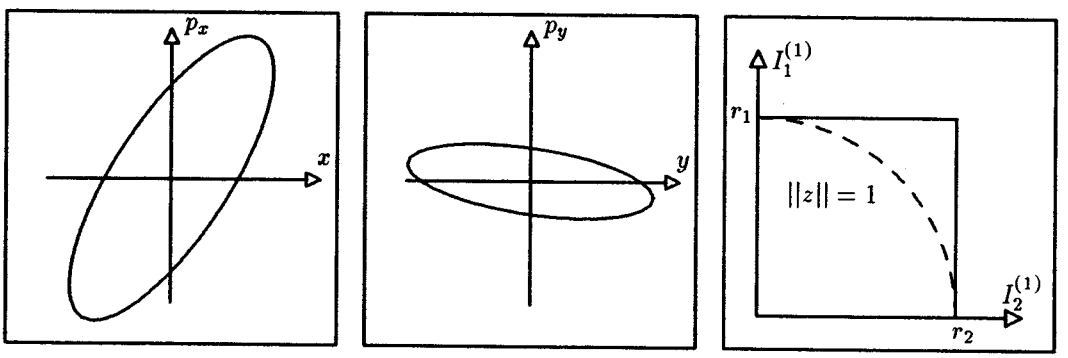

Figure 2: The motion on invariant ellipses in phase space: a) x–p_x, b) y–p_y. c) The allowed and the forbidden region and the definition of $||\vec{z}||$.

Such a function is easily obtained when the transformation to circles is not only performed for the linear map but for the complete nonlinear Taylor map up to the evaluation order n. The radii of those circles are invariant up to the evaluation order and are described by $I_i^{(n)}(\vec{z})$. Those normal form radii are easily obtained in the DA framework [4]. The desired function is therefore given by

$$f(\vec{z}) = \sum_i (\frac{I_i^{(n)}(\vec{z})}{r_i})^2 \quad . \tag{7}$$

The remaining three problems are concerned with the finding of maxima. The regions $\mathcal{S}_i = \vec{M}(\mathcal{N})\backslash\mathcal{N}$ and $\mathcal{S}_f = \vec{M}(\mathcal{O})\backslash\mathcal{O}$ can not be represented as clearly as the regions $\mathcal{N} = \{\vec{z}|\alpha^2 \geq |\vec{z}|\}$ and $\mathcal{O} = \{\vec{z}|1 \geq |\vec{z}|\}$. This does not lead to a problem when auxiliary functions $g(\vec{z})$ and $h(\vec{z})$ are used,

$$g(\vec{z}) = \begin{cases} f(\vec{M}(\vec{z})) & \text{if } \vec{M}(\vec{z}) \notin \mathcal{N} \\ -K & \text{if } \vec{M}(\vec{z}) \in \mathcal{N} \end{cases} \tag{8}$$

$$h(\vec{z}) = \begin{cases} -f(\vec{M}(\vec{z})) & \text{if } \vec{M}(\vec{z}) \notin \mathcal{O} \\ K & \text{if } \vec{M}(\vec{z}) \in \mathcal{O} \end{cases} \tag{9}$$

with a sufficiently big parameter K. The required quantities are then given by the following equations:

$$\begin{aligned} f_i &= \max\{f(\vec{z})|\vec{z} \in \mathcal{S}_i\} = \max\{g(\vec{z})|\vec{z} \in \mathcal{N}\} \\ f_f &= \min\{f(\vec{z})|\vec{z} \in \mathcal{S}_f\} = \max\{h(\vec{z})|\vec{z} \in \mathcal{O}\} \\ \delta &= \max\{d(\vec{z})|\vec{z} \in (\mathcal{O}\backslash\mathcal{N})\} \ . \end{aligned} \tag{10}$$

Those maxima can be found in a mathematically rigorous way using interval arithmetic [5]. Doing this would, together with equation 3, give a mathematically rigorous estimate for the survival time of particles propagated by the given one turn Taylor map.

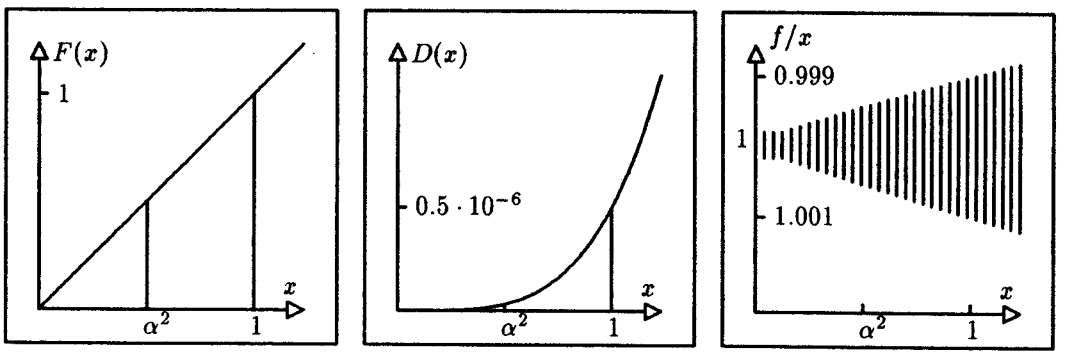

Figure 3: The functions a) $F(x)$ and b) $D(x)$ in the region $\mathcal{O}$. c) Variation of $f(\vec{z})$ relative to $||\vec{z}||$.

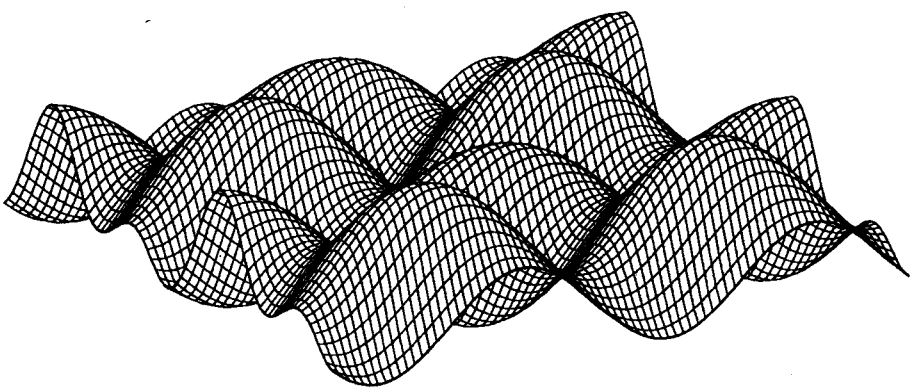

Figure 4: $d(\vec{z})$ on the boundary between allowed and forbidden region. The maximum δ of this function has to be found. In this example the function varies between $-0.5 \cdot 10^{-6}$ and $0.5 \cdot 10^{-6}$.

The functions $f(\vec{z})$ and $d(\vec{z})$ have some properties which allow to make sensible simplifications. Those properties will be demonstrated for the proposed PSR II. The evaluation order is 6 and the acceptances are ϵ_i = 1mm mrad. As shown in figure 3 a), the function $F(x) = \max\{f(\vec{z})|x = ||\vec{z}||\}$ is typically growing monotonously with x so that the maximum of $f(\vec{z})$ on $\mathcal{S}_i$ occurs at $||\vec{z}|| = \alpha^2$ and the minimum of $f(\vec{z})$ on $\mathcal{S}_f$ occurs at $||\vec{z}|| = 1$. The function $D(x) = \max\{d(\vec{z})|x = ||\vec{z}||\}$ is also typically growing monotonously as shown in figure 3 b), so that the maximum δ occurs at the border of the allowed region ($||\vec{z}|| = 1$). Furthermore figure 3 b) shows that the variation of $f(\vec{z})$ relative to $||\vec{z}||$ is much smaller than $\Delta f = f_f - f_i$ which therefore is close

to $1-\alpha^2$. We obtain the estimate

$$N = \frac{1-\alpha^2}{\max\{d(\vec{z})|1 = ||\vec{z}||\}} \tag{11}$$

which involves finding only one maximum on a subspace with constant $||\vec{z}||$. Figure 4 shows the function $d(\vec{z})$ on the border of the allowed region ($||\vec{z}|| = 1$). This function does not have sharp maxima so that sampling with 20 steps in each direction does give a good approximation of the maximum value. Table 1 gives N for different systems and for different evaluation orders for $\alpha^2 = 1/2$. For the pendulums the propagation after one second was taken as one turn map so that N describes the time in which the instruments certainly stays in the allowed region. Due to energy conservation, the pendulum and the coupled pendulums are stable for all times. The quality of our estimate is shown by the big numbers N which we obtain for those cases.

Order	Pendulum (r =1mm mrad)	Coupled Pendulums ($r_1 = r_2$ =1mm mrad)	PSR II ($r_1 = r_2$ =1mm mrad)
3	$1.37 \cdot 10^{10}$	$1.04 \cdot 10^{9}$	$3.22 \cdot 10^{4}$
4	$1.37 \cdot 10^{10}$	$1.02 \cdot 10^{9}$	$3.60 \cdot 10^{4}$
5	$1.20 \cdot 10^{15}$	$5.42 \cdot 10^{10}$	$6.37 \cdot 10^{5}$
6	$1.20 \cdot 10^{15}$	$4.20 \cdot 10^{12}$	$6.94 \cdot 10^{5}$

Table 1: Minimum number of turns N to move from $I_i^{(1)} = r_i/2$ to $I_i^{(1)} = r_i$.

The evaluation of the functions $f(\vec{z})$ and $d(\vec{z})$, using interval arithmetic to find the maximum values and therefore establishing a mathematically strict lower bound for the turn number N_{max}, is currently under investigation.

References

[1] L. Schachinger and R. Talman. TEAPOT, a thin element program for optics and tracking. *Particle Accelerators*, 22:35, 1987.

[2] J. S. Berg, R. L. Warnock, R. R. Ruth, and E. Forest. Construction of symplectic maps for nonlinear motion of particles in accelerators. Technical Report SLAC–PUB–6037, SLAC, 1993.

[3] M. Berz. Arbitrary order description of arbitrary particle optical systems. *Nuclear Instruments and Methods*, A298:426, 1990.

[4] M. Berz. Differential algebraic formulation of normal form theory. In *Proceedings of the 1992 Workshop on Nonlinear Effects in Accelerator Physics*, Berlin, 1992.

[5] E. Hansen. *An Overview of Global Optimization Using Interval Analysis*, pages 289–307. R. E. Moore, Academic Press, New York, 1988.

A MEASUREMENT OF 30 MeV/A ^{84}Kr BEAM ENERGY USING TIME-OF-FLIGHT

J. Bailey, J. Nolen[a], and S. Cheng[a].

An experiment measuring relativistic effects in H-like Kr[1] required knowledge of the velocity of the ~30 MeV/A ^{84}Kr beam. The A1200 spectrometer, used to separate charge states after stripping, had not been calibrated in absolute rigidity. So the straight section of beam line entering the N3 vault was temporarily reconfigured to measure the time of flight of the beam, immediately after the completion of the atomic experiment. This velocity measurement provides an external check on subsequent measurements of the A1200 rigidity at low excitation.

Foil	3.4 mg/cm^2 Al	1.6 mg/cm^2 C
Velocity	7.368 ±.007 cm/ns	7.416 ±.010 cm/ns
Bρ	1.836 ±.002 T-m	1.849 ±.003 T-m
E/A	29.48 ±.06 MeV/A	29.88 ±.06 MeV/A

Table 1: $^{84}Kr^{36+}$ Time-of-Flight velocity measurement of the 30 MeV/A Kr beam after charge stripping. Results are given in terms of velocity, magnetic rigidity, and energy per nucleon for the two different stripping foils.

Minipots were installed immediately after the C121 quadrupole, and in the 92 in. chamber. Two Si detectors were placed in the latter minipot with time of arrival of the beam measured on each detector. The forward detector was then moved (complete with electronics and cables) upstream to the first minipot, and beam time was measured again on each detector. Results are presented in Table ??. Corrections were made for the reference detector, and the effects of different beam sizes at the two locations (a focussed beam was ranged over the detector to determine time differences for various sections of the detector.) The uncertainty includes the measured effect of stretching the cable (the dominant source), frequency shifts made during the atomic experiment (±100 Hz), statistical errors in measuring time centroids and TDC scales, and errors in measuring distance, including possible sag and stretching at 2 – 4 lbs. tension.

The beam was nominally 30.12 MeV/A $^{84}Kr^{15+}$ before stripping. The fractional part is due to the frequency shift necessary to obtain this analog of 30 MeV/A $^{129}Xe^{23+}$, while preserving the rigidity. The distance between detectors was 1675.6 ±.3 cm.

Foil	3.4 mg/cm^2 Al	1.6 mg/cm^2 C
B1	5.91326 kG	5.96304 kG
B2	5.93019 kG	5.98429 kG
B3	5.91855 kG	5.93658 kG
B4	5.91570 kG	5.93853 kG
Bρ	1.839 ±.002 T-m	1.850 ±.002 T-m

Table 2: The magnetic rigidity, of the beams presented in Table 1, measured with the A1200 spectrometer in dispersive mode. The measured magnetic field in each of the four dipoles is also presented.

The beam rigidities, as measured with the A1200 spectrometer are presented in Table ??. The A1200

was in dispersive mode, with a resolution of 8mm per .1% in momentum. The beam spots were within 2 mm of the optic axis at both the focal plane position, and the target pot position leaving an error of .05%. The A1200 B is the average of the four dipole magnetic fields, each of which is accurate to 1 part in 10^6. The bending radius, ρ, at a rigidity of 1.7 T-m has subsequently been measured at 3.107 $\pm$.002 m[2].

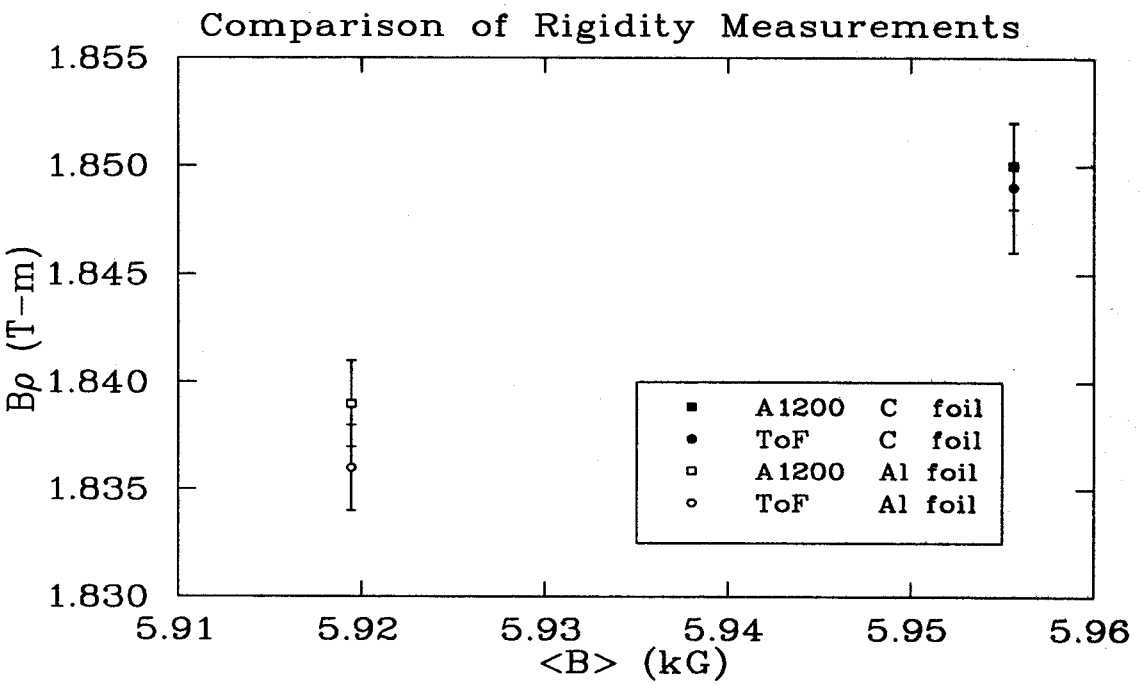

Figure 1: The A1200 rigidity at this excitation agrees closely with that calculated from the Time-of-Flight velocity measurement.

The rigidities obtained in both measurements are compared in Figure ??. The close agreement confirms the measurement of the A1200 dipole bending radius at this magnetic excitation.

a. Argonne National Laboratory

References

1. Cheng, S., "Branching Ratio for the M1 Decay of the 2 $^2S_{1/2}$ State in One–Electron Krypton" Phys. Rev. **A47** (1993) 903.
2. Sherrill, B., Private communication, MSU (1993).

STATUS OF THE SOLID HYDROGEN TARGET

D.E. Pendell, H. Laumer, and A.F. Zeller

Assembly and initial testing of the hydrogen target[1] have been completed, including testing of the helium cryogenic components and filling of the hydrogen target cell. The dewar contains approximately 0.6 liters of liquid helium. At a pressure of 7.9 psi and with the cell's heater turned off, the boil-off rate was 30 liters/hour. Using a 100 liter portable helium dewar supply, there would not be enough time to make acquisition of particle interaction data meaningful. The minimum desirable holding time is 24 hours. Heat load calculations for the entire assembly indicated that the maximum heat load should have been between 1 and 3 watts--sufficient to meet the desired holding time. It was decided to disassemble the hydrogen target cryogenics and determine the cause of the high heat load. Once disassembled, it was discovered that the major contributor to the heat load was a point contact in the helium fill line. The entire helium dewar system has been redesigned and upgraded to further lower the heat load.

The hydrogen target cell was also tested. The original hydrogen target cell, 1/8" thick copper, was attached to the helium dewar by a 1/4" diameter copper rod, 2" long. The target area was a 1/2" diameter hole covered with thin Mylar® windows. They are sealed with varnish, and held in place with copper keeper plates and 8 small bolts.

For testing, transparent cell windows were necessary to view the hydrogen's freezing dynamics. In the final application, the windows will be made of beryllium. A metering valve was used to fill the cell with hydrogen at a pressure of 300 millitorr. This was done to determine the minimum pressure at which the cell can be filled, allowing a thinner beryllium window to be used.

Kapton® windows were finally chosen for this testing because the original Mylar® windows cracked when they flexed at 4K. Once the cell was cold it was filled with hydrogen, with the fill line heater turned on. When the cell was full of liquid hydrogen the heater was turned off. It was observed that this heater has little effect and has been eliminated from the design. However, when the liquid hydrogen froze, it did so from the edges toward the center. This concentric freezing of the hydrogen caused a void to appear in the center of the cell. This center void is extremely undesirable in a target. Therefore, the target cell has been redesigned, utilizing a bi-metal cell. The bottom 54% of the cell is copper and is attached to the bottom of helium dewar. The top 46% of the cell is brass to capitalize on the enthalpy and heat transfer differential through the brass. The heat released by the hydrogen freezing will be transferred into the copper and be conducted into the helium dewar. This should cause the hydrogen to freeze from the bottom of the cell toward the top.[2]

The cell design will also incorporate a more easily removable cell attached with an extremely low temperature melting solder (110°C) and Cajon® VCR fittings on the stainless steel hydrogen fill line. This will allow quicker turn-around when changing to different thickness target cells.

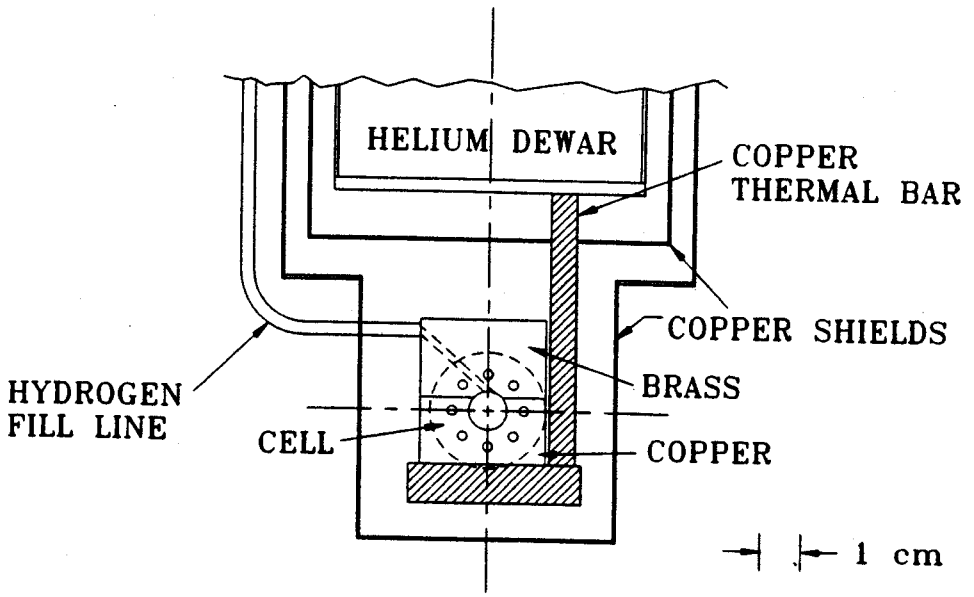

Fig 1. The redesigned hydrogen target cell.

References

1. A.F. Zeller, et al; Advances in Cryogenic Engineering 37A, 1503 (1992)

This second test method confirms the fast degradation of the fast light output within the first 40 days. These more detailed measurements seem to indicate that the VIS600M shows the smallest change. However, the long term effects can not yet be observed since the detectors were mounted only three months ago.

Both measurements are still under progress to investigate the long term development of the fast light output for the different coupling materials.

References

1. M. Laval *et al.*, Nucl. Instr. and Meth. **206**, 169 (1983)
2. R. Novotny *et al.*, TAPS-REPORT 10, University of Giessen, unpublished (1990).
3. G.F. Knoll, "Radiation Detection and Measurement", John Wiley & Sons, Inc. (1989).

A HIGH RATE PHOSWICH FORWARD ARRAY FOR THE MSU 4π ARRAY

R. Pak, W.J. Llope, D. Swan, J. Wagner, G.D. Westfall, D. Craig, E. Gualtieri, S. Hannuschke, T. Li, N. Stone, A.M. Vander Molen, and J. Yee

The forward array of the MSU 4π Array has been recently upgraded to include a newly designed close-packed phoswich array called the High Rate Array (HRA). This configuration offers minimum dead area, and acceptable granularity over the subtended solid angle. The HRA is to be utilized in experiments with high count rates, such as flow or coincidence runs, and is meant to be complementary to other high resolution forward arrays used in the 4π Array which employ silicon detectors, such as the Iowa Forward Array.

The HRA consists of three pentagonal rings of 10, 15, and 20 fast/slow plastic counters as shown in Figure 1. The array spans polar angles from 3° - 20°, subtending all solid angle between the Maryland Forward Array and the rest of the 4π Array. This results in ~95% geometric efficiency for the entire detector system. A 45 detector design was choosen so that no additional electronics would be necessary. The only investment was in scintillator plastic and the mechanical support structure. Machining was done in-house, and all additional fabrication was carried out by the 4π Group.

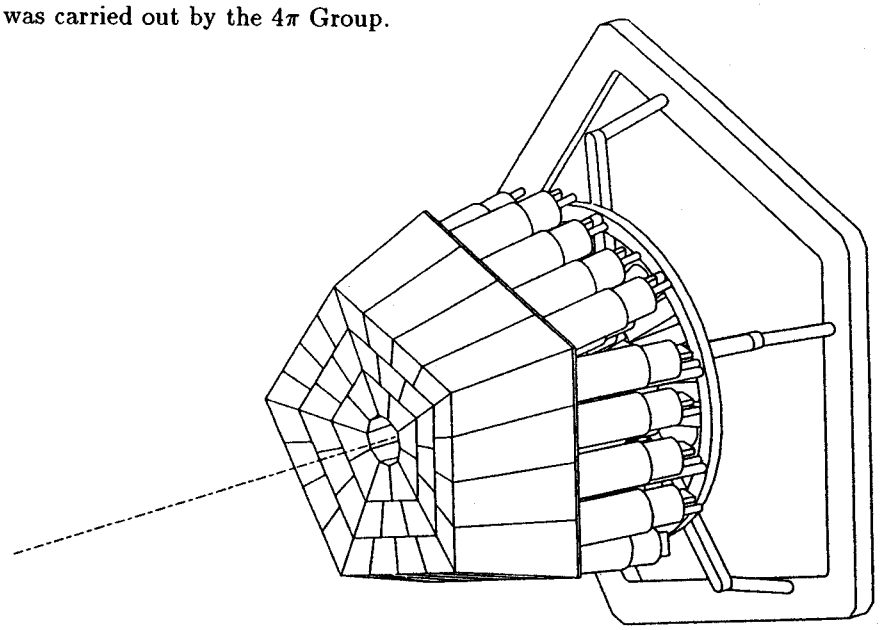

Figure 1: The newly designed close-packed phoswich forward array for the 4π Array called the High Rate Array (HRA). The array consists of 45 fast/slow plastic counters, and spans polar angles from 3° - 20°.

The individual detectors are fast/slow plastic counters which measure E, ΔE, and time by the same technique presently used for the phoswiches in the rest of 4π Array [1]. The detectors are painted with an epoxy based paint pigmented with TiO_2 to reduce cross talk and are glued together in five wedges of nine detectors, effectively minimizing dead area. The front of the array is covered with 1.5 μm Mylar to increase light collection efficiency, and is positioned as close to the target as would allow a 2 in. diameter phototube to be optically coupled onto the back of each detector.

Simulated events were run through a software replica of the HRA to determine the positions and sizes of the 45 HRA elements that provide the optimal granularity for these generated events, and minimize the probability for double hits in each detector. Three designs were considered, each having a different combination of the number of detectors in each of the pentagonal rings: DESIGN(1) 20-15-10; DESIGN(2) 15-15-15; and

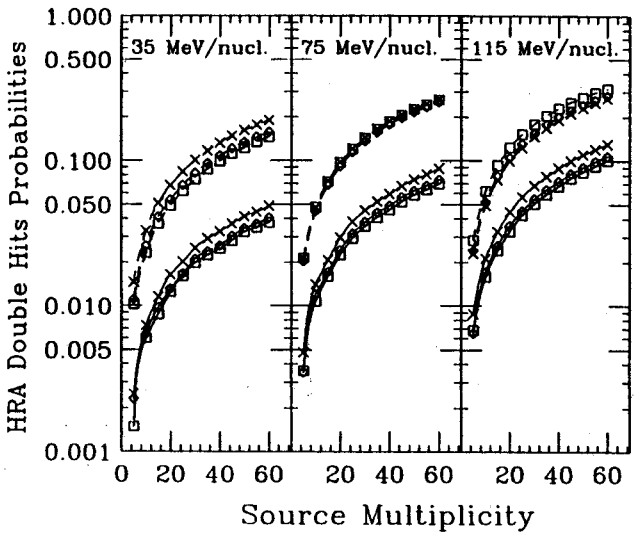

Figure 2: Simulation results for double hits probabilities in various designs for the HRA. At each incident energy the upper curves are for projectile source emission, and the lower curves are emission from Ar + Sc at mid-rapidity. Crosses are for DESIGN(1); diamonds are for DESIGN(2); and squares are for DESIGN(3).

DESIGN(3) 10-15-20 (counting from the ring closest to the beam axis). At each incident energy, events were generated with specific multiplicities in a projectile-like frame (upper curves) and in an Ar + Sc CM frame (lower curves), as shown in Figure 2. The particles were distributed isotropically in each frame with thermal (T = 10 MeV) kinetic energy distributions. The vertical axis is the probability that two or more particles hit the same HRA element. The results indicate that the design that overall is least susceptible to double hits is DESIGN(3), and was therefore considered the most suitable for the energy range of interest in high rate experiments.

References

1. G.D. Westfall, J.E. Yurkon, J. van der Plicht, Z.M. Koenig, B.V. Jacak, R. Fox, G.M. Crawley, M.R. Maier, B.E. Hasselquist, R.S. Tickle, and D. Horn, Nucl. Inst. and Meth. A238, 347 (1985).

TRANSPUTERS IN HIGH SPEED DATA AQUISITION SYSTEMS

A. Vander Molen, R. Au, R. Fox, and S. Hannushke

One problem associated with large scale detectors such as the NSCL 4π Array is that of a cost effective, dynamic, and fast data acquisition system. This detector, in particular, can produce sustained data rates above one megabyte/sec. Meanwhile, cost effective storage media like 8mm tape can only record data at rate around 450-500 kilobytes/sec. It was found that 30 - 50% of the recorded data was either redundant information or "noise". Many experiments would also benefit from a secondary software trigger by reducing the undesired data recorded on tape. The *inmos* T800 transputer chip with their high speed links offers a fast, economical, and easy way of building a system that can be expanded to meet new demands without the drawbacks of a bus based system. A prototype system has been designed and built at NSCL to investigate the application of transputers to data acqusition frontends. This system is currently used as the data acqusition system of the NSCL 4π Array.

The transputer system was initially designed for 5 transputers linked to a SUN host system. The transputers will handle all run control, initialization, data acquisition, and data filtering. The SUN would receive buffered data and route this data for storage and/or online analysis. The prototype system consists of one transputer housed in a VME crate along with CAMAC and Lecroy ECLine interfaces. The transputer was interfaced to the SUN via transputer links. Both short (10 meter, 20Mbits/sec) and long (30 meter, 10Mbits/sec) links were used. Software was developed using *inmos* OCCAM language for run control and data acquisition. OCCAM was found to be ideally suited for this type of application. The system is now being used for experiments and found to improved overall data rates by 20% using the long links with no optimization or filtering. The system was also found, when used in a calibration run at Los Alomos, to be very portable. Current research is being done with filters, adding more nodes and improving link speeds.

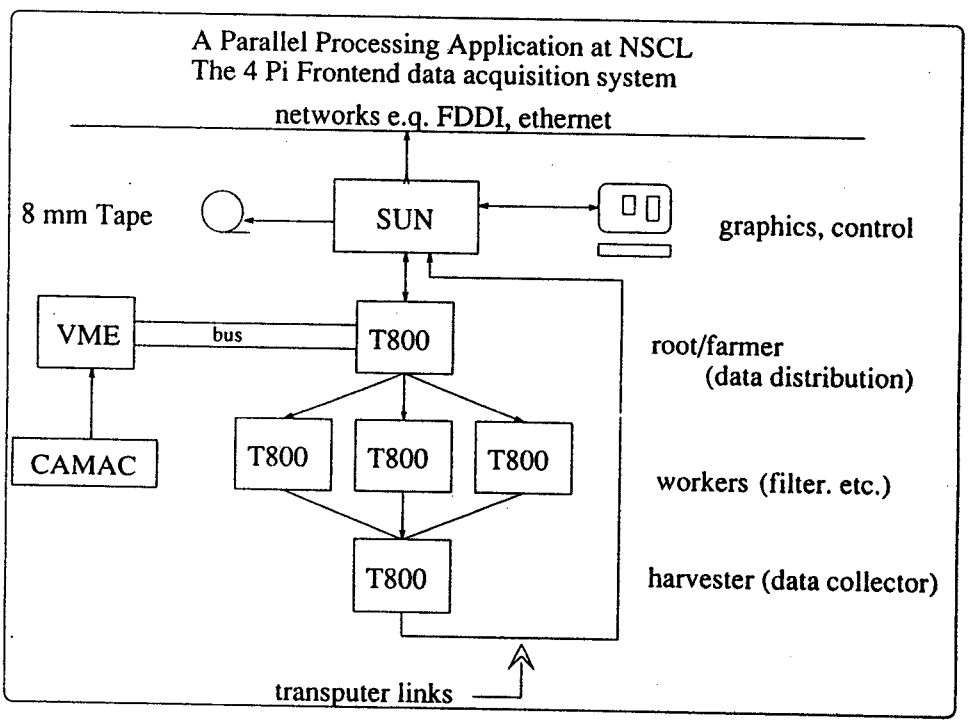

OPERATION OF A DOUBLE-SIDED ANNULAR SILICON DETECTOR FOR THE MSU 4π ARRAY.

W.J. Llope, R. Pedroni[a], R. Pak, G.D. Westfall, J. Wagner, A. Mignerey[b], D. Russ[b], J. Shea[b], H. Madani[b], R.A. Lacey[c], D. Craig, E. Gualtieri, S. Hannuschke, T. Li, J. Yee, and E. Norbeck[a].

A recent upgrade of the MSU 4π Array [1] includes the addition of a segmented phoswich-silicon detector array covering laboratory polar angles from $\sim$1.5° to $\sim$2.9°. This array, the Maryland Forward Array (MFA), was recently used in concert with the fully instrumented 4π Array for the measurement of deep inelastic and massive transfer reactions of 50 MeV/nucleon ^{129}Xe projectiles with ^{27}Al, ^{nat}Cu, ^{139}La, and ^{165}Ho targets. A description of the setup and operation of the double-sided annular silicon detector (ASi) that is part of the MFA for the collection of these data, as well as 40 MeV/nucleon ^{16}O, ^{40}Ar, and ^{84}Kr "cocktail" beams, is described herein.

The MFA is shown in Figure 1; the ASi is the entrance detector for this array. The 297 μm of silicon that is the active region of the ASi is read on the ohmic side using sixteen segments, which provide an electronic pulse height proportional to the energy deposited in the silicon by an incident particle, as well as the azimuthal angle for the hit in 22.5° bins. The junction side is read by sixty four concentric strips. The correlation of the pulse heights in the strips with those from the segments allows the additional assignment of the polar angles of the hits in $\sim$0.9° bins.

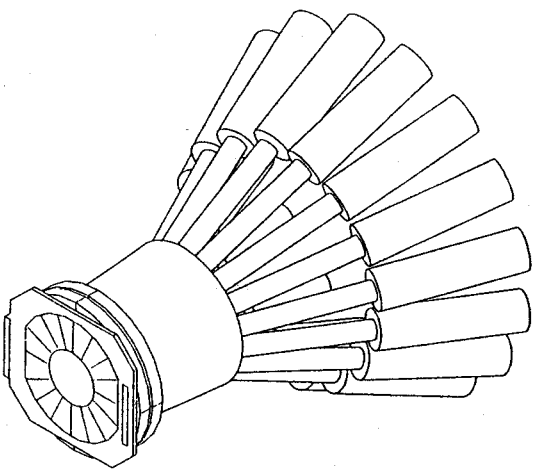

Figure 1: The Maryland Forward Array; the sixteen ASi segments are in front (closest to the target), and are followed by sixteen plastic phoswich detectors.

The ASi is positioned directly in front of the phoswich part of the MFA, which is divided azimuthally into sixteen optically decoupled fast/slow plastic detectors. The correlation of the pulse heights from the ASi and the fast plastic of the MFA phoswich detectors allows the measurement of the charge, kinetic energy, and angles of large and/or slowly moving fragments which may stop in the fast plastic, while the correlation of the fast and slow plastic gives similar information for generally lighter and faster particles.

The ASi is fully depleted for voltage drops across the detector of 20.5 V, for which the capacitance of the ASi is $\sim$117 pF/segment or $\sim$29 pF/strip. Positive voltage was applied to each of the sixteen (ohmic side)

segments in a daisy chain from a single voltage supply, although future experiments will use a new NSCL built voltage divider module [2] for more accurate control of the voltage across each segment. The ASi was over-biased to a voltage drop of 30 V during the data collection to insure good charge collection, for which the total leakage current was very stable and approximately 55 μA, or 3.4 μA/segment.

The signals from both sides of the ASi travel through about 8 feet (~216 pF) of shielded ribbon cable to NSCL built pre-amplifiers, which have a full scale for signals equivalent to energy depositions on the order of 10 GeV (about a factor of five larger than the energy deposited in the ASi by 50 MeV/nucleon ^{129}Xe nuclei). The energy resolution of the ASi is compromised somewhat by the large capacitance of the signal cables relative to the detector capacitance. The pre-amplifiers will be mounted directly onto the 4π-Array backplate in future experiments, allowing shorter overall cable lengths and greatly reduced input capacitance to the pre-amplifiers. The *RC* time constant of the pre-amplifiers is 100 μs, which allows maximum average count rates of approximately ~2 kHz. During the data collection, the particle rates per channel were kept on the order of ~250 Hz.

The pre-amplified signals are then input into NSCL built "Quad Shaper" modules, and are shaped to a bi-polar pulse with the negative lobe peaking at 10 μs for all but the smallest pulse heights, which "slew", i.e. peak faster depending on the (low) pulse height. The peak heights of the bipolar shaped pulses are proportional to the energy deposited in the ASi, and the heights of the negative lobes are digitized by LeCroy 4300B FERAs using a narrow (~200 ns) gate positioned 10 μs after a hit in the MFA phoswich has been registered. Future experiments will use NSCL built peak-sensing ADCs [2] for measurements of ASi pulse heights that are not biased by the pulse slewing, as well as additional trigger logic to allow self-start triggers of the ASi, which will allow the measurement of the heaviest and/or slowest fragments which stop in the ASi.

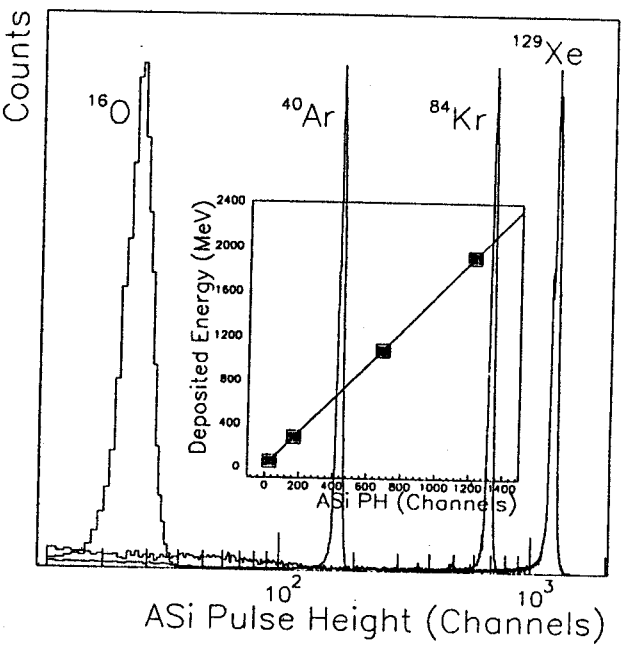

Figure 2: The ASi pulse heights in FERA channels measured using several 40 MeV/nucleon "cocktail" beams, and 50 MeV/nucleon ^{129}Xe, on a ^{129}La target. The inset depicts the comparison of the digitized ASi pulse heights in FERA channels with calculated values of the energy loss in the ASi for each ion and energy above.

Figure 2 depicts the digitized ASi pulse heights when 40 MeV/nucleon beams of ^{16}O, ^{40}Ar, and ^{84}Kr are directed onto a ^{139}La target. Also included in this Figure are the results from the 50 MeV/nucleon ^{129}Xe+^{139}La reaction. These events are predominately elastic scattering, so that the positions of the observed peaks can be used to calibrate the ASi (and the MFA phoswich). The inset in Figure 2 gives the energy lost in the ASi by these ions at these energies calculated using a standard energy loss code ("ELOSS"), versus the mean value of the measured ASi pulse height in FERA channels. Over the range Z=8 to Z=54 the ASi and its associated electronics are linear.

The measured correlation of the digitized pulse height from an ASi segment with that from the fast plastic of the phoswich detector ("ΔE") directly behind this segment is shown in Figure 3 for the 50 MeV/nucleon ^{129}Xe+^{139}La reaction. Although this is raw on-line data, particles with $8 \lesssim Z \lesssim 30$ are well resolved, while the separations between the bands for the larger charges are not as obvious due to the binning of the figure and the apparent strong saturation of the MFA phoswich ΔE signals. It is noted that particles with $1 \leq Z \lesssim 25$ are clearly resolved in the correlation of the MFA phoswich fast ("ΔE") versus slow ("E") plastic signals.

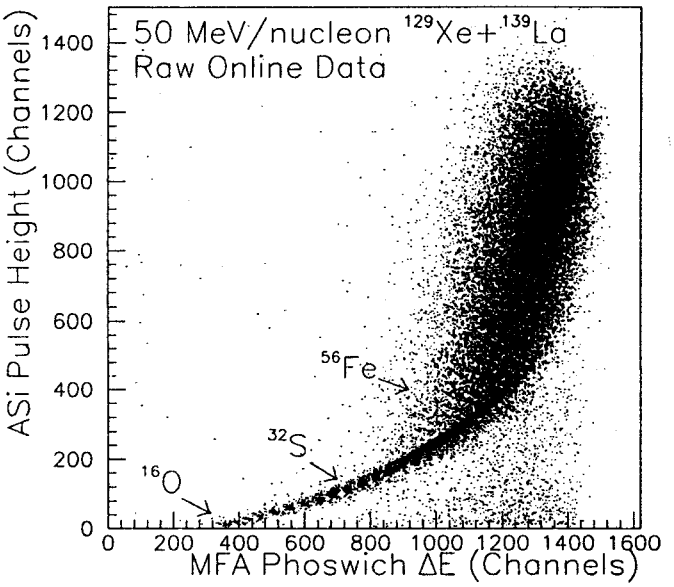

Figure 3: The correlation of the ASi pulse heights with the MFA fast plastic ("ΔE"), both in FERA channels, for 50 MeV/nucleon ^{129}Xe + ^{139}La collisions.

The treatment of the saturation in the MFA phoswich signals is presently underway. We note though that, according to energy loss calculations, the resolution necessary to resolve 50 MeV/nucleon Xe (Z=54) fragments from 50 MeV/nucleon I (Z=53) fragments in the ASi is ~2.1%, while a Gaussian regression of the Z=54 peak of Figure 2 gives a resolution of 1.5%. We therefore expect that, by gating the MFA ΔE vs E signals for light particles, and the ASi and the MFA ΔE signals for heavier particles, no worse than unit charge resolution over the full range of particles and fragments in these data will be possible.

a. Dept. of Physics and Astronomy, University of Iowa, Iowa City, IA 52242
b. Department of Chemistry, University of Maryland, College Park, MD 20742
c. Department of Chemistry, SUNY - Stony Brook, Stony Brook, NY 11794

References

1. G.D. Westfall *et al.*, Nucl. Inst. and Methods **A238**, 347 (1985).
2. A. McGilvra, private communication.

IOWA FORWARD ARRAY: A CESIUM IODIDE/SILICON FORWARD ARRAY FOR THE MSU 4π ARRAY

E. Norbeck[a], F.D. Ingram[b], W.J. Llope, R.S. Pedroni[c], G.D. Westfall and L.B. Yang[a]

The Iowa Forward Array is a closely-packed, multi-element, high-resolution detector array that is intended to replace the present forward array in the MSU 4π Array. The present forward array is a loosely-packed array of forty-five phoswich detectors that only covers about 56% of the solid angle in the $4.5° \leq \theta \leq 20.°$ angular range. This angular range is the region between the forward five hexagonal detectors of the 4π Array and the Very Far Forward Array of the University of Maryland. The Iowa Array will cover as much of the solid angle in this angular range as is technically possible – at least 90% coverage is expected. The Iowa Array will also have better energy and charge resolution and a lower energy threshold than the phoswich array.

After an exhaustive series of studies, a final design for the Iowa Array has been chosen. This design consists of three pentagonal rings, each composed of twenty $\Delta E/E$ detector telescopes. Each detector telescope contains a 300 μm-thick Si PIN diode used as a transmission ΔE detector and a CsI(Tl) crystal coupled to a Si PIN photodiode as the E detector.

The arrangement of the CsI(Tl) crystals is shown in Fig.1. The rings will be located with the ΔE detectors at about 13.5, 35 and 51 cm from the target. The CsI crystals will be 6 cm long. This length of CsI together with a 300 μm-thick ΔE detector will stop about 140 MeV protons.

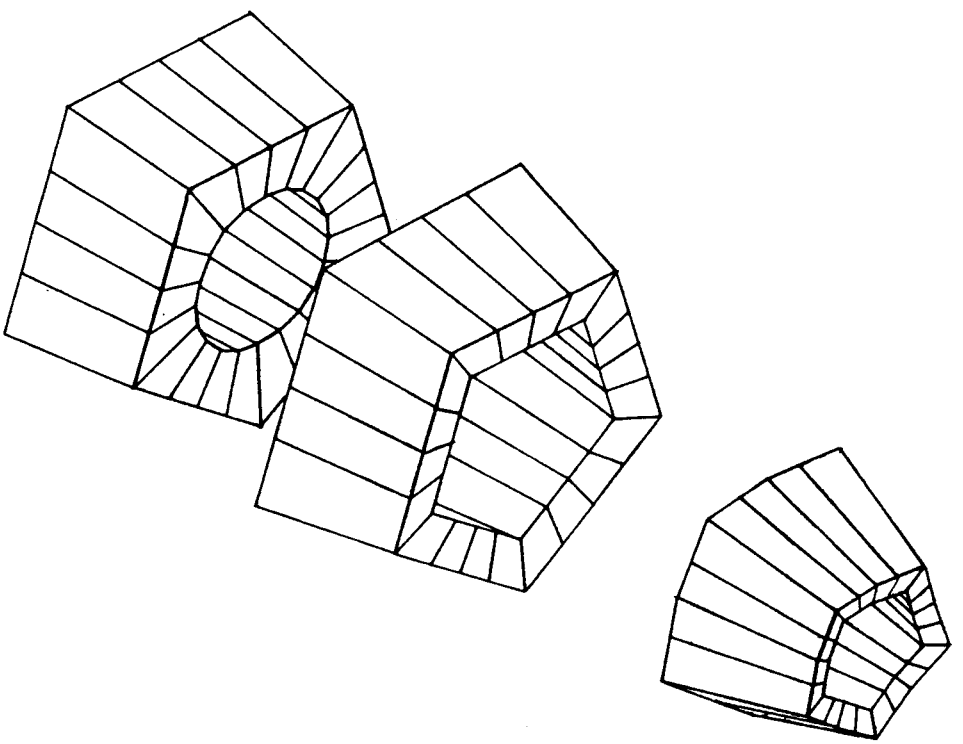

Figure 1: Arrangement of the three rings of twenty CsI(Tl) crystals.

The ΔE detectors will be single pieces of silicon that are divided into two or four segments – one segment to go in front of each CsI(Tl) crystal. There will be five ΔE detectors – each divided into four segments – in both of the two rings farthest from the target. In the ring closest to the target, there will be ten ΔE detectors, each divided into two segments. The segmented detectors for the ring closest to the target and for the middle ring are shown in Fig.2.

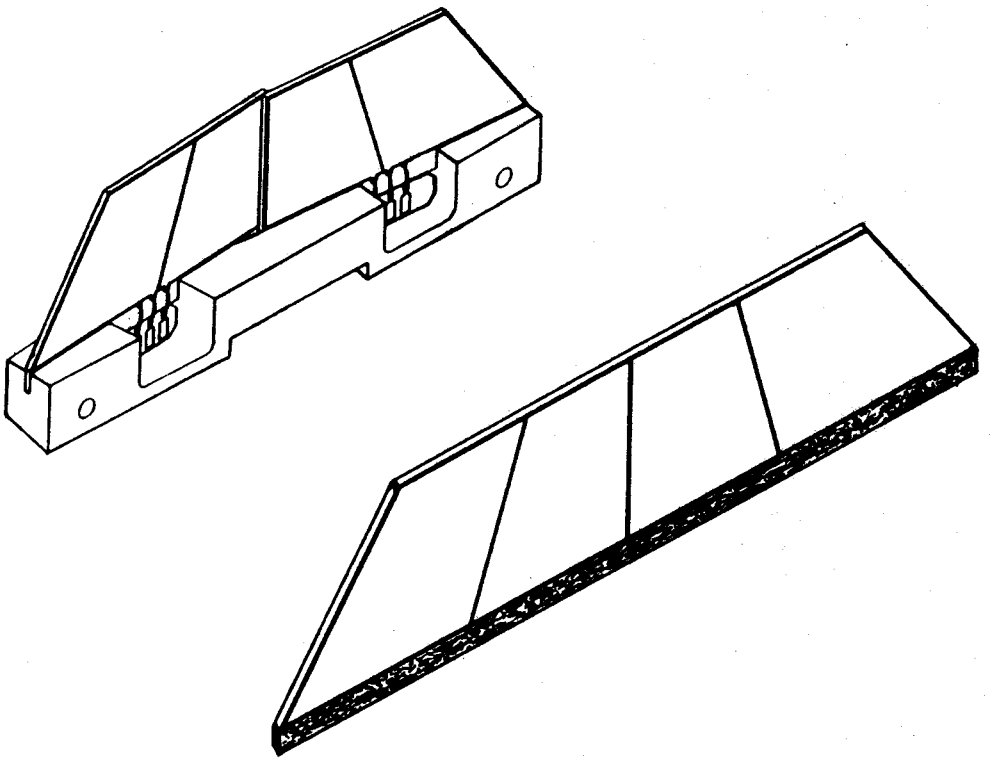

Figure 2: The arrangement of two, two-segment detectors in the mount for one side of the ring closest to the target is shown at the upper left. At the lower right, the outline of a four-segment detector for one side of the middle ring is shown. The dark strip at the bottom of the detector is an extension of the guard ring structure which will be used to attach the detector to its mount.

The final details of the design will be finished in the early spring of 1993. We hope to take delivery of the detectors and to begin the assembly in the summer. An active program is underway to develop the electronics for this project – including a new eight-channel, peak sensing CAMAC ADC. We expect to conduct the first experiments with the completely-operational Iowa Forward Array in the summer of 1994.

a. The University of Iowa, Department of Physics and Astronomy, Iowa City, Iowa 52242.
b. Rock Valley College, Rockford, Illinois 61114.
c. The University of Iowa, but in residence at Michigan State University.